RF Characterization and Modeling of High-Power InGaAs/InP Photodiodes for Analog Optic Links

A Dissertation

Presented to
the faculty of the School of Engineering and Applied Science
University of Virginia

in partial fulfillment
of the requirements for the degree
Doctor of Philosophy

By

Yang Fu

December
2012

APPROVAL SHEET

The dissertation

is submitted in partial fulfillment of the requirements

for the degree of

Doctor of Philosophy

AUTHOR

The dissertation has been read and approved by the examining committee:

Dr. Joe C. Campbell

Advisor

Dr. Archie L. Holmes Jr.

Dr. Arthur W. Lichtenberger

Dr. Robert M. Weikle

Dr. Olivier Pfister

Accepted for the School of Engineering and Applied Science:

Dean, School of Engineering and Applied Science

December

2012

Copyright

by

Yang Fu

2012

This dissertation is dedicated to my parents, Jun and Li, for their love, support and guidance.

Acknowledgements

I would like to first and foremost thank my advisor, Professor Joe Campbell, for his constant guidance and support. He has given me a lot of freedom in my graduate study and instilled great confidence in me. I am extremely lucky to have Professor Campbell as my mentor both in research and life in general.

I would also like to acknowledge the support of other members of my advising committee. Professor Archie Holms' insightful advice and guidance have been very beneficial to me. Professor Arthur Lichtenberger and Professor Robert Weikle have enlightened me with their vast knowledge and expertise of microwave engineering and fabrication. Professor Olivier Pfister provides me with many valuable suggestions that helped me better present and defend my work. Working with all the professors in the advising committee has been a very rewarding experience for me.

I had the good fortune of enjoying the help and guidance of the postdocs and senior students after I joined Professor Joe Campbell's group. Members of the high-power photodetector group, Andreas Beling, Hao Chen, Huapu Pan and Zhi Li, taught me everything from device design to fabrication and characterization. They had been very patient with me as I wreaked havoc in the lab. I can never forget the numerous nights we spent together in the cleanroom making those tiny

photodiodes. I worked especially close with Huapu Pan and Zhi Li, who are also my best friends. Chong Hu and Handing Liu have been my guru through the course of my PhD study and I have learned a lot from them both inside and outside research. They are also wonderful skiing and PS3 game buddies. Dion McIntosh was like a big sister to me and always helped with any troubles in my graduate study. Xiaoguang Zheng shared his vast knowledge and experience in both scientific research and life with me. I really appreciate all of his valuable advices. Qiugui Zhou always has his insightful comments ready and I have learned a lot from interacting with him. Here I would also like thank Songbin Gong and Lihan Chen in Professor Scott Barker's group who have been immensely helpful in teaching me microwave design and measurements.

Other members of the group have also helped me on numerous occasions and made my graduate study a very enjoyable experience. Zhiwen Lu and I joined the group around the same time and we shared my ups and downs in research. The spirited discussions with Joe Murray, Lijun Li, Wenlu Sun and Yaojia Chen have been a constant source of inspiration for me. I would also like acknowledge Jinrong Yuan and Baile Chen in Professor Archie Holms' group for their help. I wish you all the best in your research endeavors.

I would like to thank Brenda Crider for all her kind help during the past four years. As the administrative assistant of our group, she has always been extremely helpful and patient. The research work would have been impossible

without her contribution. I want to thank our cleanroom stuff including Joe Beatrice, Alex Lobo, Harry Wade, Tim Pernell and Jie Wang for maintain all the instruments and providing a great working environment. I am also grateful for the help of other ECE staff members, including Eileen Thacker, Dan Fetko, Yadira Weaver, Gloria Walker, Susan Malone and Natalie Edwards.

I would like to acknowledge members of Dr. Scott Diddams' group at NIST, Jennifer Taylor, Haifeng Jiang, Tara Fortier and Frank Quinlan for introducing me to the ultra-stable photonic oscillator and achieving such great results. I want to thank Dr. David Tulchinsky and Dr. Keith Williams at NRL for their support of this work. I would also like to thank members of Professor John Bowers' group at UCSB for their great discussions and constant support. I want to thank Vincent Houtsma, Yves Baeyens, Rose Kopf and Liming Zhang at Alcatel-Lucent Bell Labs for making my internship there such an enjoyable experience.

I would be nowhere without my parents. They gave me the greatest gift of all while expecting nothing in return except my happiness. They support me in every aspect of my life and never burden me with expectations. I am forever grateful for their love.

Finally I want to thank my wife, Kejia Li, for her love, understanding and support through the years. This work would have been impossible without her. She remains ever willing to sacrifice to support me in my academic pursuits and gives me so many reasons to be happy. I am eternally grateful and looking

forward to spending the rest of our lives together.

Abstract

By transmitting and processing microwave signals over an optical carrier, analog optic links provide many advantages over electronic approaches, such as large bandwidth, low loss, immunity to electromagnetic interference (EMI), and lightweight cabling. The photodiodes used in the receivers of analog optic links need to be able to maintain high bandwidth, high power, and high linearity. The primary motivation behind this dissertation has been to study the power and linearity performance of high-power InGaAs/InP photodiodes with respect to both internal physical parameters and external microwave circuits. The knowledge gained from this study is to be applied for developing improved high-power photodiode designs.

Systematic characterizations and modeling of the bandwidth, impedance and third-order intermodulation distortion (IMD3) properties of the Modified Uni-Traveling Carrier (MUTC) photodiode are presented. Negative differential resistance (NDR) is found in the MUTC-4 photodiode under optical illumination and its origin is investigated using measurement and simulation tools. The electric-field-dependent responsivity caused by the Franz-Keldysh effect in the depleted InGaAs absorber in the MUTC photodiode with heavily doped absorber (HD-MUTC) has been identified as the primary contributor to nonlinear

distortions at low frequencies. Both the magnitude and the phase characteristics of IMD3 in HD-MUTC photodiodes can be well explained using the developed model, which also enables the design of a new high-linearity MUTC photodiode structure with graded-bandgap InGaAsP layer.

Wilkinson power combiners and resonance circuits have been monolithically integrated with high-power InGaAs/InP photodiodes to improve their power and linearity performance. A 6 dB OIP3 improvement has been demonstrated with the 4×1 combiner circuit and an improved 2×1 combiner circuit achieved over 50 dBm OIP3 at 20 GHz.

High-power MUTC photodiodes have been successfully incorporated into the NIST ultra-low phase noise optoelectronic oscillator (OEO) at 10 GHz; the result was 10 ~ 20 dB noise floor reduction. In order to optimize the high-power performance of MUTC performance in OEOs, large-signal impulse response measurements have been carried out. The amplitude-to-phase (AM-to-PM) conversion in the photodiode, a primary contributor to phase noise in OEOs, has been investigated and a physical explanation is provided for the zeros in AM-to-PM conversion factors.

Table of Contents

Chapter 1 Introduction 1

1.1 Analog optic link 1

1.2 Why high-power high-linearity photodiode? 6

1.3 PIN photodiodes 8

1.4 Photodiode performance metrics 11

1.4.1 Responsivity 12

1.4.2 Bandwidth 13

1.4.3 RF output power 14

1.4.4 Linearity 19

1.5 A brief review of high-power photodiode structures 22

1.6 Scope and organization of thesis 25

Chapter 2 High-Power MUTC Photodiode Design and Characterization 28

2.1 Overview 28

2.2 Epitaxial structure design 30

2.3 Geometry design 33

2.4 Device simulation *34*

2.5 Characterization techniques *34*

2.5.1 Current-Voltage (I-V) and Capacitance-Voltage (C-V) measurements 34

2.5.2 RF response measurement 35

2.5.3 S-parameter measurement 38

2.5.4 Linearity measurement 38

Chapter 3 Photodiode Fabrication Process 40

3.1 Metal deposition *40*

3.2 Mesa etching *42*

3.3 Oxide deposition and etching *43*

3.4 Au electro-plating *44*

3.6 Additional Processing *46*

3.7 Complete process flow *46*

Chapter 4 The High-Power Modified Uni-traveling Carrier (MUTC) Photodiode 48

4.1 Introduction *48*

4.2 The MUTC-4 photodiode *51*

4.2.1 Impedance analysis 52

4.2.2 Bandwidth measurement and discussion 62

4.2.3 Modeling MUTC-4 photodiode in Crosslight Apsys..... 73

4.2.4 The origin of negative differential resistance (NDR) 77

4.3 Summary 82

Chapter 5 MUTC Photodiode Array with Monolithically Integrated Wilkinson Combiner..... 84

5.1 Introduction..... 84

5.2 First generation circuits..... 88

5.2.1 Design and fabrication 88

5.2.2 S-parameter measurements 91

5.2.3 Frequency response measurements..... 95

5.2.4 Measurement and simulation of OIP3 97

5.3 Second generation circuits..... 104

5.3.1 Design and fabrication 104

5.3.2 S-parameter measurements 108

5.3.3 Bandwidth and linearity measurements 110

5.4 Summary 112

Chapter 6 Characterizing and Modeling MUTC Photodiode Nonlinearity.114

6.1 Introduction.....114

6.2 Responsivity and OIP3 measurements *115*

6.3 Nonlinear mechanisms in the MUTC photodiode *118*

6.4 The nonlinear model *120*

6.4.1 Electric field calculation 120

6.4.2 Franz-Keldysh effect 120

6.4.3 Impact ionization 122

6.4.4 Device temperature 123

6.4.5 Coupling of physical effects in the photodiode 124

6.4.6 Simulation procedure 125

6.5 Simulation results and discussion *127*

6.5.1 Responsivity versus wavelength 127

6.5.2 Responsivity versus electric field 128

6.5.3 Responsivity versus photocurrent 129

6.5.4 OIP3 versus photocurrent 130

6.6 IMD phase measurement and discussion *131*

6.7 Summary *134*

Chapter 7 High-Power Photodiode for Ultra-Low Phase Noise Microwave Signal Generation 136

7.1 Introduction *136*

7.2 Initial measurements at NIST *138*

7.3 Impulse response measurement at UVa *144*

7.3.1 Bandwidth and saturation analysis 146

7.3.2 The AM-to-PM conversion factor 154

7.4 Summary *161*

Chapter 8 Summary and Future Work 162

8.1 Summary *162*

8.2 Future Work *166*

8.2.1 High-linearity MUTC photodiode with graded-bandgap InGaAsP absorber 166

8.2.2 Integrated lumped element Wilkinson combiner with high-power photodiodes 170

Appendix I Parameters for Crosslight Apsys Simulation 175

Publication list 178

Bibliography 181

List of Figures

Figure 1.1 A simplified diagram of an optical link 2

Figure 1.2 Simplified local oscillator distribution system used in the ALMA radio telescope in Chile [13] 4

Figure 1.3 Schematic diagram of an OEO 5

Figure 1.4 Top (a) and back (b) illuminated PIN photodiodes. 9

Figure 1.5 Bandgap energy and lattice constant of common semiconductor materials used in optoelectronics. The superimposed color bands represent visible wavelengths [24]. 10

Figure 1.6 Different PIN photodiode structures [25]: (a) vertical-PD, (b) waveguide (WG-PD), (c) evanescently-coupled WG-PD, (d) distributed traveling-wave (TW) PD, and (e) periodic TW-PD.....11

Figure 1.7 The power transfer plot of a typical photodiode showing (a) compression and (b) expansion/compression 15

Figure 1.8 (a) Carrier and electric field distribution in a PIN photodiode under illumination (b) carrier transport properties of $\boldsymbol{In0.53Ga0.47As}$ at 300K [30]..... 16

Figure 1.9 Photodiode equivalent circuit 17

Figure 1.10 (a) The time-domain waveforms and (b) the loci of voltage and

current on the photodiode. 4V bias voltage and 80 mA average photocurrent is assumed for (b). 18

Figure 1.11 Frequency spectrum of a nonlinear system 20

Figure 1.12 Power transfer plot showing the definitions of SFDR and IP3 21

Figure 1.13 High-power photodiode structures: (a) conventional PIN-PD, (b) UTC-PD, (c) PDA-PD, (d) DDR-PD and (e) MUTC-PD [31]..... 22

Figure 2.1 The (a) energy band diagram and (b) epitaxial structure of the MUTC-1 photodiode..... 30

Figure 2.2 The (a) photomask design, (b) top-view microscope picture and (c) cross-section diagram (not to scale) of an MUTC photodiode. The structures in (a) and (b) measure approximately 400 μm × 200 μm. 33

Figure 2.3 The two-laser heterodyne setup [74] 35

Figure 2.4 The photodiode chip mounted on the thermal-electric cooler (TEC) for testing. 37

Figure 2.5 The three-tone IMD measurement setup [61] 38

Figure 4.1 RF output power of a 34-μm-diameter MUTC-4 device at 24 GHz versus photocurrent at reverse biases of 4-V, 5-V, and 6-V. The inset shows the −3 dB bandwidth for different photocurrent values (10, 50, 90, and 130 mA). [59]..... 49

Figure 4.2 (a) S11 and (b) its magnitude of a 40 μm MUTC4 photodiode bias at -5V. The photocurrent is increased from 0 mA to 70 mA 50

Figure 4.3 The epitaxial structure of the MUTC-4 photodiode [59] 51

Figure 4.4 The capacitance-voltage characteristics of MUTC-4 photodiode 53

Figure 4.5 Linear regression analysis of the photodiode capacitance 54

Figure 4.6 S11 of a28 μm-diameter MUTC-4 photodiode at -5V bias voltage and different photocurrent 55

Figure 4.7 The (a) resistance and (b) capacitance of a 28 μm-diameter MUTC-4 photodiode at -5 V from S-parameter measurements 58

Figure 4.8 Depletion width of MUTC-4 photodiodes at -5V estimated from capacitance data 61

Figure 4.9 Normalized resistance of MUTC-4 photodiode at -5V 62

Figure 4.10 Impulse response of 28 μm-diameter MUTC-4 photodiode at -5V. These waveforms do not include calibration for the cable assembly..... 64

Figure 4.11 Bandwidth summary for MUTC-4 photodiodes with different diameters at -5V 69

Figure 4.12 Carrier transit time's dependence on current density for MUTC-4 photodiode at -5V 70

Figure 4.13 The simulated (a) conduction band, (b) electric field and (c) electron velocity profiles of an MUTC-4 photodiode at different photocurrent and -5V bias voltage. 76

Figure 4.14 Comparison of measured and simulated transit-time of MUTC-4 photodiode at -5V 76

Figure 4.15 Measured (scatter points) and simulated (solid lines) series resistance of 28μm MUTC-4 photodiode at -5V 77

Figure 4.16 Measured (scatter points) and simulated (solid lines) series resistance of 28 μm diameter MUTC-4 photodiode at 90 mA photocurrent 78

Figure 4.17 Electric field profile in a 28 μm-diameter MUTC-4 photodiode at 90 mA photocurrent 79

Figure 4.18 The series resistance of a 28μm diameter MUTC-4 photodiode at -5V and 90 mA photocurrent. Simulation results assuming different material properties are compared with measurement. 81

Figure 4.19 The series resistance of a 28 μm-diameter MUTC-4 photodiode at -5V and 90 mA photocurrent. The p-type doping concentration in the undepleted InGaAs absorber is changed from 1/10 to 10 times its original value ($5\times10^{23}cm^{-3}$ to $2\times10^{24}cm^{-3}$). 82

Figure 5.1 Schematic diagram of a 2×1 Wilkinson power combiner. Z_0 is the system characteristic impedance. 85

Figure 5.2 The S-parameters of an ideal 2×1 Wilkinson power combiner with 20 GHz center frequency 87

Figure 5.3 The epitaxial structure of the HD-PDA photodiode [101] 88

Figure 5.4 The layouts of the (a) 2×1 Wilkinson power combiner with HD-PDA photodiode pair, (b) 2×1 Wilkinson power combiner without photodiodes, (c) open-stub tuner and the HD-PDA photodiode and (d) open-stub tuner

without photodiode. Dimensions: (a) and (b) 3.5 mm × 0.8 mm, (c) and (d) 1.3 mm × 0.5 mm. 89

Figure 5.5 (a) Structure A: HD-PDA photodiode with its electrical output signal directly coupled to testing CPW pads. (b) Structure B: HD-PDA photodiode with an open-stub tuning circuit, followed by the same CPW pads in (a), and (c) Structure C: two HD-PDA photodiodes with the same open-stub tuning circuits coupled to the two input ports of a Wilkinson power combiner. 90

Figure 5.6 Comparison of measured and simulated (a) S12 of the stub tuner in Error! Reference source not found.(d), (b) S12 and (c) S23 of the Wilkinson combiner with stub tuner (port-1 is the output port) in Error! Reference source not found.(b) 93

Figure 5.7 (a) S-parameters of the Ti thin film resistor and an ideal 100 ohm resistor, and (b) the resistance seen from both ports extracted from the S-parameter measurement. The inset in (a) shows the layout of the resistor test pattern. The 50 ohm resistance of the test ports has been subtracted from (b). 94

Figure 5.8 The S-parameters of Structure B (single photodiode with stub tuner) and C (photodiode pair with stub tuner and the 2×1 Wilkinson power combiner) 95

Figure 5.9 The frequency response measurement setup for the photodiode array.96

Figure 5.10 Relative frequency response of Structures A, B, and C measured at 1

mA photocurrent and 5V reverse bias. 97

Figure 5.11 Measured OIP3 of HD-PDA photodiodes with and without open-stub at 25 mA photocurrent and 8 V reverse bias. 99

Figure 5.12 The equivalent circuit model used for OIP3 simulation. 100

Figure 5.13 Simulation of the amplitude of the voltage swing versus frequency for 10 mA photocurrent. Solid and dashed lines are voltage swing amplitudes across the photodiode and the load resistor, respectively, for structure B. Dotted line: voltage swing amplitude across the load for structure A. 101

Figure 5.14 Frequency dependence of OIP3 improvement for Structure B compared with Structure A. 103

Figure 5.15 Epitaxial structure of the HD-MUTC photodiode [71]. 105

Figure 5.16 The layouts of (a) 4×1 Wilkinson combiner with 4-elecment photodiode array, (b) 4×1 Wilkinson combiner transmission test pattern, (c) 2×1 Wilkinson combiner and 2-element photodiode array and (d) 2×1 Wilkinson combiner transmission test pattern. Dimensions: (a) and (b) 3.0 mm × 1.0 mm, (c) and (d) 1.8 mm × 0.5 mm 107

Figure 5.17 Pictures of completed (a) 4×1 Wilkinson power combiner and 4-element photodiode array and (b) 2×1 Wilkinson power combiner and 2-element photodiode array. 108

Figure 5.18 The measured S-parameters of the (a) 4×1 Wilkinson power combiner and (b) 2×1 Wilkinson power combiner 110

Figure 5.19 The frequency responses of (a) 4×1 Wilkinson power combiner and 4-element photodiode array and (b) 2×1 Wilkinson power combiner and 2-element photodiode array. The bias voltage was -5 V for both measurements. 111

Figure 5.20 The OIP3 of (a) 4×1 Wilkinson power combiner and 4-element photodiode array and (b) 2×1 Wilkinson power combiner and 2-element photodiode array. The photocurrent used in (a) was 20 mA for discrete photodiode and 80 mA for the combiner. The bias voltage for both measurements was -9 V. 112

Figure 6.1 The epitaxial layer structure of an HD-MUTC photodiode 115

Figure 6.2 Responsivity's dependence on DC photocurrent and bias voltage of a 40-μm diameter HD-MUTC photodiode 116

Figure 6.3 Dependence of OIP3 on DC photocurrent and bias voltage. (a) 80% modulation depth and (b) 25% modulation depth.....117

Figure 6.4 The average electric field in the InGaAs absorber at different bias voltages and photocurrent levels. 120

Figure 6.5 Estimated device temperature at different bias voltages and photocurrent levels. 123

Figure 6.6 Block diagram of physical effects that contribute to nonlinearities at low frequencies (300MHz). 124

Figure 6.7 Simplified flowchart of the simulation program 126

Figure 6.8 Simulated wavelength and electric field dependence of responsivity at 300K. 127

Figure 6.9 Simulated responsivity versus electric field in the depleted InGaAs absorber. (solid lines: with impact-ionization, dashed lines: without impact-ionization) 128

Figure 6.10 Responsivity versus DC photocurrent under different bias voltages. (solid line: simulation, scattered: measurement) 129

Figure 6.11 OIP3 versus DC photocurrent at -4V (solid line: simulation, scattered: measurement) 130

Figure 6.12 OIP3 versus photocurrent at -8V (solid line: simulation, scattered: measurement) 130

Figure 6.13 The IMD phase measurement setup 132

Figure 6.14 The measured OIP3 and relative phase of the upper IMD3 product (IMD3U) for MUTC photodiode at different dc photocurrents and bias voltages. 133

Figure 7.1 Optical frequency division for low phase noise microwave generation [37] 139

Figure 7.2 Time domain waveform and frequency spectrum of the oscillator ... 139

Figure 7.3 SSB phase noise comparison of leading microwave oscillators in the 10 GHz range [37] 140

Figure 7.4 (a) Impulse response of a 34 μm MUTC-4 photodiode at 8.9 mW

optical power and (b) corresponding saturation plot 141

Figure 7.5 RF output power at 10 GHz of a 34-µm MUTC-4 photodiode..... 142

Figure 7.6 The phase bridge setup used to measure the AM/PM conversion factor [37, 121]..... 143

Figure 7.7 AM/PM conversion factors of (a) a 34-µm MUTC-4 photodiode and (b) commercial photodiodes previously used in the system [121] 143

Figure 7.8 The residue phase noise of 34-µm MUTC-4 photodiode at -9 V..... 144

Figure 7.9 Impulse response waveforms of a 20-µm diameter MUTC-4 photodiode at (a) -5 V, (b) -13 V and (c) -21 V bias voltages. The average photocurrent in each plot is changed from 50 µA (light green) to 1 mA (black) in 50 µA steps. A more intense the color, the larger the average photocurrent. 147

Figure 7.10 The electrical pulse energy of the impulse response of a 20-µm diameter MUTC-4 photodiode at different bias voltages and average photocurrent. 149

Figure 7.11 The 3-dB bandwidth calculated from the impulse response waveforms of (a) 20-µm, (b) 28-µm, (c) 40 µm and (d) 56 µm diameter MUTC-4 photodiodes at different bias voltages and average photocurrent. 153

Figure 7.12 The (a) phase, (b) AM-to-PM conversion factor, and (c) RF power of different harmonics for a 20-µm diameter MUTC-4 photodiode at -9 V bias voltage. The 3dB bandwidth is also shown in (c). 156

Figure 7.13 The AM-to-PM conversion factor of a 20-μm diameter MUTC-4 photodiode at 10 GHz and its bandwidth at different bias voltages. Dashed lines indicate positions of the zeros in the AM-to-PM conversion factor... 158

Figure 7.14 The measurement results for different size MUTC-4 photodiodes at 10 GHz and -21 V bias voltage: (a) AM-to-PM conversion factor and (b) RF power. The 3-dB bandwidth for each photodiode measured at -21 V is also included in the upper half of (a). Dashed lines in (a) mark the positions of zeros in the AM-to-PM conversion factors. 161

Figure 8.1 Calculated responsivity of depleted InGaAsP absorber with different bandgaps. Bias voltage = -7 V, modulation depth = 80%, light wavelength = 1543 nm 167

Figure 8.2 Calculated responsivity of InGaAsP absorber with two different bandgap layers, 0.74 eV and 0.76 eV. 168

Figure 8.3 The calculated OIP3 value of three graded-bandgap absorber designs. The depleted absorber in each design is made up by InGaAsP layers with two different bandgaps. The OIP3 of a single bandgap absorber design (HD-MUTC) is included for comparison. 169

Figure 8.4 The epitaxial structure design of MUTC photodiode with graded-bandgap InGaAsP absorber. 170

Figure 8.5 A broadband Wilkinson power combiner design realized in (a) distributed form and (b) lumped element form. 172

Figure 8.6 Lumped element Wilkinson power combiner in Ansoft HFSS 173

Figure 8.7 Simulated S-parameters of the lumped element Wilkinson combiner. 174

List of Tables

Table 4.1 Summary of MUTC-4 photodiode impedance at -5V 59

Table 4.2 Bandwidth summary of MUTC-4 photodiode at -5V 67

Table 5.1 OIP3 comparison between Structure B and C at 20 GHz. 104

Table 6.1 Values of model parameters 122

Chapter 1 Introduction

Fiber optics is the science and engineering field concerned with transmission and processing information by using optic fiber. Compared with other transmission media, optic fiber has the major advantages of low loss, low dispersion, and high bandwidth [1]. Other desirable properties of optic fiber include high immunity to electromagnetic interference (EMI), light weight, and compact size, as well as mechanical flexibility. Fiber optics have been widely used to transmit information over distances ranging from thousands of kilometers in telecommunication systems down to a few meters in high-speed computer interconnections [2]. The maturity and commercial availability of photonic components including lasers, modulators, amplifiers and detectors brought about by the widespread deployment of fiber optics have enabled many new applications in areas traditionally dominated by electronics, such as analog transmission links [3-7].

1.1 Analog optic link

An optical link combines optically encoded electrical signals with an optical carrier. Figure 1.1 shows an example of a simple optical link. On the

transmitter side, the input electrical signal is imposed on the light from a laser through a modulation device. The optical fiber transmits the signal-bearing lightwave from one location to another. Optical amplification may be incorporated in the signal path to boost its strength. At the receiver end, a photo-detection device such as a photodiode is used to demodulate the electrical signal from the optical carrier. Depending on the fashion of signal modulation and detection, optical links fall into two major categories. Intensity modulation direct detection (IMDD) systems use the intensity of the optical carrier to convey signal information and the demodulation is completed by direct square-law photo-detection. In a coherent system, the phase and frequency of the optical carrier are also used to transfer information. The demodulation process is more complicated than in an IMDD system since the optical phase or frequency information is lost during the square-law detection by a photodiode (PD). The received signal needs to be mixed with an optical local oscillator (LO) in order to be detected.

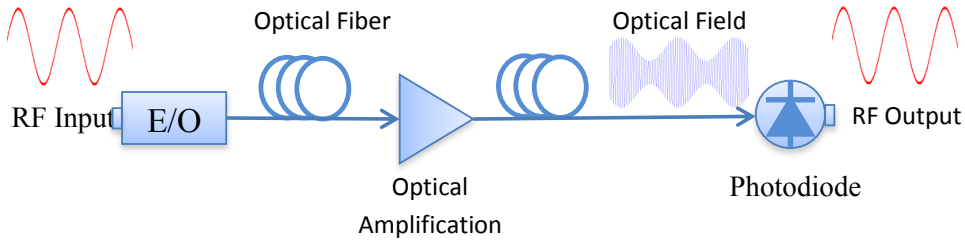

Figure 1.1 A simplified diagram of an optical link

While digital links constitute the majority of fiber optic links deployed

around the world, there are a growing number of applications for their analog counterparts, especially when there is a need to transmit and process electrical signals with high fidelity, power, or speed over a relatively short range (a few meters to tens of kilometers) [4, 6]. The initial commercial deployment of analog optical links has been for video distribution in CATV services [8, 9]. Replacement of point-to-point microwave links is another important application for analog optical links, which can have lower insertion loss than microwave links at distances as short as a few meters [5]. Their light weight and compactness are major attractions for systems where bulk is a concern, such as in shipboard or avionic applications [9]. In antenna remoting, a high fidelity and high power microwave signal is transmitted between an antenna and a central station via an analog optic link so that the complexity of instruments at the remote locations (on top of ship mast or in a difficult terrain) can be greatly reduced [6, 10]. Analog optic links are also used in beam-forming networks for phased array antennas to provide true time delay [11, 12]. Local oscillator signals over 100 GHz can be distributed to individual antennas for radio telescopes using analog optic links [13, 14].

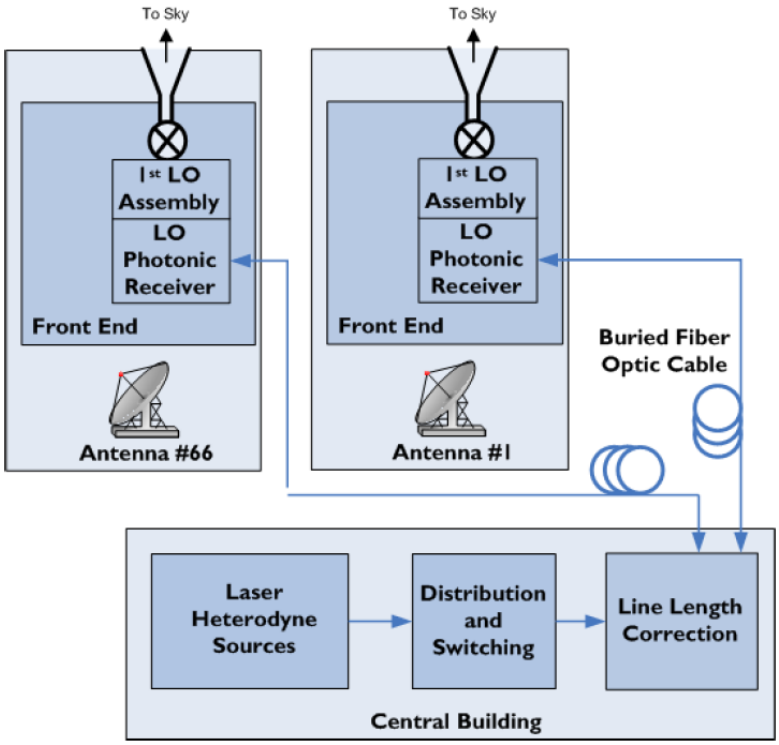

Figure 1.2 Simplified local oscillator distribution system used in the ALMA radio telescope in Chile [13]

Other than applications focused on signal transmission, photonic processing of microwave signals also uses analog optic links [15]. Examples include photonic delay lines [16], filtering [7, 15, 17], arbitrary waveform synthesis [18], A/D conversion [19, 20] and optoelectronic oscillators (OEO) [21, 22]. Here, we focus on the OEO because it is involved in a latter part of this dissertation. An oscillator is an indispensable component in virtually all modern electronic systems. Most of electronic oscillators rely on high-Q quartz crystal resonators to achieve high spectral purity. However the performance of crystal

oscillators degrades with increasing frequency due to either reduced resonator Q value or the phase noise introduced by frequency multiplication. An optoelectronic oscillator (OEO) can produce an ultra-stable microwave signal at high frequencies (up to tens of GHz) by taking advantage of the low-loss properties of optical resonators, such as long fiber delay lines, Fabry–Pérot cavities, and whispering gallery mode resonators (WGMR). Many OEOs take the form of a transposed gain oscillator (TGO), while others use a dual-mode laser or an optical frequency division technique. The fact that OEOs generate microwave signals in both the electrical and optical domains makes them especially suitable for integration with other photonic systems. Figure 1.3 shows a schematic diagram of an OEO based on the transposed gain approach.

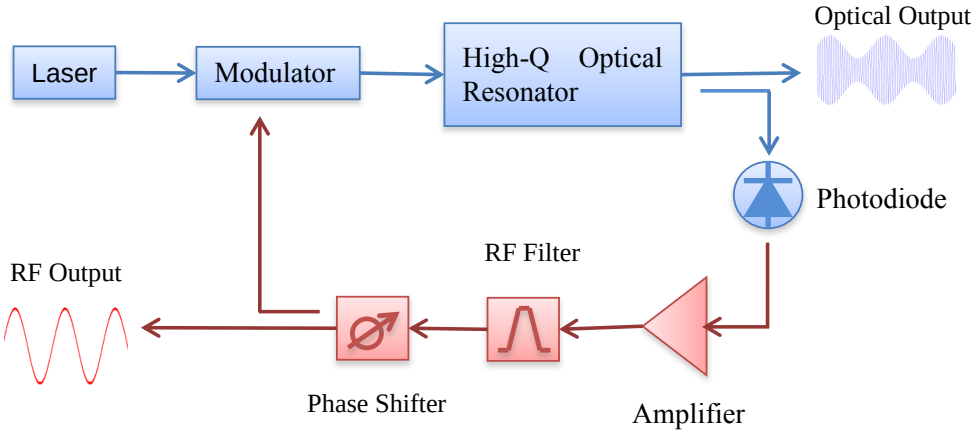

Figure 1.3 Schematic diagram of an OEO

1.2 Why high-power high-linearity photodiode?

The primary figures of merit for an analog optic link are gain (G), spurious-free dynamic range (SFDR), and noise figure (NF) [5-7, 10]. The link gain is the ratio of output RF power delivered to the load to the input RF power required. The SFDR is defined by the difference between the minimum input power that is above the noise floor and the maximum input power where all the distortions stay below the noise floor. The SFDR represents the usable input power levels over which an accurate and detectable signal can be transmitted through the system. The noise figure is the change in the signal-to-noise ratio from the system input to the output. Obviously analog optic link designs need to maximize both link gain and SFDR while keeping the noise figure as small as possible.

Among other factors, the amount of optical power or photocurrent the photodiode (PD) can handle has a large impact on the link performance. V. J. Urick et al. [6] have provided an excellent analysis of this subject. The figures of merit for a typical IMDD link can be related to the photocurrent using the following equations [6]:

$$G_{RF} = \pi^2 \left(\frac{I_{photo}^2}{V_\pi^2} \right) R_{in} R_{out} \,. \tag{1.1}$$

$$SFDR_3 = \left(\frac{4I_{photo}^2 R_{out}}{N_{out} B_{RF}}\right)^{\frac{2}{3}}. \tag{1.2}$$

$$NF_{RF} = \frac{V_\pi^2 N_{out}}{I_{photo}^2 \pi^2 R_{in} R_{out} k_B T}. \tag{1.3}$$

where I_{photo} is photocurrent of the PD, V_π is the half-wave voltage of the modulator, R_{in}, and R_{out} are the input and output resistance of the link, respectively, N_{out} is the noise power spectral density at the system output, and B_{RF} is the RF bandwidth. We can see that both the link gain and SFDR increase as the system can handle larger photocurrent, while the noise figure decreases. Moreover, large photocurrent and RF output power from the photodiode can eliminate the need for electronic amplifiers and their corresponding contributions of noise and distortion to the system.

In addition to high-power handling capability, the photodiode an analog optic link also needs to have high-linearity in order to avoid introducing excessive distortion during the photo-detection process. The equations above assume that the photodiode is perfectly linear. In reality, all electronic devices tend to be more nonlinear with increasing power. It is beneficial, therefore, for the photodiode to be able to handle high power while maintaining high linearity.

1.3 PIN photodiodes

The most common type of photodiode used in optical communications is the PIN photodiode, which is also the basis for many advanced photodiode designs. The PIN photodiode consists of an intrinsic layer, sandwiched between heavily doped n-type and p-type layers. The built-in potential and applied bias voltage establish the electric field in the depletion region. Only photons with energies larger than the semiconductor bandgap are able to generate electron-hole pairs. The carriers generated within the depletion region are swept across the region by the internal electric field, while the carriers generated in the p- or n-type doped regions rely on diffusion before reaching the depletion region. The terminal current consists of contributions from both the conduction current and the displacement current induced by the moving charges. A simplified diagram of the PIN photodiode is shown in Figure 1.4. Insertion of the intrinsic layer between the p-type and n-type regions increases the absorption volume and reduces the junction capacitance. Therefore, the PIN photodiode exhibits higher quantum efficiency and larger bandwidth than the PN photodiode.

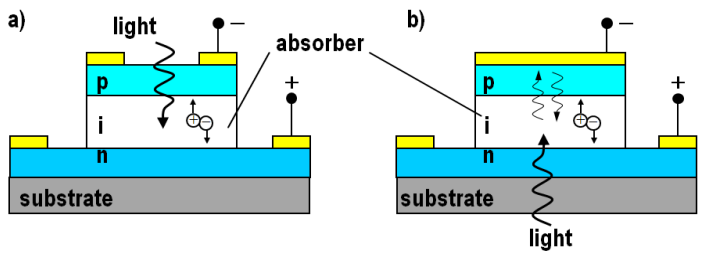

Figure 1.4 Top (a) and back (b) illuminated PIN photodiodes.

The InGaAs/InP material system is widely used for optical communication applications. $In_{0.53}Ga_{0.47}As$ (which will be referred to as InGaAs for simplicity in this dissertation) is lattice matched to InP and has a bandgap energy of 0.74 eV (1.68 μm) at 300 K [23]. It is well suited for optical absorption in the 1.3 μm and 1.55 μm transmission windows in optical fibers. InP works as an IR-transparent layer due to its larger bandgap (1.34 eV at 300 K). The electron velocity overshoot in both InGaAs and InP can help to increase the device speed. Ge has similar bandgap energy but suffers from higher leakage current. Its major advantage is the monolithic integration with Si components.

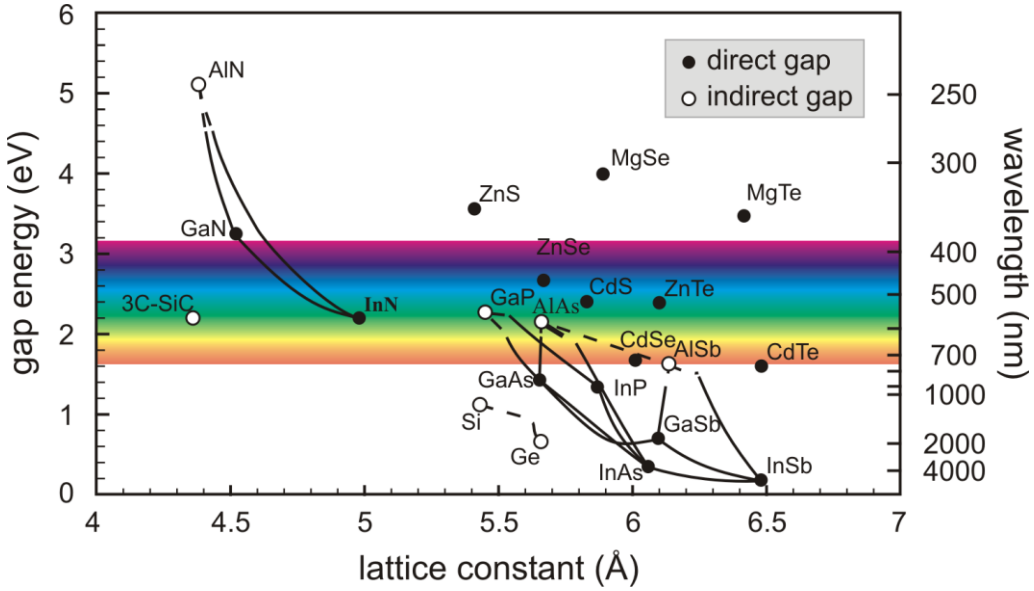

Figure 1.5 Bandgap energy and lattice constant of common semiconductor materials used in optoelectronics. The superimposed color bands represent visible wavelengths [24].

Depending on the optical coupling scheme, PIN photodiodes can be divided into two major categories: vertically-coupled (surface-normal) PDs and waveguide-coupled (WG) PDs [25]. A vertically coupled PD is usually easier to design, fabricate, and achieve uniform absorption. However, it suffers from a performance trade-off between speed and efficiency due to the parallel direction of optical illumination and charge carrier transport. The waveguide-coupled PD avoids this problem by changing the direction of lightwave propagation and has the added benefit of easy planar integration with other photonic components. However, it is more complex and absorption tends to be non-uniform along the length of the PD. As we will see in the next section, uniform absorption is very

important in order to achieve high-power operation. This dissertation will focus on the vertically-coupled photodiodes. Different PIN photodiode structures are shown in Figure 1.6.

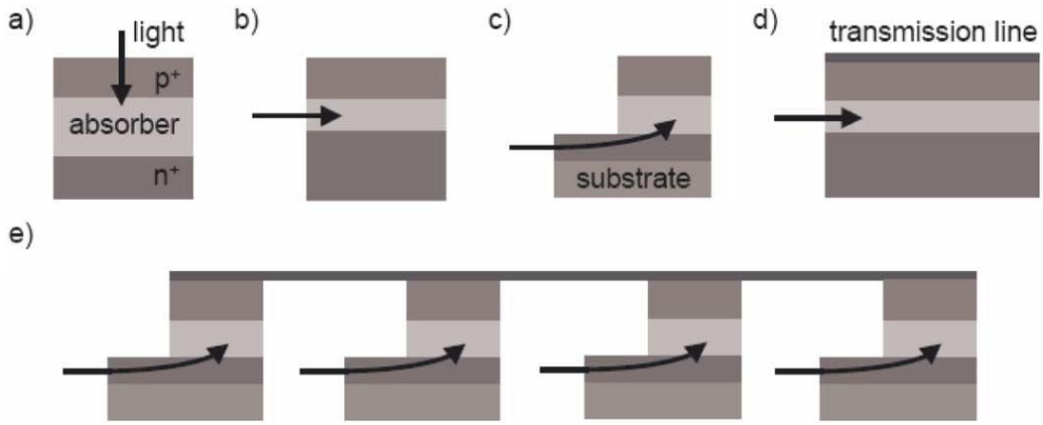

Figure 1.6 Different PIN photodiode structures [25]: (a) vertical-PD, (b) waveguide (WG-PD), (c) evanescently-coupled WG-PD, (d) distributed traveling-wave (TW) PD, and (e) periodic TW-PD

The conventional PIN photodiode has its limitations with respect to its high-power characteristics. Space charge [25-27], load feedback [26], and thermal [27, 28] effects are fundamental mechanisms that limit the photodiode performance under intense optical illumination. Trade-offs exist between various design parameters restricting further improvements. This is the motivation for advanced photodiode structure development.

1.4 Photodiode performance metrics

This section discusses the primary performance metrics for photodiode characterization. Their implications for photodiode design are also included.

1.4.1 Responsivity

The responsivity (R) is defined as the ratio of the photocurrent to the incident optical power in the units of A/W. For a vertically illuminated photodiode, the responsivity can be calculated by

$$R = \frac{I_{ph}}{P_{opt}} = \frac{\eta_{ext}\lambda\ [\mu m]}{1.24} \text{ and } \eta_{ext} = (1 - \mathrm{R}_{surface})(1 - e^{-\alpha d})$$

where I_{ph} is the photocurrent, P_{opt} is optical power, η_{ext} is the external quantum efficiency, λ is the light wavelength, $R_{surface}$ is the surface reflectivity, and α and d are the absorption coefficient and thickness of the absorber, respectively. The above equation assumes single-pass light absorption and 100% carrier collection. The absorption coefficient for InGaAs at 1.55 μm and 300 K is about 7000 cm^{-1} [23]. Therefore, 2 μm-thick InGaAs is needed to absorb 80% of the incident light. The maximum achievable responsivity (assuming no gain) at 1.55 μm is 1.25 A/W which corresponds to 100% external quantum efficiency. Methods to increase responsivity for photodiode include using thicker absorbers, anti-reflection (AR) coatings, optical resonant-cavities, and structures with internal gain such as the avalanche photodiode (APD).

1.4.2 Bandwidth

Bandwidth is used to describe the operational speed of a photodiode in terms of frequency response. The photodiode can be regarded as a low-pass system and the 3-dB bandwidth is defined as the frequency at which the output RF power decreases from its low-frequency value by 3 dB.

RC-time constant and carrier transit time are the two primary bandwidth limitations for a PIN photodiode. The junction capacitance, C_{pd} , of the photodiode forms a first-order RC circuit with the effective resistance, R_{eff}, in parallel. The load resistor, R_{load}, which is typically 50 ohm, and the series resistance of the photodiode, R_{pd}, are the two primary contributors to R_{eff}. Other parasitic impedance components in the photodiode are usually much smaller than C_{pd} and R_{load}. The RC-limited bandwidth f_{RC} is given by the expression,

$$\boldsymbol{f_{RC} = \frac{1}{2\pi R_{eff} C_{pd}}} \quad . \tag{1.4}$$

The carrier transit time is the time required for the photo-generated electrons and holes to travel through the intrinsic region and reach their respective contacts in order to be collected. Assuming uniform generation, the transit time limited bandwidth for a PIN photodiode can be estimated by [29]

$$\boldsymbol{f_{tr} = \frac{3.5\bar{v}}{2\pi d}} \tag{1.5}$$

where d is the thickness of intrinsic region and $\bar{v}$ is the average carrier velocity. Combining the RC and transit-time components, the 3-dB bandwidth is given by

$$f_{3dB} = \frac{1}{\sqrt{\frac{1}{f_{RC}^2}+\frac{1}{f_{tr}^2}}} \quad . \tag{1.6}$$

There are trade-offs between these two bandwidth-limiting mechanisms and the responsivity of the PIN photodiode. A thick absorption layer provides large responsivity and small junction capacitance but increases the carrier transit time, which results in a reduction in bandwidth. A thin absorption layer, on the other hand, can increase the junction capacitance, which frequently limits the bandwidth. Reducing the active area of the PIN photodiode lowers the capacitance while maintaining the same carrier transit time, but this usually results in increased series resistance and its power handling capability suffers as well. A 50 ohm parallel resistor can be added to the photodiode in order to reduce the RC time by ~50% and increase the bandwidth. This is achieved, however, at the expense of half of the photocurrent. These design trade-offs and possible solutions will be discussed in greater detail in Chapter 2.

1.4.3 RF output power

The RF output power is defined as the AC power delivered to the load resistor, which is usually 50 ohm. Assuming a single-frequency sinusoidal signal, the photocurrent can be express as

$$I_{ph}(t) = I_{DC} + I_{AC} = I_{avg} + \tag{1.7}$$

$$\alpha I_{avg}\cos(2\pi f t) \quad .$$

where t is time, I_{avg} is the average photocurrent or DC component, α is the modulation depth, and f is the signal frequency. Since the load is usually connected to the photodiode through a bias tee or dc block, only the second term or the AC component is delivered to it. The RF power is expressed as

$$P_{Load} = \frac{1}{2} I_{AC}^2 R_{Load} \quad . \tag{1.8}$$

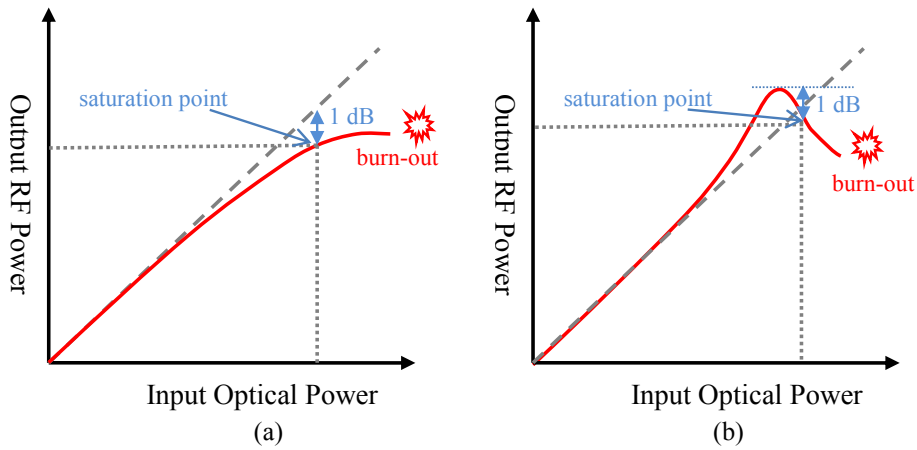

Figure 1.7 The power transfer plot of a typical photodiode showing (a) compression and (b) expansion/compression

The power transfer characteristic of a typical photodiode is plotted in Figure 1.7. At a given frequency, the output power of a photodiode first increases linearly when the input optical power is increased from a low level. However the power transfer curve gradually deviates from the linear response as the input optical power continues to increase. This phenomenon is referred to as "expansion" if the output power exceeds the ideal line and

"compression/saturation" if it falls below it. All physically realizable devices would enter saturation eventually due to either supply/breakdown voltage limit or thermal failure. In order to evaluate the photodiode power handling capability, the 1-dB saturation point is defined as the point where the power transfer curve drops below the ideal line by 1 dB. The corresponding RF output power and average photocurrent are referred to as the saturation power and saturation current, respectively. Some devices exhibit significant expansion behavior prior to the onset of compression. For these devices, the 1-dB saturation point is defined as the point where the power curve drops below the maximum expansion point by 1 dB.

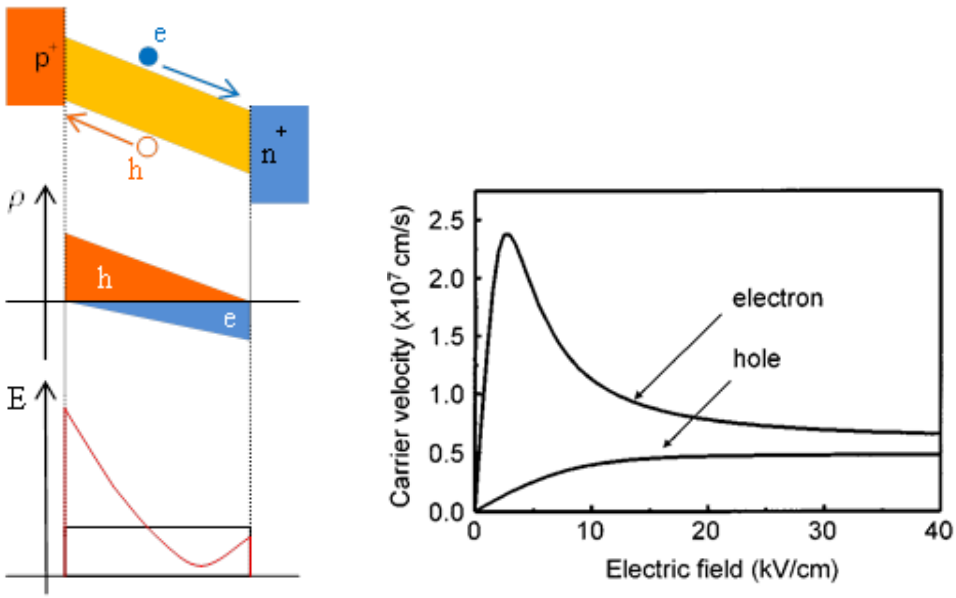

(a) (b)

Figure 1.8 (a) Carrier and electric field distribution in a PIN photodiode under illumination (b) carrier transport properties of $In_{0.53}Ga_{0.47}As$ at 300K [30]

There are many factors that contribute to the saturation behavior of a PIN, the space-charge effect [25, 26, 31, 32] being the most important. Figure 1.8 (a) shows the spatial distribution of the photo-generated carriers as they transit the depletion layer and the corresponding electric field. The electric field generated by the free carriers, i.e., the space-charge field, works against the field established by ionized dopants and the applied bias voltage. This is referred to as the "field-screening" effect. As a result, the total electric field in the depletion region drops to almost zero at high current densities. Once this occurs, the carrier transit time increases significantly and RF power output suffers from compression/saturation. The saturation problem is more severe in a photodiode structure with heterojunctions, since the carriers may not have sufficient energy to overcome the heterojunction barriers after the electric field collapses.

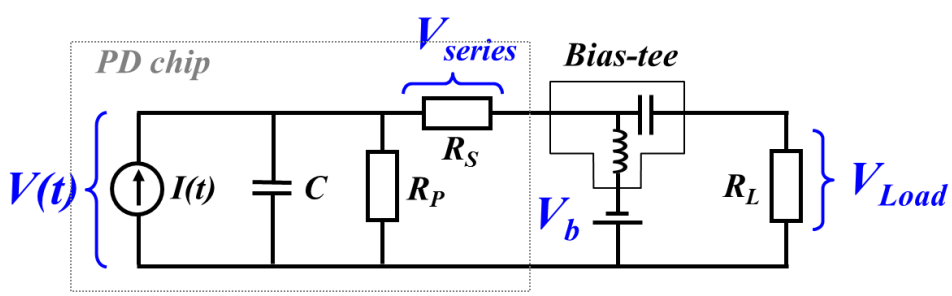

Figure 1.9 Photodiode equivalent circuit

The loading effect also plays an important role in determining the saturation current. Figure 1.9 shows the photodiode equivalent circuit. The AC voltage swing across the load is superimposed on the DC voltage bias applied to the photodiode, as illustrated in Figure 1.10. The photodiode stays at its quiescent

point (4V and 80 mA in Figure 1.10 (b)) when the light intensity is constant. When there is AC signal present, the operating point of the photodiode moves along the straight load line (without reactance) or the ellipses (with reactance) [33], causing the effective bias on the photodiode to change. This change is negligible when the photodiode works in the small-signal region. Under large signal operation, however, the effective bias voltage can be reduced substantially when the instantaneous current is larger than its average value, and pushes the photodiode towards saturation. The photodiode is easier to saturate when driving a larger load resistor. Increasing the bias voltage mitigates the loading effect, but is ultimately limited by the device breakdown voltage and thermal effects.

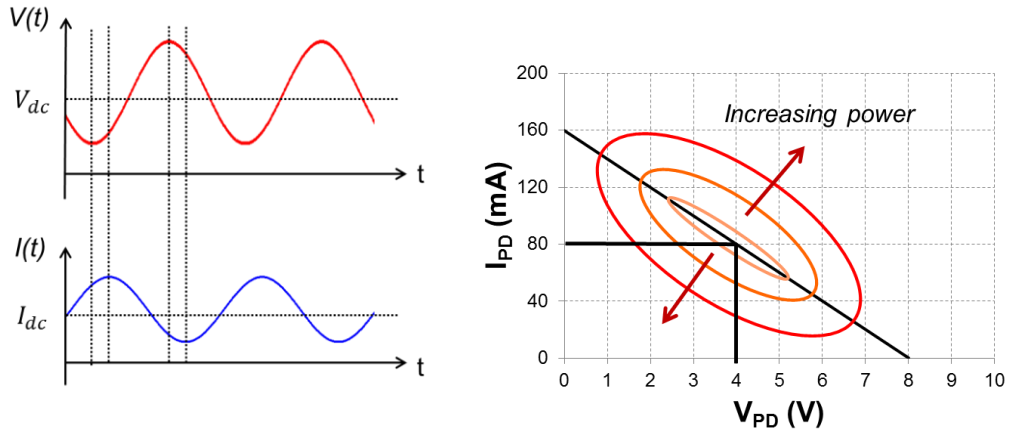

(a) (b)

Figure 1.10 (a) The time-domain waveforms and (b) the loci of voltage and current on the photodiode. 4V bias voltage and 80 mA average photocurrent is assumed for (b).

The distribution of charge carriers and the electric field inside the photodiode is not always uniform. If the light is focused on a portion of the photodiode active area and it will create a high local carrier concentration. This

usually results in early saturation of the photodiode. Also, current crowding due to high resistance in the contact layers causes a lateral potential drop on the device that exacerbates saturation.

1.4.4 Linearity

Linearity describes the extent to which the output of a system follows its input without distortion. The photodiode nonlinearity has a direct impact on the spurious free dynamic range (SFDR) of an analog optic link [34, 35]. Phase distortions can also be introduced by photodiode nonlinearity and limit the performance of systems that require precision timing, such as photonic ADCs [36] and optoelectronic oscillators [21, 37].

The nonlinear distortion phenomenon in photodiodes was first studied by Ozeki and Hara in 1976 [38]. Esman [39], Williams [40] and Humphreys [41] pioneered the work on characterization of intermodulation distortion (IMD) and harmonic distortion (HD) in PIN photodiodes in the 1980s and 1990s. Early efforts at nonlinearity modeling include the numerical studies by Williams [40] and Dentan and de Cremoux [42] based on carrier drift/diffusion (DD) transport mechanisms. Since then, there has been growing interest in nonlinearity study and developing high-linearity photodiodes.

Many physical mechanisms could potentially contribute to the nonlinear

behavior of photodiodes, including carrier velocity modulation [40], carrier recombination [43], nonlinear capacitance [44, 45], resistance [45], and nonlinear responsivity [46]. Optical effects such as refractive index change due to electric field and carrier concentration [47, 48] are also capable of producing nonlinear response under certain conditions. Device heating [49] and circuit loading effects play important roles in photodiode nonlinearity as well. The fact that most of these mechanisms are interrelated makes nonlinearity study an even more complicated task.

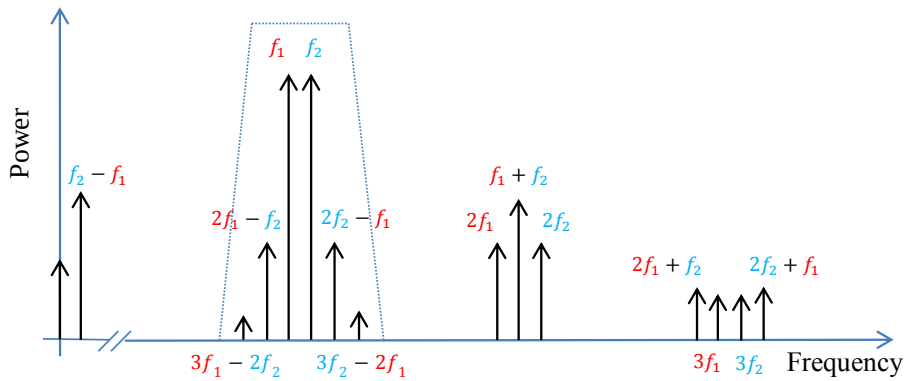

Figure 1.11 Frequency spectrum of a nonlinear system

Different kinds of nonlinear distortions exist in the output of a system when it is excited by an input signal, as shown in Figure 1.11. The third-order intermodulation distortions, IMDs or IMD3s, are considered the most troublesome. This is due to the fact that usually the IMD3s are the largest nonlinear distortion products that fall in the vicinity of the fundamental frequencies or the pass band of the system [50, 51].

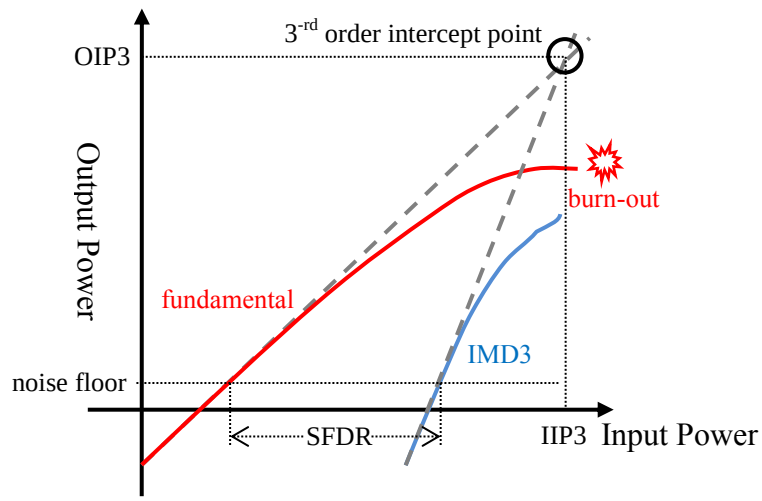

Figure 1.12 Power transfer plot showing the definitions of SFDR and IP3

The third-order intercept point (IP3) is the figure of merit that is widely accepted for characterizing weakly nonlinear systems. At the fundamental frequency, the output power of the system grows by 1 dB for every 1 dB increase in the input power until the system goes into a strongly nonlinear region. This relationship appears as a straight line with slope of 1 on the power transfer plot, while the IMD3 line has a slope of 3 as shown in Figure 1.12. The linear extrapolations of these two lines intercept at a point referred to as the third-order intercept point (IP3). In the weakly nonlinear region, the OIP3 can be calculated by [35]

$$\boldsymbol{OIP3 = P_f + \frac{1}{2}(P_f - P_{IMD3})} \quad . \tag{1.9}$$

where P_f is the power of fundamental frequency, P_{IMD3} is the power of the IMD3, both in units of dBm. The photodiode linearity will be studied in Chapter 6.

1.5 A brief review of high-power photodiode structures

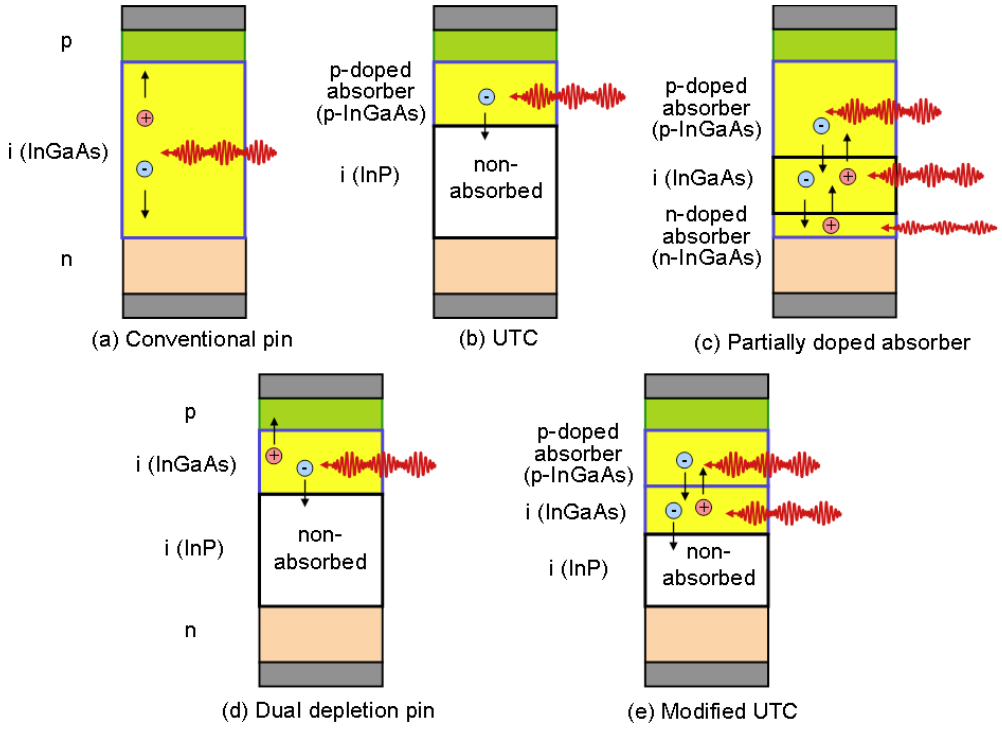

Figure 1.13 High-power photodiode structures: (a) conventional PIN-PD, (b) UTC-PD, (c) PDA-PD, (d) DDR-PD and (e) MUTC-PD [31]

Over the years, many photodiode designs focused on high-power operation have been developed, including the partially depleted absorber (PDA) photodiode [26, 32, 52], the dual depletion region (DDR) photodiode [53, 54], uni-traveling carrier (UTC) photodiode [31, 55-57], the modified UTC (MUTC)

photodiode [58-61], and the near-ballistic UTC (NB-UTC) photodiode [62, 63]. Figure 1.13 compares the epitaxial structure design, light absorption, and carrier transport in different high-power photodiodes.

The PDA photodiode design reduced the intrinsic InGaAs layer thickness in order to mitigate space-charge effect, while adding an undepleted InGaAs absorber in order to keep the responsivity the same as that of a conventional PIN photodiode. The PDA photodiode also has better charge balancing in the intrinsic layer than a PIN, which can increase the saturation current [64], since the carrier injection from the undepleted layers can be controlled independently. 48 GHz bandwidth and 24 mA saturation current from PDA photodiode has been reported [32].

The DDR photodiode design inserts a transparent InP depletion layer between the InGaAs absorber and the n-type quasi-neutral region. It reduced the junction capacitance while maintaining the same hole transit time as an InGaAs PIN. The electrons do need to traverse a longer distance in this structure, but they have higher drif velocity than holes. Therefore, the total transit time is not affected significantly and the device bandwidth is increased. 50 GHz bandwidth and 0.7 A/W responsivity of a DDR photodiode has been published [65]. Another DDR design with integrated GRIN lens for more uniform illumination achieved 45 mA saturation current at 10 GHz [66].

The UTC photodiode design relies on undepleted p-type InGaAs for light

absorption and intrinsic InP for depletion region. It is so named because only electrons need to travel through the whole structure, since the holes are generated directly in the p-type region and collected within the dielectric relaxation time (<0.1 ps). The fact that electrons can maintain relatively high drift velocity at low electric field enables UTC photodiodes to operate at high speed and high saturation current. A UTC photodiode with bandwidth up to 220 GHz has been demonstrated [67]. A p-type charge layer can be added between the InP collector and the n-contact layer to control the electric field in the InP, in such a way that electrons can travel at the overshoot velocity over a significant portion of the InP collector. This variation of the UTC photodiode has been named near-ballistic UTC-PD and has achieved 120 GHz bandwidth and 25 mA saturation current [68].

The modified UTC (MUTC) photodiode can be viewed as the combination of all the device structures mentioned above and provides greater flexibility in design optimization. An MUTC photodiode with 24 GHz bandwidth and 144 mA saturation current has been developed in our group [59]. It is the focus of my PhD study. The MUTC photodiode working principle and design considerations will be discussed in greater detail in Chapter 2.

1.6 Scope and organization of thesis

The main objectives of this thesis are:

1. To understand the frequency response of high-power MUTC photodiode in both continuous-wave (CW) and pulse operations.
2. To develop a physics-based model for analyzing the magnitude and phase of intermodulation distortion products in the MUTC photodiode.
3. To demonstrate the feasibility of using integrated microwave circuitry with high-power MUTC photodiode for power and linearity improvement.
4. To understand the requirements of high-power photodiodes for precision timing applications and demonstrate their value for ultra-low phase noise optoelectronic oscillators (OEOs).

The thesis describes my attempts to achieve these objectives. My main contributions are:

1. The development of a software model to explain the frequency response and impedance of the MUTC photodiode and the discovery of negative differential resistance (NDR) under optical illumination.
2. The development of a physics-based model for analyzing third-order intermodulation distortions (IMD3s) in MUTC photodiodes at low frequencies and the development of an experimental setup and technique for characterizing the phase of IMD3s.

3. The demonstration of MUTC photodiodes monolithically integrated with a Wilkinson power combiner and a resonance circuit at 20 GHz with improved power and linearity performance.
4. The achievement of record-low (-170 dBc) phase noise at 10 GHz with a NIST OEO that incorporates the high-power MUTC photodiode and determination of mechanisms responsible for zero phase distortion phenomenon in the MUTC photodiode.

The thesis is divided into eight chapters. Chapter 1 introduces the background of high-power photodiode research and reviews the fundamentals of PIN photodiodes as well as the state of high-power photodiode development. Chapter 2 describes design considerations for the MUTC photodiode, which is the device focus of this study. Characterization techniques and measurement setups are also discussed. The fabrication process is described in Chapter 3. In Chapter 4, the frequency response and impedance of the MUTC-4 photodiode are systematically characterized. Device parameters are extracted to establish a software model. The origin of the NDR is investigated using both measurement and simulation tools. Chapter 5 presents the design, fabrication and characterization of monolithically integrated MUTC photodiodes and microwave circuitry (Wilkinson power combiner and resonance circuit). Chapter 6 describes the development of a physics-based model for analyzing the IMD3s in the MUTC photodiode at low frequencies. Chapter 7 presents the record-low phase noise

results achieved at 10 GHz using a NIST OEO and the MUTC photodiode. The phase distortions during the photo-detection process are very important for OEOs and investigated to reveal the optimum operating conditions and the mechanisms responsible for these distortions. Chapter 8 outlines the main conclusions of the thesis and how this work can be extend in the future.

Chapter 2 High-Power MUTC Photodiode Design and Characterization

2.1 Overview

As we have discussed in Chapter 1, the MUTC photodiode structure offers high performance and great design flexibility. Our group has been working on optimization of the MUTC photodiode structure for the past several years [28, 32, 58, 59, 69-72], the most recent designs being the MUTC-4 [59] and HD-MUTC [61, 71] photodiodes. The design process involves three primary parts: the epitaxial structure, geometry, and fabrication process design. The epitaxial structure design defines the vertical layer stack of the semiconductor materials such as material composition, thickness, and impurity dopant types and concentrations. The carrier transport properties are determined by the epitaxial structure design. Simulation software such as Crosslight Apsys [73] is an excellent tool for design optimization. The crystal can then be grown in either a metal organic chemical vapor deposition (MOCVD) or molecular beam epitaxy

(MBE) reactor.

The geometry design involves defining the physical dimensions of the photodiode. Since we use a planar microfabrication process, the geometry design is concerned primarily with lateral dimensions, such as the mesa area and size of contact pads. The product of this step is a photomask set (reticle) that is used for photolithography during the fabrication process. The process flow defines the procedures used in cleanroom to fabricate the devices. Included are metal deposition, oxide growth, chemical and dry etching, deposition of anti-reflection coatings, wafer thinning, bonding to appropriate heat sinks, and electroplating. The fabrication procedures will be described in Chapter 3. We note that these three aspects of photodiode development are interrelated. For example, the dimensions of the photodiode can deviate from its design values due to lateral etching in the fabrication process. The designer needs to take all these effects into account.

Various measurement techniques are used to characterize the photodiode performance. The latter part of this chapter describes the experimental setups and techniques, with emphasis on high-power measurements.

2.2 Epitaxial structure design

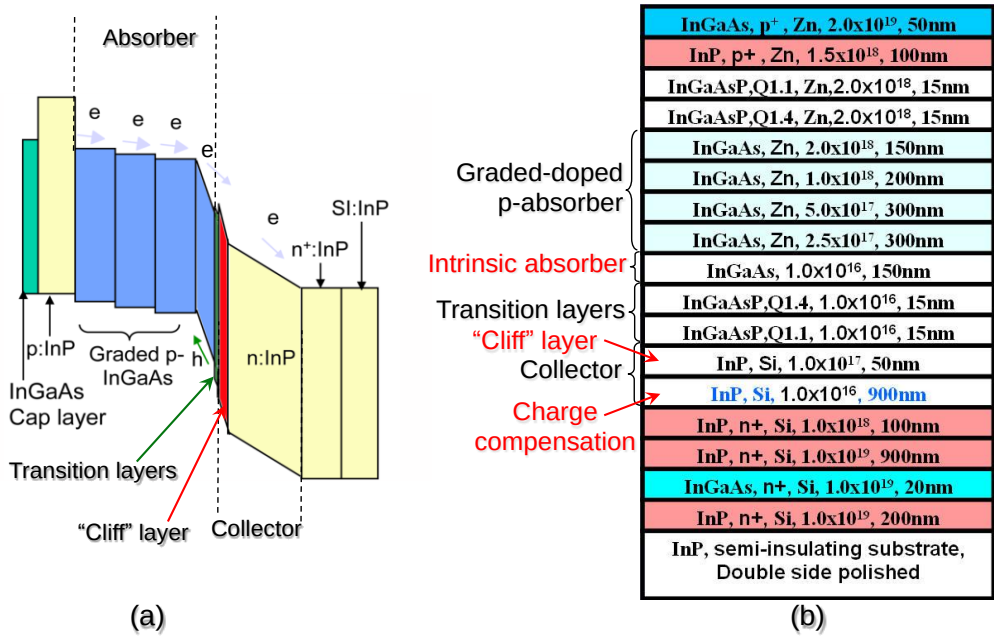

Figure 2.1 The (a) energy band diagram and (b) epitaxial structure of the MUTC-1 photodiode

The epitaxial structure and energy band diagram (under reverse bias) of the MUTC-1 photodiode are shown in Figure 2.1. The essential sections are the InGaAs absorber and the InP collector. The InGaAs absorber contains both p-type (undepleted) and unintentionally doped (UID) material. An electric field exists in the depleted region including UID InGaAs and UID InP due to the built-in potential of the junction and the applied reverse bias. Most of holes are generated in the undepleted absorber; they are quickly collected since they only need to drift a small distance toward the p-region. The electrons generated in the undepleted absorber diffuse more slowly toward the depletion region. In the depletion region

their transport is accelerated by the electric field. Consequently, the electron diffusion in the undepleted absorber is the primary bandwidth-limiting transport factor in the MUTC photodiode.

The undepleted InGaAs absorber is graded-doped. The dopant gradient establishes an electric field that accelerates electron transport. At high photocurrent densities, the potential drop across the undepleted absorber (ohmic potential) is the origin of another accelerating field for electrons, the so-called "self-induced" field. This effect reduces the carrier transit time significantly and becomes stronger with increasing photocurrent. Lower p-type doping concentrations result in larger self-induced field and less carrier recombination in the undepleted InGaAs absorber. This results in higher bandwidth and responsivity. However, there is a minimum doping concentration ($\sim 1 \times 10^{17}\ cm^{-3}$) below which the p-type absorber cannot be considered undepleted or quasi-neutral. Moreover, low doping concentrations lead to larger capacitance variation with respect to voltage, resulting in more nonlinear distortion. The highest doping level is limited by the material growth capabilities (on the order of $1 \times 10^{19}\ cm^{-3}$) and impurity diffusion. The p-type InP layer is used to block electron diffusion toward the p-contact in order to increase responsivity. The heavily doped InGaAs layer on top of the structure lowers the contact resistance.

Several design features are intended for facilitating electron transport over the InGaAs/InP heterojunction barrier between the absorber and collector, where

the conduction band discontinuity is ~ 0.24 eV. InGaAsP quaternary layers with intermediate bandgap energies are used to smooth the transition by breaking up the single large barrier into multiple smaller barriers. The depleted InGaAs layer accelerates electrons before they reach the heterojunction barrier. The "cliff" layer is a thin n-type charge layer on the InP side of the heterojunction. It boosts the electric field in the depleted InGaAs layer for better electron transport and larger saturation current. The electric field in the InP collector is reduced by the cliff layer, but it is usually acceptable since the space-charge effect there is not as severe as that in the depleted InGaAs layer.

The InP collector is lightly n-doped. The positive charges of the ionized donors compensate the negative charges of injected electrons from the absorber and mitigate the space-charge effect. More charge compensation increases saturation current, but results in larger capacitance and lower breakdown voltage.

It is worth mentioning that the MUTC photodiode structure is very similar to InGaAs/InP heterojunction bipolar transistors (HBTs). Optical injection is used in the photodiode, instead of the electrical injection by the emitter-base (EB) junction in the HBTs. Many design features mentioned above have their counterparts in HBT structures, such as the depleted InGaAs layer as "spacer" or "setback" layer, and the cliff layer as "delta-doping" or charge control layer in HBTs.

2.3 Geometry design

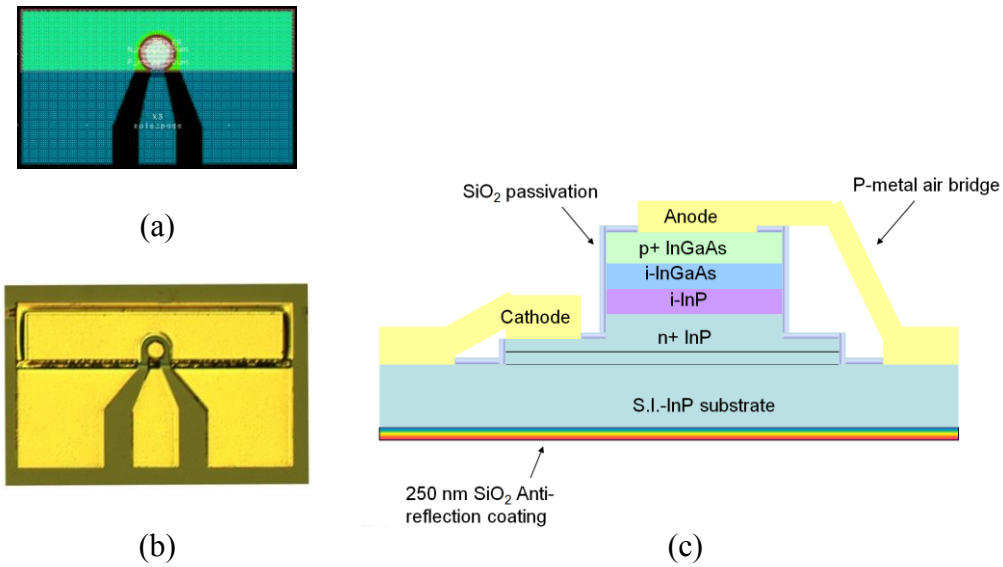

Figure 2.2 The (a) photomask design, (b) top-view microscope picture and (c) cross-section diagram (not to scale) of an MUTC photodiode. The structures in (a) and (b) measure approximately 400 µm × 200 µm.

Figure 2.2 shows the photomask design, top-view microscope picture and the cross-section diagram of an MUTC photodiode. The active area of the photodiode consists of only the small circle in the center of Figure 2.2 (a) and (b). The rest of the area is mainly occupied by the coplanar waveguide (CPW) pads used for probing and wire bonding. The photodiode uses mesa structure for isolation. The top p-mesa is connected to the center conductor of the CPW pad by an air-bridge to reduce the parasitic capacitance. The n-mesa is connected to the ground conductor directly.

2.4 Device simulation

Although analytical formulas can provide first-order estimations for some device performance metrics, numerical simulation is often needed to get more accurate results. I use the Crosslight Apsys software [73] for photodiode structure simulations. It is a semiconductor-technology computer-aided-design (TCAD) software based on 2D/3D finite element analysis. For an input structure and material set, the software solves the Poisson equation, carrier transport equations, and the current continuity equation self-consistently. The simulation output includes distributions of various physical quantities inside the device, such as the energy bands, electric field profile, carrier concentrations, and terminal (electrode) current and voltage. DC, AC and transient analysis are supported. The Crosslight APSYS software has been very useful for the present work.

2.5 Characterization techniques

2.5.1 Current-Voltage (I-V) and Capacitance-Voltage (C-V) measurements

A probe station and an HP4145B semiconductor parameter analyzer are

used for on-wafer DC current-voltage (I-V) measurements. The dark current for the MUTC photodiode is usually in the range 10 nA to 1 μA at 10 V reverse bias. A large forward current at low voltage is desirable because it implies low series resistance, which is usually around 1 ~ 5 ohms.

An HP4275A LCR meter and the same probe station are used for on-wafer capacitance-voltage (C-V) measurements. Typical device capacitance ranges from tens of femtofarad (fF) to hundreds of femtofarad.

2.5.2 RF response measurement

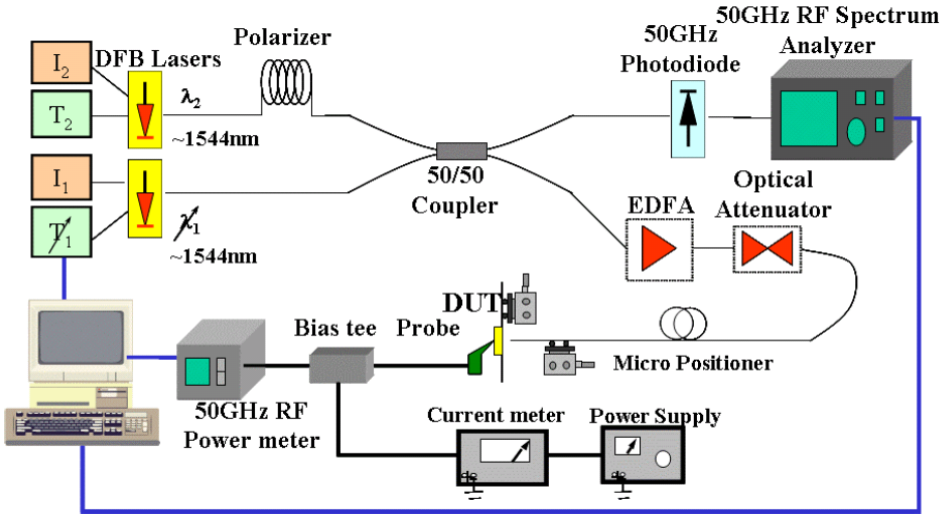

Figure 2.3 The two-laser heterodyne setup [74]

RF response measurements are carried out in both the frequency and time domains in order to obtain the 3-dB bandwidths. Comparison of the results from

these two domains can reveal more information about the physics of the photodiode. In the frequency domain, the two-laser heterodyne setup shown in Figure 2.3 is used. The outputs from two distributed-feedback (DFB) lasers with slightly different wavelengths are mixed together and the resultant beat note frequency is used as the RF source signal. Both lasers are temperature-controlled; their wavelengths are near 1544 nm at room temperature. The beat note frequency is swept by changing the temperature and thus the wavelength of one laser. For the 50GHz RF frequency range, the maximum wavelength change is ~0.4 nm. The output power of the two lasers are matched using current controllers and the modulation depth of the beating note is kept at approximately 100% across the frequency band of interest [32]. The ability to provide large-signal modulation across a wide frequency range is the primary advantage of the two-laser heterodyne setup. Saturation current is measured using the same setup. The input optical power is controlled by the attenuator while keeping the beat note frequency constant. Figure 2.4 shows the photodiode chip mounted on a thermal-electric cooler (TEC) for testing. A 50 GHz ground-signal-ground (GSG) CPW probe is used to connect to the device. The fiber is on the backside of the TEC and not visible in this picture.

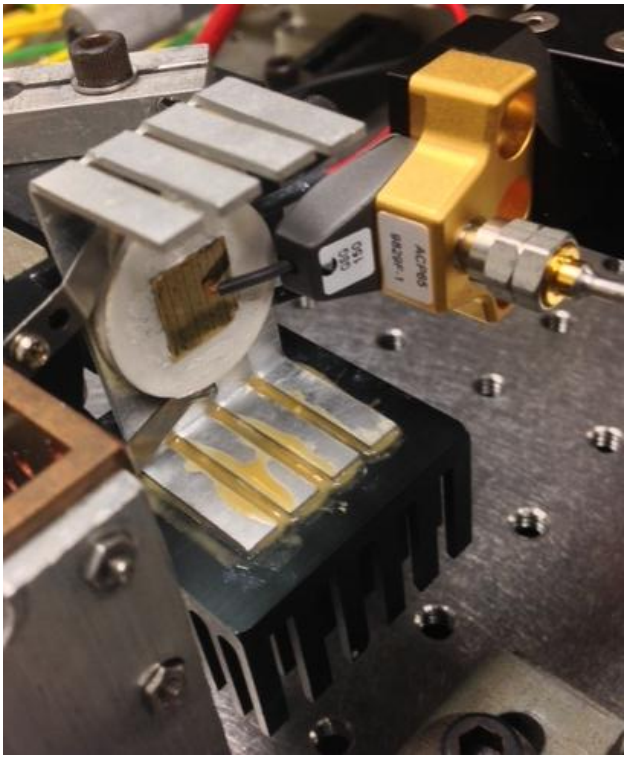

Figure 2.4 The photodiode chip mounted on the thermal-electric cooler (TEC) for testing.

Bandwidth can also be obtained from impulse response measurement by using fast Fourier transform (FFT). The light source for the impulse response measurement is a 1560 nm high-power (>100 mW average optical output) fiber laser from Toptica Photonics [75]. The pulse width is less than 100 fs and the repetition rate is 100 MHz. The relatively low repetition rate ensures that the photodiode has enough time to relax after each pulse. The electrical pulse waveform is captured by a high-speed sampling oscilloscope.

2.5.3 S-parameter measurement

S-parameter measurements are carried out using the HP8510C vector network analyzer (VNA). Both the Agilent 2.4 mm calibration kit or a CS-5 calibration substrate can be used, depending on whether on-wafer measurement is required.

2.5.4 Linearity measurement

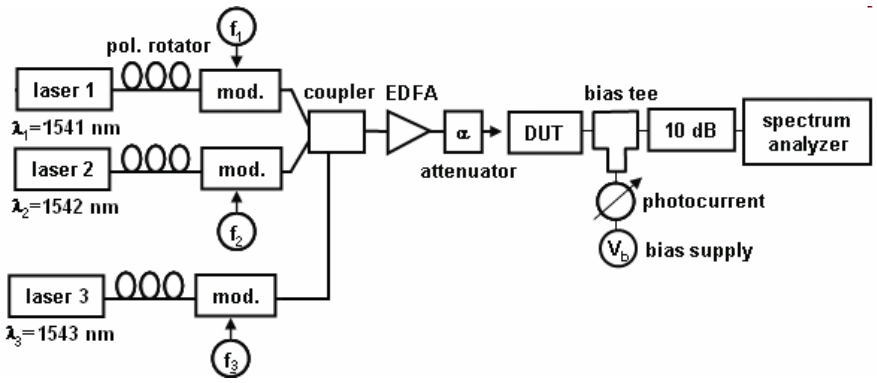

Figure 2.5 The three-tone IMD measurement setup [61]

A number of measurement techniques have been developed to characterize IMD behavior in nonlinear systems [76]. Two-tone and three-tone tests are by far the most common methods used for IMD characterization. Their results are a rich source of information about the IMD mechanisms for academic studies and serve as a good prediction for linearity performance [76, 77].

A three-tone measurement setup has been employed in this study. A

schematic diagram of the setup is shown in Figure 2.5 [61]. The three-tone method is free of the interference from second harmonics produced by the modulators [78] and less sensitive to modulator bias deviations. The three fundamental tones f_1, f_2 and f_3 are closely spaced and incommensurate. The RF power of the IMD tones located at $f_1 + f_2 - f_3$, $f_1 - f_2 + f_3$ and $-f_1 + f_2 + f_3$ are recorded using the spectrum analyzer and their average value is used for OIP3 calculation. Large attenuation (10 dB external, 30~40 dB internal) is needed in order to prevent nonlinear distortions of the spectrum analyzer from interfering with photodiode nonlinearities. The resolution bandwidth (RBW) of the spectrum analyzer is set to 100 Hz to reduce the noise floor since the magnitude of intermodulation distortions from the photodiode are very low (-80 dBm ~ -110 dBm).

Chapter 3 Photodiode Fabrication Process

This chapter describes the fabrication process for the MUTC photodiodes. Fabrication begins with the as-grown epitaxial wafer, which is usually provided by a vendor. Processing consists of four fundamental functions. A complete process flow consists of 7~9 steps, which are listed at the end of this chapter.

3.1 Metal deposition

The purposes for metal deposition include contact metallization, seed layer for electro-plating, and creation of thin film resistors. An electron beam (E-beam) evaporator is used for this process. The metal pattern is defined by photolithography. Oxygen plasma ashing (150 W, 5 min) is used before E-beam evaporation to remove any possible photoresist residues in the open windows. The small amount of photoresist lost (<100 nm) during this process is acceptable. The metal is deposited on the whole surface of the wafer in the E-beam evaporator, after which immersion in a solvent solution (e.g. acetone) removes the metal on the photoresist, leaving only the metal that adheres to the semiconductor surface

directly. This is the “lift-off” process.

For thin (<100 nm) metal deposition, positive photoresist such as AZ5214 can be used directly for pattern definition. For thicker metal layers, a double layer process is needed to ensure successful lift-off. In this process, a layer of lift-off resist (LOR) is spun onto the wafer surface before the AZ5214 photoresist. The LOR is not photo-sensitive but still can be removed by the developer solutions. With careful baking (3min at 130 °C and 2 min at 150 °C), the LOR has a slightly faster developing speed than the photo-sensitive resist on top of it. After the developing step, an undercut forms at the edge of the open patterns in the photoresist. This undercut breaks the continuous metal film and let the solvent solution remove the photoresist more easily. N-Methyl-2-pyrrolidone (NMP) and polyethylene glycol (PEG) instead of acetone are needed in order to remove the LOR. An ultra-sonic bath can be used if difficulties are encountered during the lift-off process, but the intensity should be kept as low as possible to avoid any unwanted removal of the deposited metal.

Metal stack Ti (15 nm)/Pt (20 nm)/Au (80 nm) is used for p-metallization on InGaAs, while AuGe (30 nm)/Ni (20 nm)/Au (80 nm) is used for n-metallization on InP. Ti and AuGe serve as adhesion layers in their respective stacks. Cr or Ni can also be used in this role. Usually no annealing is required for the n-metallization, but p-metallization tends to require an anneal step, which is carried out at 450 ^{o}C for 30 seconds by rapid thermal annealing (RTA) in order to

achieve low contact resistance.

3.2 Mesa etching

There are two steps that require mesa etching. First p-mesa etching defines the active area of the photodiode. It stops on the n-contact layer. Next n-mesa etching isolates different devices and removes the heavily doped n-type material where the CPW pads are located. This etch reduces leakage current and parasitic capacitance. A SiO_2 layer is deposited first on the InGaAs/InP material to act as the mask layer during etching. The pattern defined by photolithography on this mask layer is transferred to the InGaAs/InP layer with either wet chemical etching or inductively coupled plasma (ICP) etching (dry etching). The mesa height after etching is measured using the Alpha stylus profilometer.

Two types of wet etchant can be used: H_3PO_4:H_2O_2:H_2O (volume 1:1:10, etch rate 0.5~0.6 μm/min) and bromine:methanol (volume 1:200~250, etch rate 0.2~0.3 μm/min). H_3PO_4:H_2O_2:H_2O only attacks InGaAs while bromine:methanol can etch both InGaAs and InP. The etching process by bromine:methanol is diffusion limited and tends to leave trenches around the edge of the mesa, whose depth is proportional to the etching time. Although stirring the solution mitigates this problem, the material thickness etched by bromine:methanol should be kept at minimum. Consequently, the InGaAs layer is

usually removed by H_3PO_4:H_2O_2:H_2O while bromine:methanol is used for InP etching.

ICP etching is carried out using the Oxford RIE-ICP system. The recipe is Cl_2 (20 sccm):N_2 (8 sccm) gas mixture at 150 °C and 4 mTorr pressure. Dry etching attacks both InGaAs and InP with an etch rate of 500~600 nm/min. Laser-interferometry end point detection is used to monitor the etching progress. The SiO_2 mask layer is partially consumed in the dry etching process, so a relatively thick SiO_2 layer (400~500 nm) is needed to prevent etching through the mask.

Wet etching usually produces smoother sidewalls and lower leakage current, but also results in lateral undercut due to its isotropic nature. The undercut can be a serious problem for small devices (diameter < 20 μm). Dry etching is highly anisotropic and ensures an accurate pattern transfer from the mask to the InGaAs/InP layers, but tends to leave more surface damage and results in higher leakage current. In practice, a combination of dry and wet etching is used: first dry etching completes most of the etching progress and a quick wet etching (30 seconds) is used to remove the surface damage.

3.3 Oxide deposition and etching

SiO_2 is used as the etching mask, passivation layer, and anti-reflection (AR) coating in the fabrication process. It is grown in the plasma enhance

chemical vapor deposition (PECVD) system using SiH_4 (400 sccm) and NO (105 sccm) gas mixture at 285 °C. The SiO_2 film thickness is measured using the Filmetrics spectral reflectance machine on a Si dummy wafer placed close to the InP/InGaAs wafer in the PECVD chamber. The growth rate of SiO_2 is 10 ~ 12 nm/min.

Both wet and dry etching can be used for SiO_2 removal. Wet etching is done with buffered oxide etchant (BOE).; the etch rate is 120 ~ 140 nm/min. BOE etching is very stable but has similar undercut issues as the wet etchants used for mesa formation. For small features such as p-contact opening, dry etching is preferred. It is carried out in the Trion reactive ion etching (RIE) machine, using O_2 (60 sccm):CF_4 (2 sccm) gas mixture at room temperature with 300 W RIE and ICP power. The etch rate is 15 ~ 20 nm/min.

3.4 Au electro-plating

Electro-plating is used to form the contact pad and the air-bridge. It is a two-step process. First the contact pad and the pier area of the air-bridge are defined by photolithography. The photoresist in these areas is removed during the developing process, while the photoresist underneath the bridge area is kept intact in order to support the air-bridge during the electro-plating process. A long hard-bake process (120 °C, 30min) is used before the seed metal deposition. The

purpose of this hard-bake is to release all the gases in the photoresist, which tends to form bubbles beneath the seed metal layer and adversely affect the electro-plating process. A metal stack of Ti (20 nm)/Au (60 nm) is deposited as the seed layer for plating. After the metal deposition, a second photolithography is carried out directly without lifting off the first layer of photoresist and metal. The CPW pad, bridge, and bridge pier areas are all exposed after this photolithography. Oxygen plasma ashing (150W, 5 min) is used to remove any possible photoresist residue in the opening areas. The gold plating solution (from Technic Inc.) is kept in a 50 °C wafer bath during the plating process. The amount of current needed depends on the exposed gold area on the wafer. Usually 1 mA of current is used for a 1 cm × 1 cm wafer and the voltage is ~ 0.4 V. The plating rate is 0.2 ~ 0.3 μm/min. The thickness of the CPW pad and the air-bridge is 2.5 ~ 3.0 μm. The gold usually grows faster along the edges of open areas where the field lines are more crowded. After the plating is completed, the wafer is transferred to N-Methyl-2-pyrrolidone (NMP) and polyethylene glycol (PEG) for lift-off, which usually takes about 60 minutes. Both photoresist layers and the metal seed layer sandwiched in between are removed. A mild ultrasonic bath can be used to facilitate the lift-off process without damaging the air-bridges.

3.6 Additional Processing

Additional processing steps usually include wafer dicing, polishing the back of the wafer, and wire bonding. Dicing with a Disco dicing saw (from Disco High Tech America) splits the wafer into smaller pieces for testing. A layer of photoresist is spun onto the top surface of an InGaAs/InP wafer in order to protect the devices from accidental damage during the dicing process. The InGaAs/InP wafer is glued onto a silicon carrier wafer by black wax for support. The purpose of polishing is to remove any residues attached to the backside of the wafer and improve responsivity. It is done using the Logitech polishing machine. An anti-reflection coating is frequently added after polishing. Wire bonding is needed to connect the CPW pad to other substrates for testing.

3.7 Complete process flow

The complete process flow for fabricating the MUTC photodiode is listed below.

1. P-metal deposition
2. P-mesa etching
3. N-metal deposition
4. N-mesa etching

5. SiO_2 passivation
6. Contact-via opening
7. CPW pad deposition
8. CPW pad and air-bridge electro-plating
9. Wafer dicing, polishing and wire bonding (if needed)

Chapter 4 The High-Power Modified Uni-traveling Carrier (MUTC) Photodiode

4.1 Introduction

The MUTC photodiode designed by Zhi Li and others [32, 58, 59] has achieved record-high performance in terms of RF output power and linearity, and has served as the basis for further high-power photodiode development in our group. However, some interesting phenomena exhibited by the MUTC photodiode have not been understood very well, either quantitatively or qualitatively. For example, the 3-dB bandwidth of the MUTC-4 photodiode structure increases dramatically with photocurrent until saturation, as shown in Figure 4.1. This is usually attributed to electron transport acceleration by the self-induced field in the p-type InGaAs absorber [59, 79, 80]. But there is no quantitative study to relate the photocurrent-dependent bandwidth of MUTC photodiodes to their physical parameters, without which further optimization of the structure is difficult and other possible contributing mechanisms cannot be ruled out.

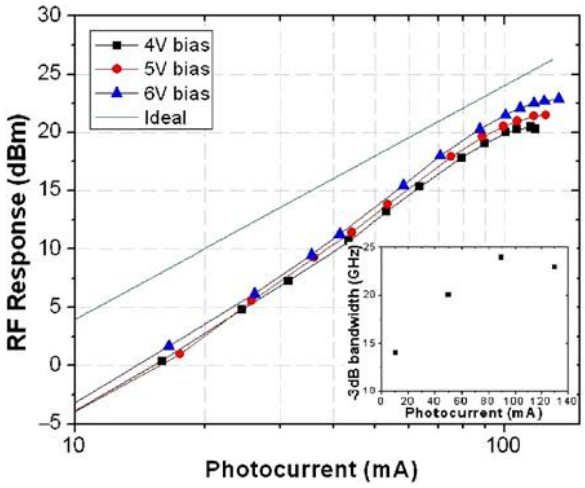

Figure 4.1 RF output power of a 34-µm-diameter MUTC-4 device at 24 GHz versus photocurrent at reverse biases of 4-V, 5-V, and 6-V. The inset shows the −3 dB bandwidth for different photocurrent values (10, 50, 90, and 130 mA). [59]

The impedance of the MUTC photodiode also varies with changing photocurrent. One example of S11 measurement on a MUTC-4 photodiode is shown in Figure 4.2. Most interestingly, the magnitude of S11 becomes larger than unity at high photocurrent levels, which implies the existence of negative differential resistance (NDR). It should not be surprising to find NDR in the MUTC photodiode, which contains many possible contributing elements, such as the negative differential electron mobility of InGaAs and InP, electron injection delay from absorber to the drift layer (similar to Gunn and IMPATT devices) and the heterojunction barrier. The existence of NDR in MUTC photodiodes could have important implications on the device operating principles, as well as the epitaxial structure and matching circuit design.

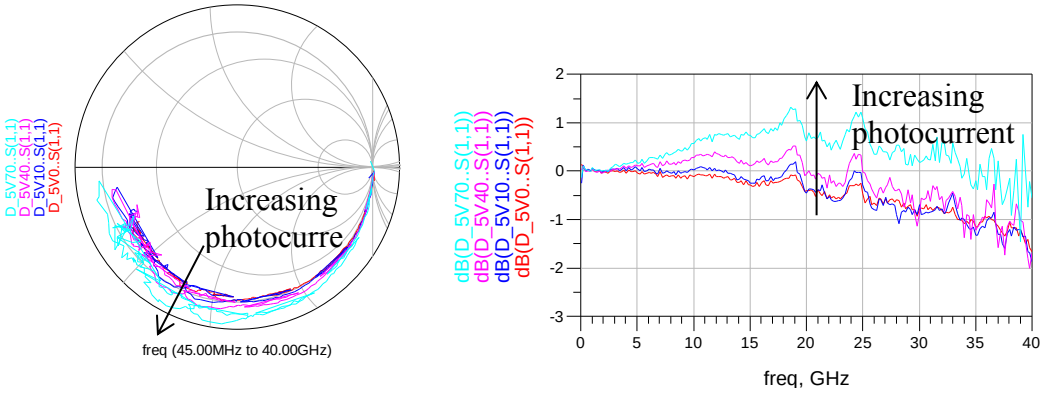

Figure 4.2 (a) S11 and (b) its magnitude of a 40 µm MUTC-4 photodiode bias at -5V. The photocurrent is increased from 0 mA to 70 mA

It is therefore the purpose of this chapter to provide a detailed study of both the bandwidth and the impedance characteristics of the MUTC photodiode. Results obtained from different measurement techniques are compared, and a physics model of the photodiode is established using the commercial software package Crosslight Apsys [73]. The model is also used to study the origin of the NDR.

4.2 The MUTC-4 photodiode

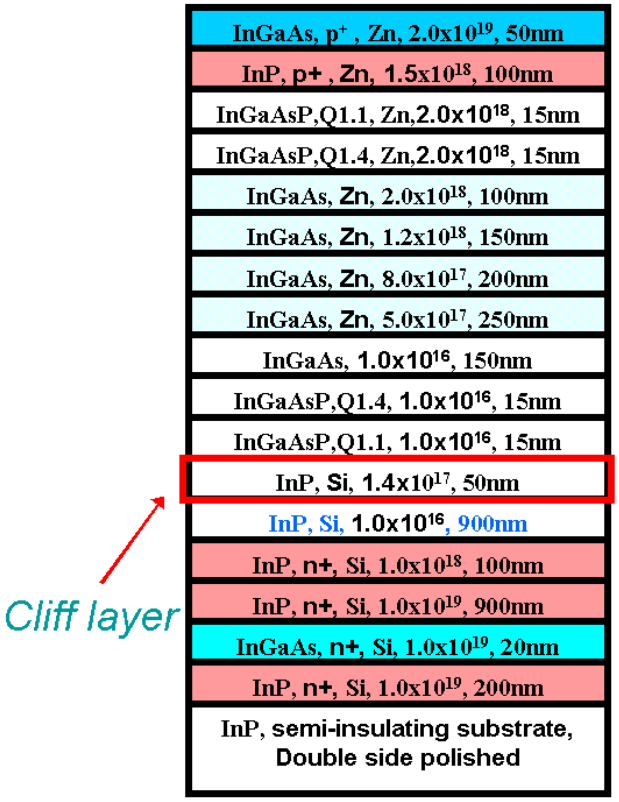

Figure 4.3 The epitaxial structure of the MUTC-4 photodiode [59]

The epitaxial structure of the MUTC-4 photodiode is shown in Figure 4.3. It is a PIN diode, or more specifically, $p^+n^-n^+$structure. The majority of the potential drop exists in the n^- layers when the diode is reverse-biased. The total InGaAs absorber thickness is 850 nm, of which 700 nm is p-type with Zn doping. The 150nm UID InGaAs layer is intended to provide sufficient electric field for electrons generated in the absorber to overcome the heterojunction barrier at InGaAs/InP interface. The electric field is further enhanced by the thin charge

layer or “cliff” layer of 50nm n-type InP. The incorporation of the InGaAsP quaternary layer reduces the conduction band spike between InGaAs and InP. The drift layer, which is also referred to as the collector, is 900 nm-thick n-type InP. The purpose of the light Si doping in this layer is to compensate the charge of injected electrons at high photocurrent levels and avoid early saturation.

MUTC-4 photodiodes with different diameters are studied in this chapter, including 20μm, 28μm, 40μm and 56μm. Comparing the performance of photodiodes with different active area is a very useful in many aspects. For example, the smaller devices with less RC delay is good for studying transit-time related effect and they can usually withstand higher current density; on the other hand, larger devices provides less uncertainty for extracting area-related parameters and can reach larger current, which comes in handy when investigating current-related effect such as load feedback. Analysis accuracy can also be improved by employing statistical techniques like linear regression. The responsivity is 0.7 A/W at -5V bias voltage and 1550 nm wavelength.

4.2.1 Impedance analysis

Both capacitance-voltage (C-V) and one-port S-parameter measurements are used to extract the impedance parameters of the MUTC-4 photodiodes. The C-V curves are measured in the dark, while the S-parameters are obtained under

both dark and illuminated conditions.

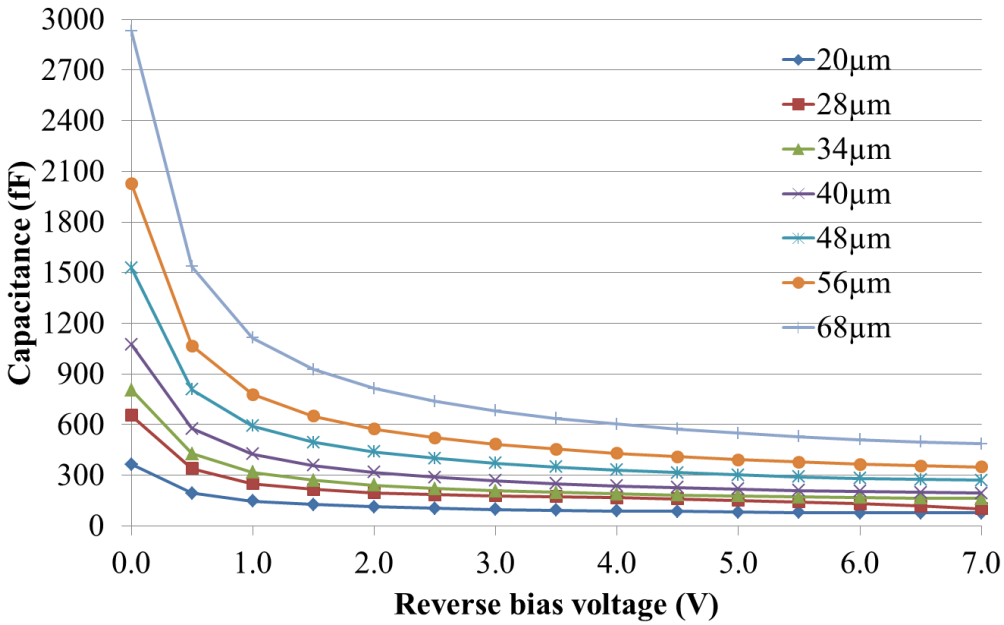

Figure 4.4 The capacitance-voltage characteristics of MUTC-4 photodiode

The C-V curves of MUTC-4 photodiodes with diameters in the range 20 µm to 68 µm are shown in Figure 4.4. The depletion width increases with increasing reverse bias voltage, thus reducing the capacitance. The C-V curve is almost flat after the drift layer is completely depleted. This is referred to as "punch-through". Usually the measured capacitance contains contributions from the CPW pad and other sources. So the intrinsic capacitance of the photodiode is extracted using the linear regression technique, as shown in Figure 4.5. The intercept of the linear regression line is subtracted from the measured capacitance to reveal its intrinsic value.

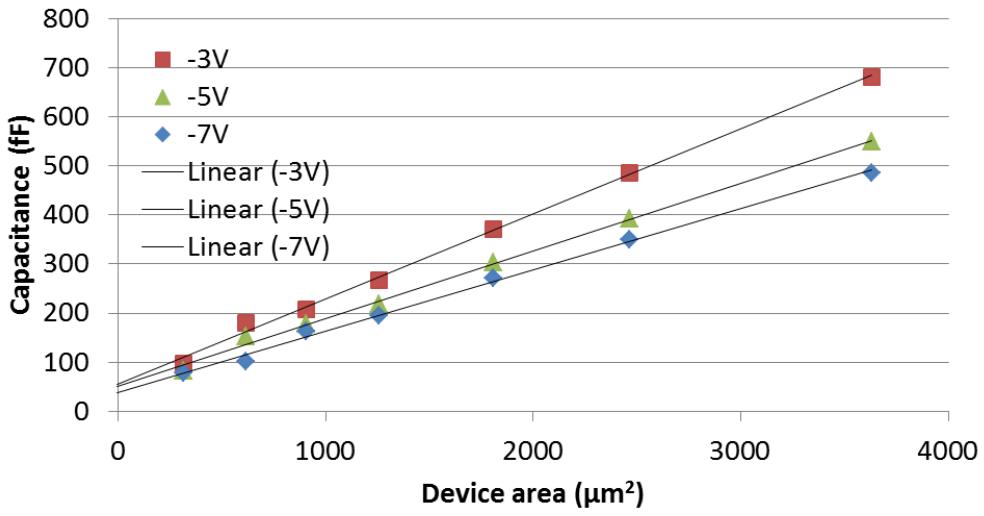

Figure 4.5 Linear regression analysis of the photodiode capacitance

The impedance of the photodiode may deviate from its dark value when it is illuminated. A 1-port S-parameter measurement is used to characterize this change. The S-parameter is measured from 45 MHz to 40 GHz using an HP8510C vector network analyzer (VNA). A CS-5 calibration substrate from GGB Industries is used for on-wafer calibration with the short-open-load-through (SOLT) method. The reference plane is at the CPW probe (Cascade 50A-GSG-150) tip after calibration. Bias voltage is supplied through an HP 50 GHz bias tee. The light source is a 1550 nm DFB laser without modulation. One measurement example is shown in Figure 4.6.

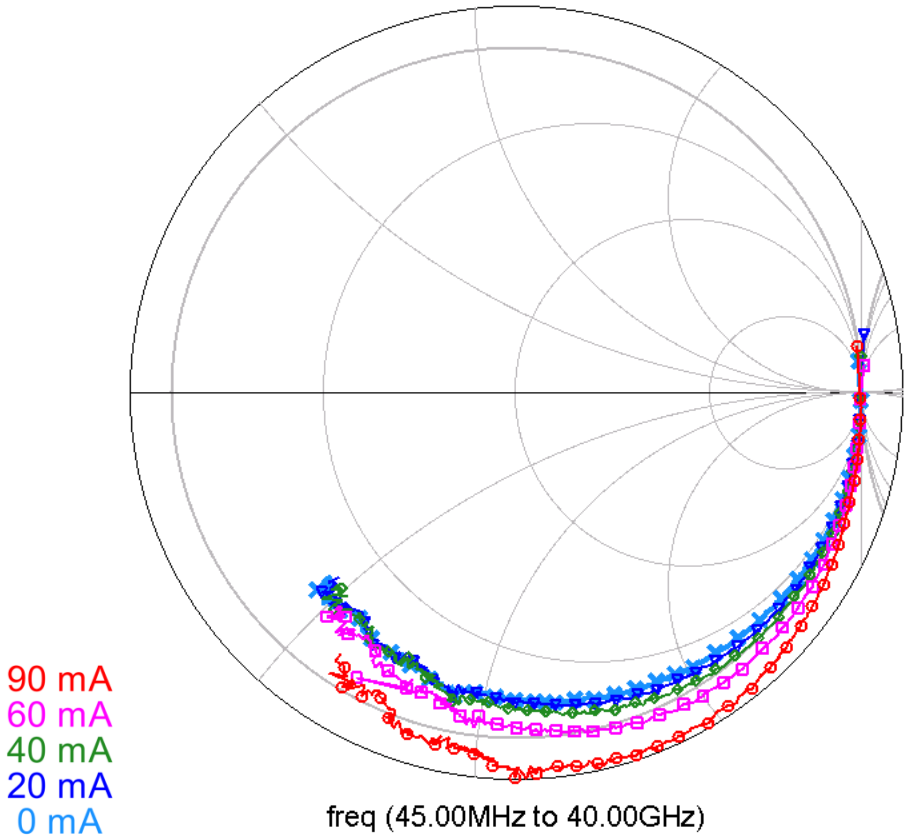

Figure 4.6 S11 of a28 µm-diameter MUTC-4 photodiode at -5V bias voltage and different photocurrent

The S11 curves resemble that of an open-end transmission line for dark and low photocurrent levels. This is due to the fact that the photodiode acts as a capacitor connected at the open-end of CPW pad, which can be regarded as a short transmission line. Ideally the CPW pad should be de-embedded by incorporating the calibration standards on the same wafer as the photodiode so that the reference plane can be moved onto the photodiode itself. But those calibration standards would either take up valuable real estate on wafer (for TRL

method) or be hard to implement accurately (for SOLT method). Fortunately the extent of distortion to resistance of the photodiode is negligible since the CPW pad is short (~100 μm). Although its effect on the photodiode reactance is quite large, I am concerned primarily with the relative change in the photodiode reactance in this measurement, rather than its absolute value. The CPW pad impedance is independent of photocurrent or bias voltage, and thus can be removed from the measurement results.

As the photocurrent increases in Figure 4.6, S11 of the photodiode moves radially outward on the Smith chart, and eventually exceeds the circle where the magnitude equals unity. This implies the presence of negative differential resistance (NDR). In order to see the impedance change more clearly, the measurement result can be plotted in the form of resistance and capacitance by converting the S-parameters into Z-parameters. Device parameters extracted from Figure 4.6 are plotted in Figure 4.7.

It is clear that both resistance and capacitance drop noticeably as the photocurrent increases. The capacitance change can be explained as follows: at high photocurrent levels, the photo-generated carriers screen the space-charge field generated by the background dopants. The net charge concentration becomes smaller so that a larger depletion width is required to satisfy the Poisson equation [81]. This phenomenon is especially pronounced in photodiode structures utilizing a charge-compensated drift layer, which does not achieve punch-through at

moderate bias voltage and small photocurrent. The frequency dependent behavior of the capacitance is the result of the CPW pad, as explained above.

The dark condition resistance is usually modeled as the series resistance of the photodiode, comprising contact and bulk resistances. At larger photocurrent, the resistance becomes smaller or even negative. This is very interesting and the focus of this study.

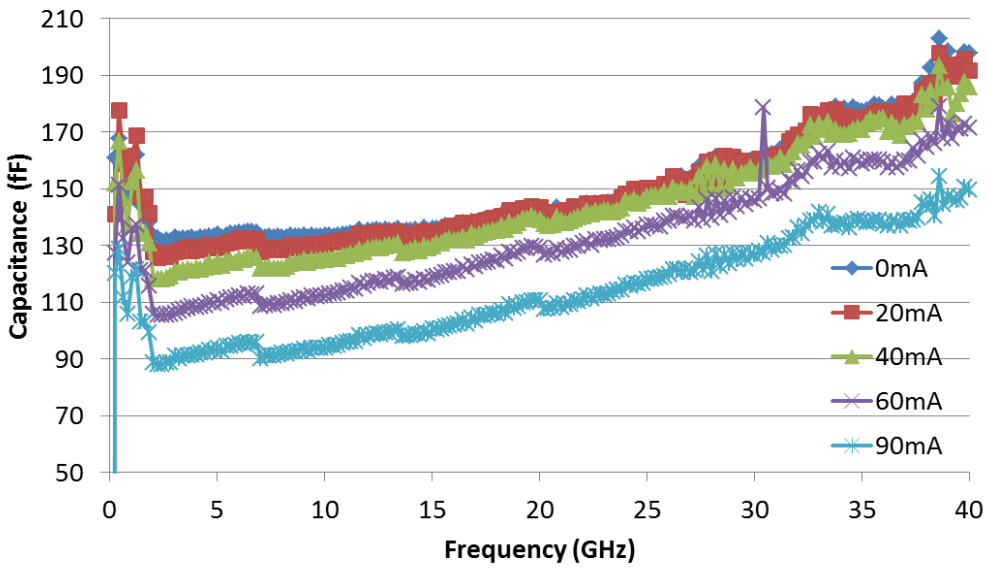

(a)

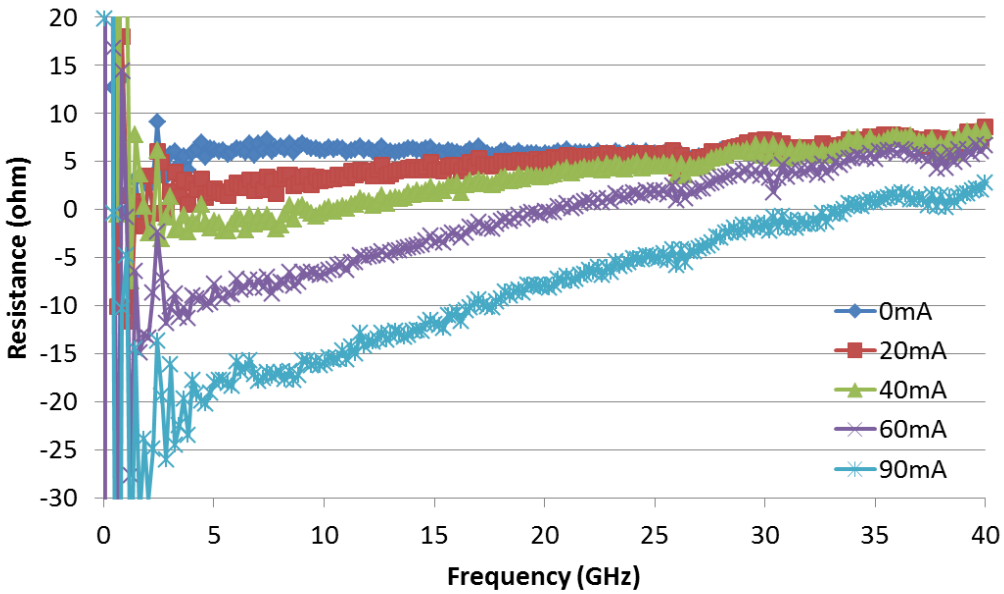

(b)

Figure 4.7 The (a) resistance and (b) capacitance of a 28 µm-diameter MUTC-4 photodiode at -5 V from S-parameter measurements

The net effect of decreasing resistance and capacitance of the photodiode is reduced RC time delay or larger RC-limited bandwidth. Overlooking this effect in device modeling could result in an over-estimate of the transit-time limited bandwidth of the photodiode.

20 µm				28 µm			
I (mA)	R (ohm)	C (fF)	RC limited BW (GHz)	I (mA)	R (ohm)	C (fF)	RC limited BW (GHz)
0	12	52	49.4	0	6	100	28.4
10	10	45	58.9	10	5	100	28.9
20	7	40	69.8	20	5	90	32.2
30	3	35	85.8	30	4	85	34.7
40	-6	33	109.6	40	-1	80	40.6
50	-10	33	120.6	60	-7	72	51.4
60	-15	32	142.1	90	-10	65	61.2
40 µm				56 µm			
I (mA)	R (ohm)	C (fF)	RC limited BW (GHz)	I (mA)	R (ohm)	C (fF)	RC limited BW (GHz)
0	4	192	15.4	0	2.6	368	8.2
20	4	182	16.2	40	2.6	350	8.6
40	4	179	16.5	50	2.4	350	8.7
60	2	170	18.0	70	2.4	350	8.7
90	0	165	19.3	105	2	335	9.1
140	-3	146	23.2	150	2	323	9.5

Table 4.1 Summary of MUTC-4 photodiode impedance at -5V

The impedance of MUTC-4 photodiodes at -5V is summarized in **Table 4.1**. These data will be used in conjunction with bandwidth results to extract the carrier transit time and other parameters. The depletion width estimated using the capacitance data is shown in Figure 4.8. We can see that in the dark the collector

is not punched through; the depletion width is only 700~800 nm. The maximum depletion width of ~1100 nm agrees well with the epitaxial design.

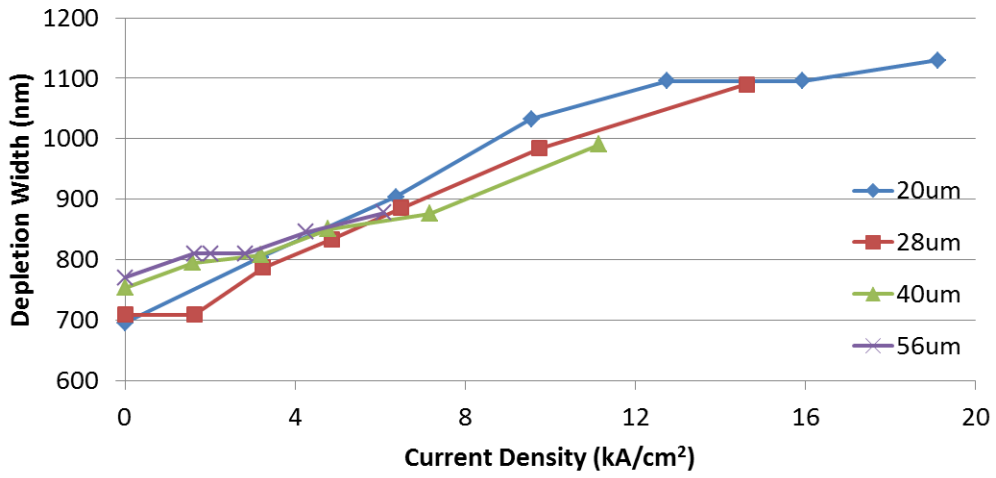

Figure 4.8 Depletion width of MUTC-4 photodiodes at -5V estimated from capacitance data

Figure 4.9 shows the normalized resistance with respect to current density. The data points spread over a larger range, comparing to that in Figure 4.8, but the decreasing trend is clear.

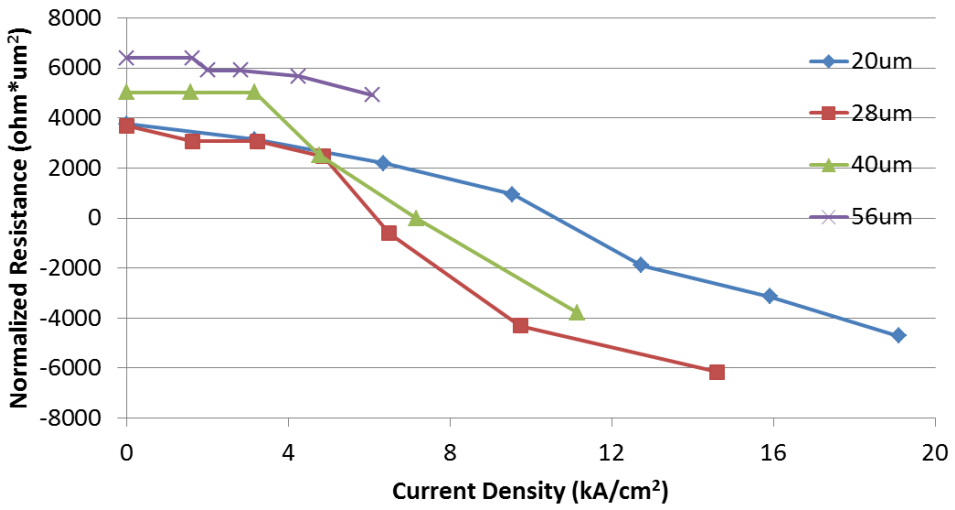

Figure 4.9 Normalized resistance of MUTC-4 photodiode at -5V

4.2.2 Bandwidth measurement and discussion

The bandwidth of the MUTC-4 photodiode was measured using small-signal impulse response and the two-laser heterodyne methods described in Chapter 2. The two-laser heterodyne method can generate a sinusoidal signal with almost 100% modulation depth over a large frequency range (>100GHz), and thus has become the standard approach for measuring the bandwidth of high-power photodiodes [6, 58, 82]. The majority of the MUTC-4 photodiode bandwidth data were obtained using this technique. However, the simultaneous presence of a large DC current offset (average photocurrent) and an RF tone during the test makes it difficult to distinguish their individual contributions to device performance. Consequently, it is beneficial to use different test methods with

separate control of average photocurrent and RF signal. The small signal impulse response method has very small RF component (or modulation depth) so that the effect of DC current offset can be separated. This approach also avoids possible early saturation caused by the large peak current/voltage during the two-laser heterodyne measurement. It is also a much faster measurement; it is almost instantaneous compared to 3~5 min for the heterodyne technique). A third method of large-signal impulse response is the other extreme (very large modulation depth), which will be investigated in Chapter 7.

The impulse response measurement setup has been described in Chapter 2. The pulse amplitude is kept constant during the measurement to observe only the effect of changing DC offset current. The impulse response waveforms are captured using a 50 GHz Agilent 86100C Infiniium DCA. 12dB of RF attenuation is used to minimize reflections. An example of small-signal impulse response is shown in Figure 4.10.

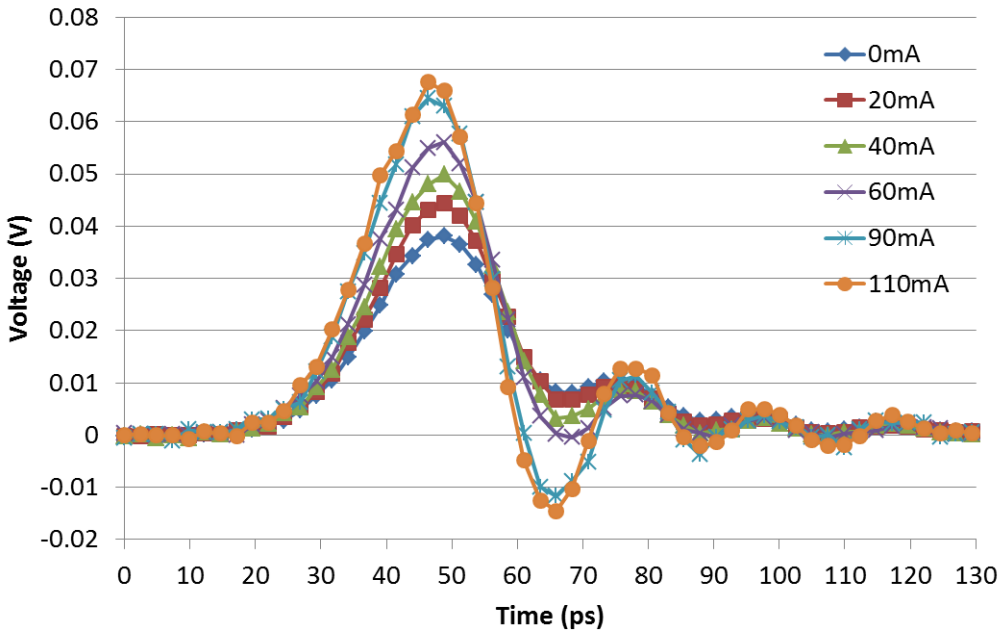

Figure 4.10 Impulse response of 28 µm-diameter MUTC-4 photodiode at -5V. These waveforms do not include calibration for the cable assembly.

Several observations can be made from Figure 4.10. First, the pulse peak amplitude becomes larger with increasing DC photocurrent, while the area below the curve remains constant. This is consistent with the photodiode being faster with increasing DC photocurrent, rather than a responsivity change. Secondly the larger oscillation or "ringing" at higher DC photocurrent suggests the presence of peaking in the frequency response. The relatively small change in pulse width or FWHM could be the result of cable assembly insertion loss.

The 3dB bandwidth of MUTC-4 photodiodes is summarized in Table 4.2. The small-signal impulse response bandwidth is calculated using Fast Fourier Transform (FFT). The transit-time limited bandwidth is computed from the

following equation,

$$\frac{1}{f_{3dB}^2} = \frac{1}{f_{RC}^2} + \frac{1}{f_{transit}^2} \tag{4.1}$$

and will be used to compare with Crosslight Apsys model results in the next section.

20 μm				
DC offset current (mA)	RC limited BW (GHz)	Small-signal impulse response BW (GHz)	Two-laser heterodyne BW (GHz)	Calculated transit-time limited BW (GHz)
0	49.4	9	10	9.2
10	58.9	12	14	12.3
20	69.8	15	14	15.4
30	85.8	18	18	18.4
40	109.6	22	24	22.5
50	120.6	30	30	31.0
60	142.1	36	31	37.2
28 μm				
DC offset current (mA)	RC limited BW	Small-signal impulse response BW	Two-laser heterodyne BW (GHz)	Calculated transit-time limited BW

	(GHz)	(GHz)		(GHz)
0	28.4	9	10	9.5
10	28.9	10	10.5	10.7
20	32.2	11	12	11.7
30	34.7	12	13	12.8
40	40.6	15	17	16.1
60	51.4	17	19	18.0
90	61.2	24	24.5	26.1
40 μm				
DC offset current (mA)	RC limited BW (GHz)	Small-signal impulse response BW (GHz)	Two-laser heterodyne BW (GHz)	Calculated transit-time limited BW (GHz)
0	15.4	8	9	9.4
20	16.2	9	9	10.8
40	16.5	10	11	12.6
60	18.0	11	11	13.9
90	19.3	12	13	15.3
140	23.2	15	15	19.7
56 μm				

DC offset current (mA)	RC limited BW (GHz)	Small-signal impulse response BW (GHz)	Two-laser heterodyne BW (GHz)	Calculated transit-time limited BW (GHz)
0	8.2	6	7	8.8
40	8.6	7	7	11.9
50	8.7	6.5	7	9.8
70	8.7	7	8	11.8
105	9.1	7	8	11.0
150.0	9.5	8	8	14.9

Table 4.2 Bandwidth summary of MUTC-4 photodiode at -5V

The bandwidth data can be better visualized when plotted versus current density, as in Figure 4.11. First we can see that the results from small-signal impulse response and two-laser heterodyne methods agree reasonably well. This is strong indication that the bandwidth increasing trend with photocurrent is caused by the current offset or bias, instead of the RF component. In other words, the MUTC-4 photodiode's bandwidth is almost independent of signal modulation depth (from ~0% to 100%). It is a desirable feature for many applications. We revisit the bandwidth analysis in Chapter 7 for the very large modulation depth case.

The bandwidths of smaller devices (20 μm and 28 μm diameters) are

primarily limited by carrier transit-time up to the highest photocurrent density measured. The RC delay starts to affect bandwidth noticeably for the 40 µm-diameter device. For the largest device (56 µm) the RC delay dominates the speed performance.

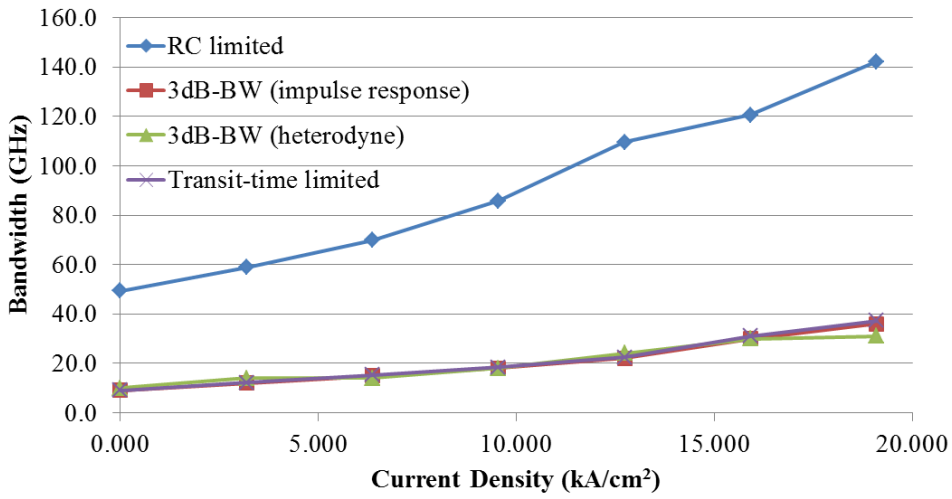

(a) 20µm MUTC-4 photodiode at -5V

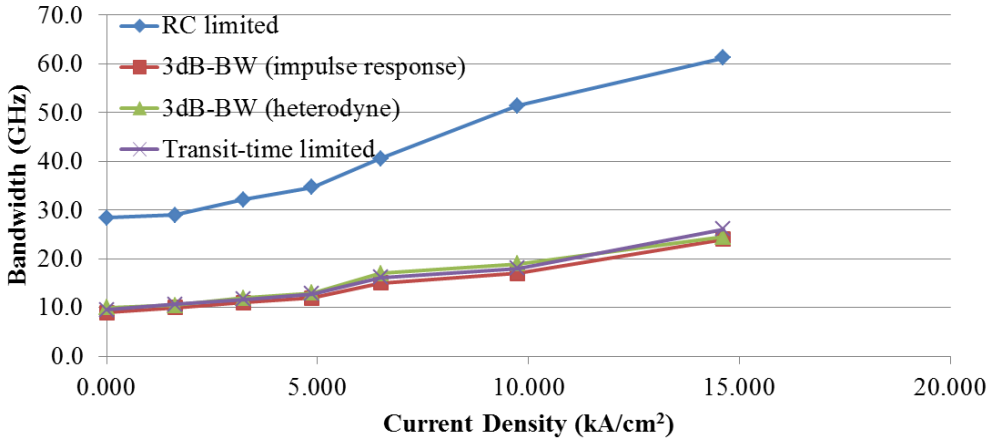

(b) 28µm MUTC-4 photodiode at -5V

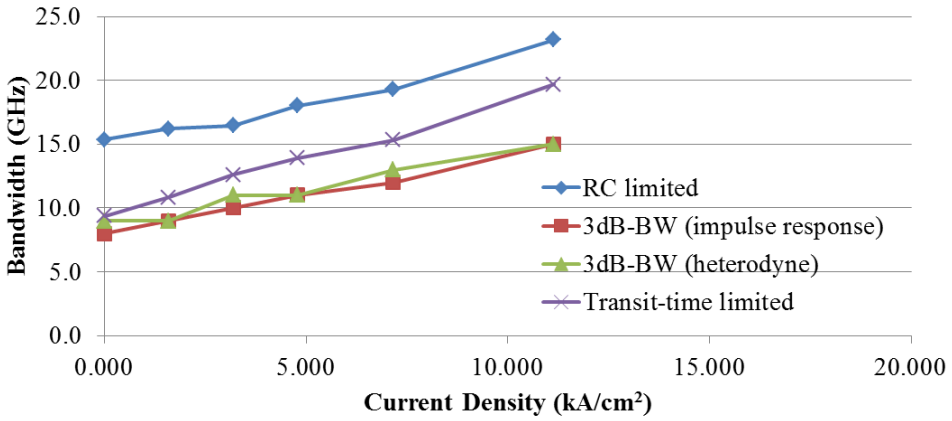

(c) 40µm MUTC-4 photodiode at -5V

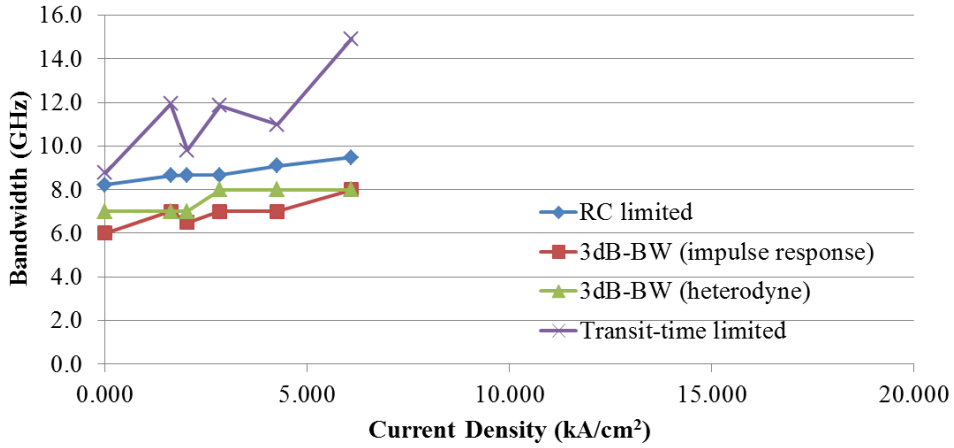

(d) 56µm MUTC-4 photodiode at -5V

Figure 4.11 Bandwidth summary for MUTC-4 photodiodes with different diameters at -5V

Both RC and transit-time limited bandwidth increase with higher photocurrent. It has previously been assumed that only the transit-time changes significantly with increasing photocurrent [32, 58, 59]. The results presented here provide a more accurate picture for modeling the carrier dynamics inside the MUTC-4 photodiode. Figure 4.12 compares the extracted carrier transit time for

devices with different diameters. The good agreement among different curves implies that the effect scales with device area, an indication of bulk related phenomenon and the absence of perimeter/surface related parasitics.

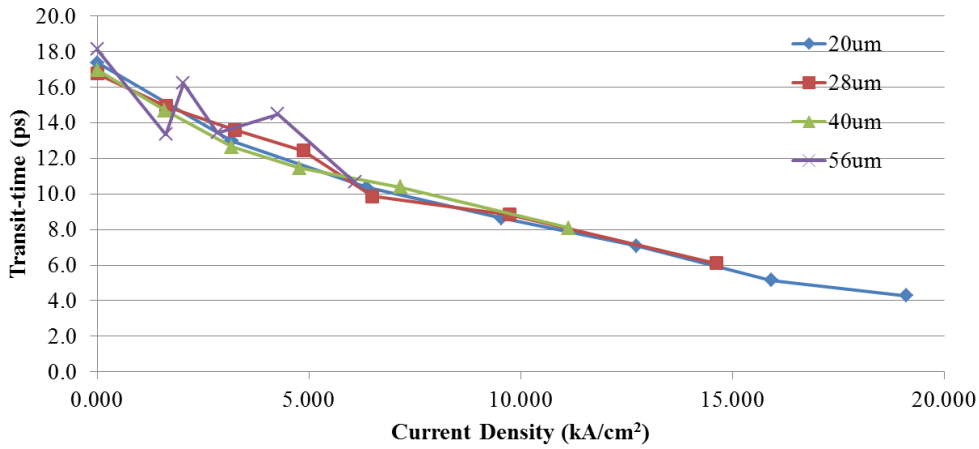

Figure 4.12 Carrier transit time's dependence on current density for MUTC-4 photodiode at -5V

When the photocurrent is very small, the transit time is dominated by electron diffusion in the p-type InGaAs absorber, which can be calculated using [83],

$$\tau_A = \frac{W_A^2}{\eta D_e^2}. \tag{4.2}$$

Here W_A= 700 nm is the width of undepleted absorber, D_e is the electron diffusion constant in p-type InGaAs, and $\eta = 2$ for a uniformly doped absorber. For non-uniform doping, as in the MUTC-4 design with dopant grading, the factor η can be estimated by [83],

$$\boldsymbol{\eta = 2\left[1 + \left(\frac{E_{bi}}{E_0}\right)^{3/2}\right]} \tag{4.3}$$

where $E_0 = \frac{2kT}{qW_A}$, and E_{bi} is the built-in field due to graded doping. For the MUTC-4 design, we have

$$\boldsymbol{E_{bi} = \frac{kT}{qW_A}\ln\left(\frac{N_A^{max}}{N_A^{min}}\right) = 1.39\frac{kT}{qW_A}} \tag{4.4}$$

Substituting (4.4) into (4.3), we have $\eta = 3.2$. The electron diffusion constant D_e ranges from 60 cm^2/s to 260 cm^2/s in the literature [84-86]. Here we take 130 cm^2/s [85], In (4.2) this yields $\tau_A = 11.8$ ps. The collector transit time is represented as [83],

$$\boldsymbol{\tau_C = \frac{W_C}{2V_e}} \tag{4.5}$$

where W_C is the depletion width and V_e is the average electron drift velocity in InP. The electron overshoot velocity in InP is ~2.5×10^7cm/s and the saturation velocity is ~1.0×10^7cm/s [87, 88]. V_e can be approximated as 1.75×10^7cm/s and $\tau_C = 2.0$ ps. The total transit time at small photocurrent is then

$$\boldsymbol{\tau_{transit} = \tau_A + \tau_C = 13.8\,ps} \tag{4.6}$$

As the photocurrent increases, the induced field in the p-type InGaAs due to hole current becomes stronger and reduces the electron transit time. The average induced field can be calculated as [89], (assuming uniform carrier generation)

$$\boldsymbol{E_{ind} = \frac{J_h}{q p_{avg} \mu_p}} \tag{4.7}$$

where J_h is the average hole current density, q is the electron charge, p_{avg} is the average hole concentration and $\mu_p = 150 cm^2/Vs$ [72] is the hole mobility. In Figure 4.12, for the largest current density $J_0 = 19\ kA/cm^2$ and $J_h \approx \frac{J_0}{2} = 9.5\ kA/cm^2$. p_{avg} can still be approximated as quasi-neutral condition in which $p_{avg} = Na_{avg} = 0.95 \times 10^{18} cm^{-3}$. Then the induced field is $E_{ind} = 0.42\ kV/cm$. Combining this with the build-in field of (4.4) we have = 10.1 . Substituting into (4.2) yields,

$$\boldsymbol{\tau_A = 4.8\ ps\ .} \tag{4.8}$$

The collector transit time τ_C may increase slightly due to deeper penetration of the depletion region, which would reduce τ_C to 3.1 ps . The total transit time at $J_0 = 19\ kA/cm^2$ is,

$$\boldsymbol{\tau_{transit} = \tau_A + \tau_C = 7.9\ ps\ .} \tag{4.9}$$

These two simple estimates fit the data in Figure 4.12 reasonably well. The overestimation of the transit time at high photocurrent may be caused by several factors. In reality, the electric field in a large portion of the depletion region could assume values close to overshoot field strength. This would reduce the collector transit time significantly. The induced field in the undepleted

absorber could be higher thus resulting a shorter absorber transit time. The carriers generated in the depleted InGaAs absorber, which we ignored in the analysis above, also tend to increase the device speed.

4.2.3 Modeling MUTC-4 photodiode in Crosslight Apsys

I have established a 2-D numerical model for the MUTC-4 photodiode structure in Crosslight Apsys software in order to better understand its characteristics. The working principle and simulation process of Crosslight Apsys are described in Chapter 2. The device is simulated under short-circuit condition, which means that the RC delay is not considered. Parameter scans are carried out for different illumination intensities at constant bias voltage. The model files and material parameters used in the simulation can be found in Appendix I Parameters for Crosslight Apsys Simulation

Figure 4.13 (a)-(c) summarize the spatial profile of the conduction band energy, the electric field, and the electron velocity inside an MUTC-4 photodiode at different photocurrent densities. We can see that the edge of depletion region reaches the n contact layer at photocurrents above 9.6 kA/cm^2, which agrees with the measurement data in Figure 4.8. The electric field in the right-half of the depletion region drops quickly with increasing photocurrent as a result of elevated

electron concentration or “electron accumulation”, which causes current saturation and limits the RF output power. The electric field in the depleted InGaAs absorber falls more quickly than that in the InP collector due to the blocking effect of the heterojunction interface. The insertion of a cliff layer boosts the field strength in depleted InGaAs at the expense of that in InP collector to prevent early saturation. We note that electrons travel at the overshoot velocity over a significant portion of the InP collector, which could potentially give rise to negative differential resistance.

The conduction band in the undepleted absorber bends more and more with increasing photocurrent and results in the self-induced field discussed above. This field transitions the electron transport in the undepleted InGaAs region from diffusion to mixed drift and diffusion, which is much faster. The electron speed reaches 10^7cm/s, which is consistent with calculations in [85, 89]. The transit-time has been calculated using the small-signal AC analysis function of Crosslight Apsys. The results are plotted in Figure 4.14 together with measurement data. The agreement between measurement and simulation is good.

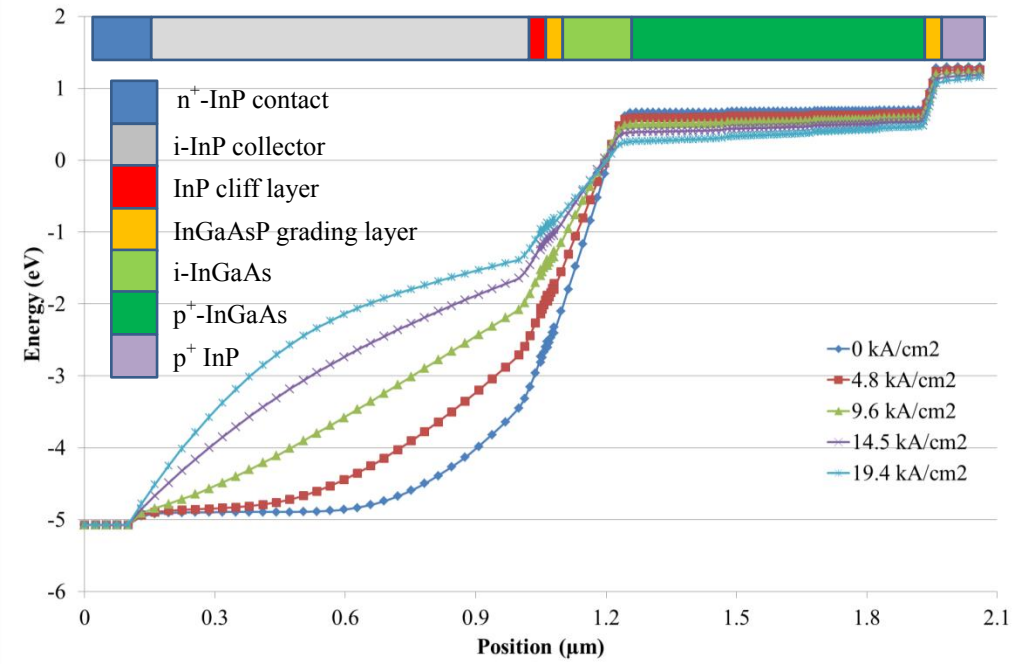
n+-InP contact
i-InP collector
InP cliff layer
InGaAsP grading layer
i-InGaAs
p+-InGaAs
p+ InP
0 kA/cm2
4.8 kA/cm2
9.6 kA/cm2
14.5 kA/cm2
19.4 kA/cm2
Energy (eV)
Position (µm)

(a)

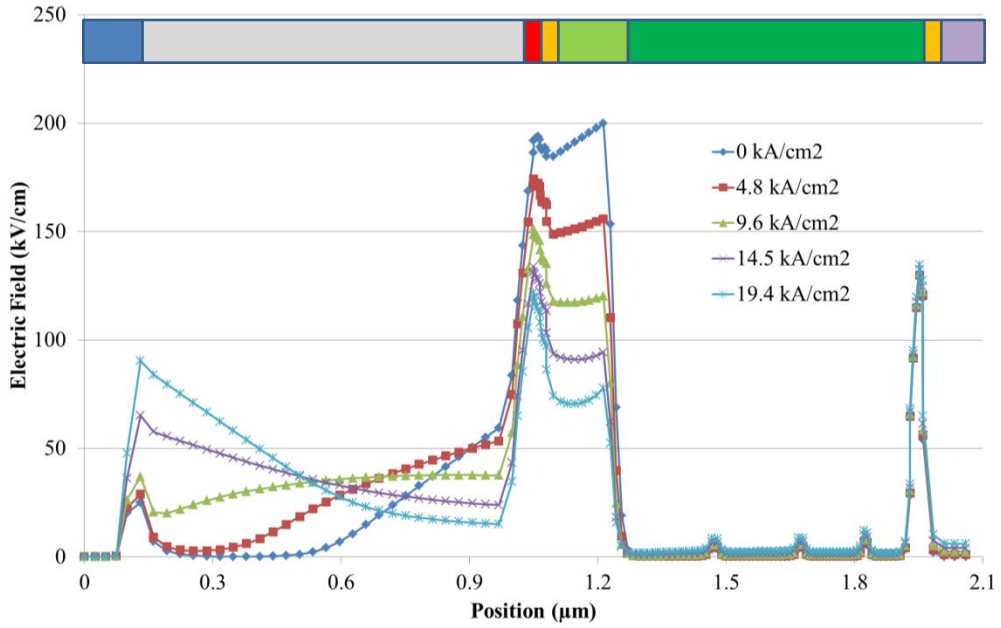
0 kA/cm2
4.8 kA/cm2
9.6 kA/cm2
14.5 kA/cm2
19.4 kA/cm2
Electric Field (kV/cm)
Position (µm)

(b)

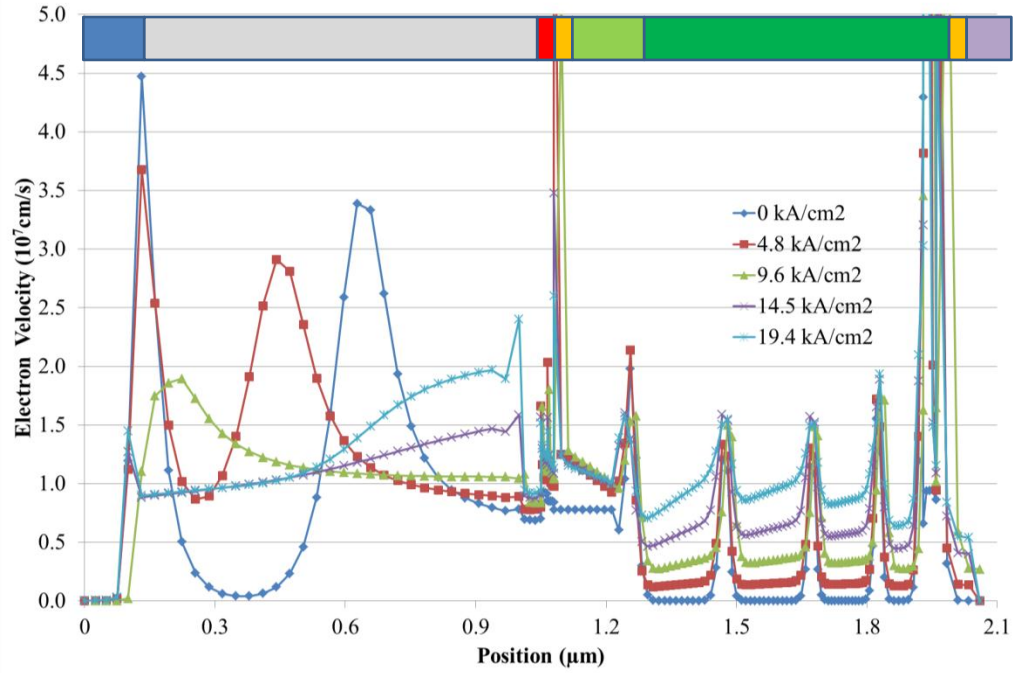

(c)

Figure 4.13 The simulated (a) conduction band, (b) electric field and (c) electron velocity profiles of an MUTC-4 photodiode at different photocurrent and -5V bias voltage.

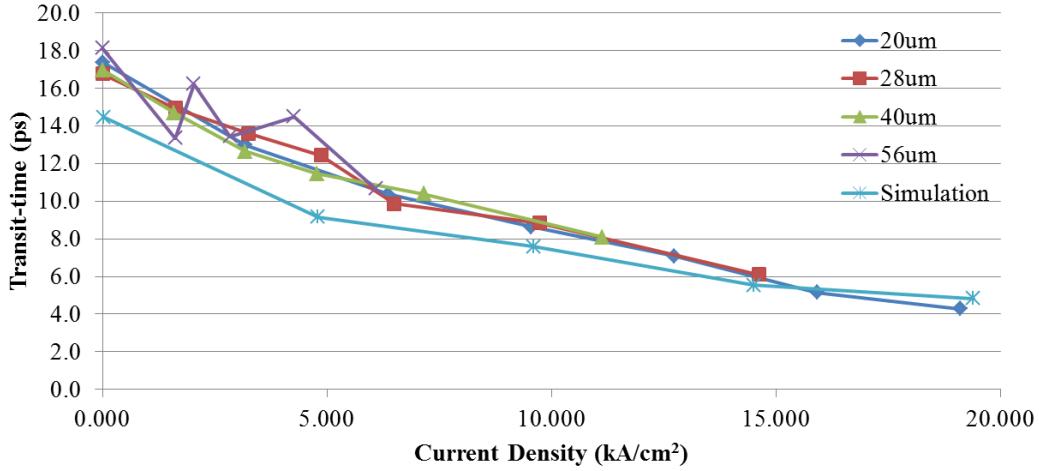

Figure 4.14 Comparison of measured and simulated transit-time of MUTC-4 photodiode at -5V

4.2.4 The origin of negative differential resistance (NDR)

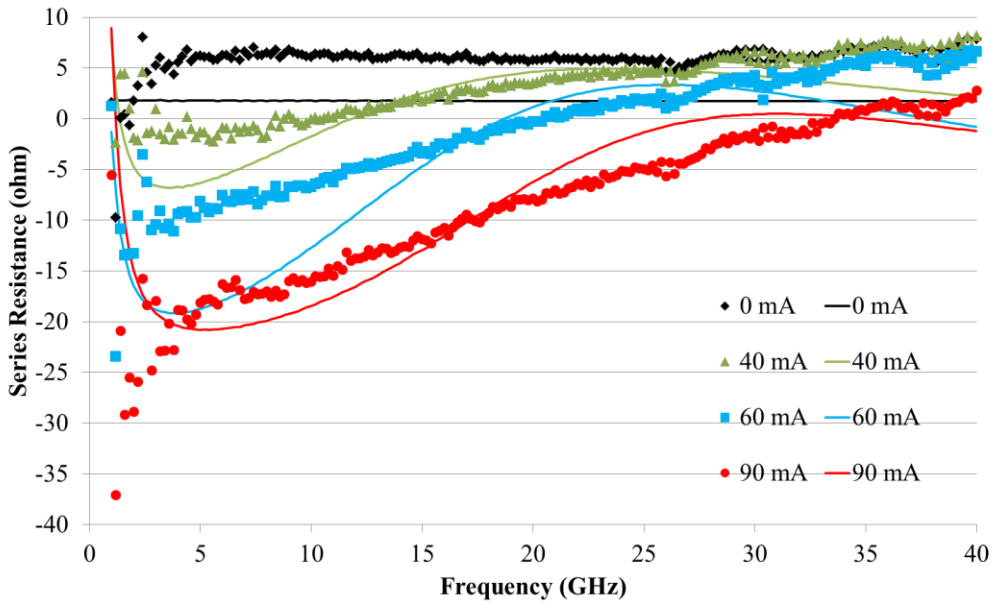

Figure 4.15 Measured (scatter points) and simulated (solid lines) series resistance of 28µm MUTC-4 photodiode at -5V

The series resistance of the MUTC-4 photodiode structure has also been calculated using Crosslight Apsys. Figure 4.15 compares the measured and simulated series resistance of a 28µm-diameter photodiode at -5V. At dark condition, both the measured and simulated resistance are independent of frequency. The simulation tends to underestimate the dark resistance since it does not take contact/air-bridge resistance into consideration. As photocurrent increases, the series resistance begins to drop, most notably at low frequency end. The difference between the resistance at dark condition and illumination can be

seen as the value of NDR. The fact that the NDR in an MUTC-4 photodiode exits at relatively low frequency and over a broad frequency range indicates that it may have an origin different from NDR in an IMPATT diode [83] or some HBTs [90, 91], which originate from transit and injection delays [92, 93], although the MUTC photodiode does have similar carrier injection and drift regions.

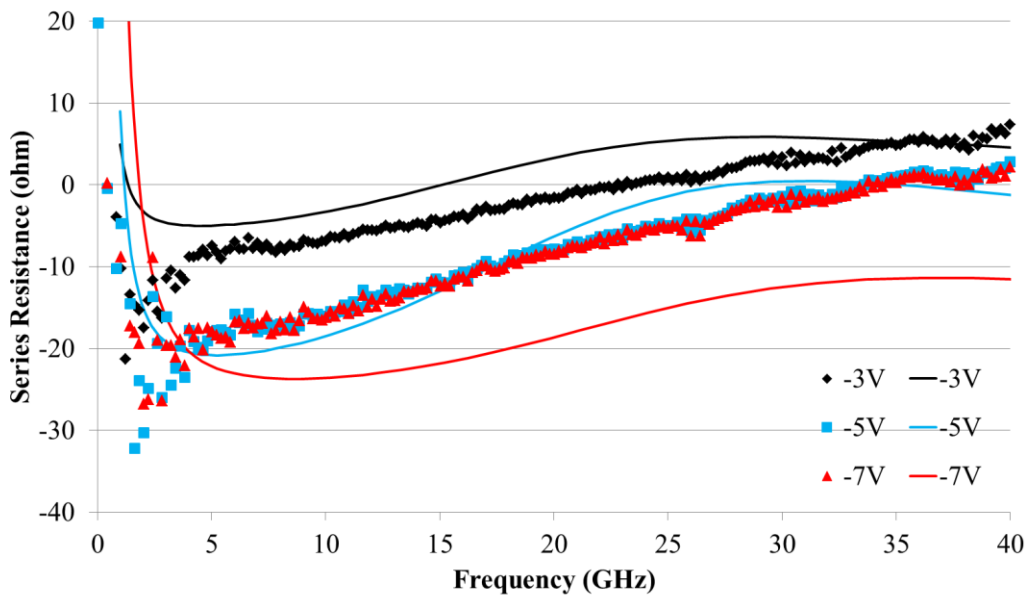

Figure 4.16 Measured (scatter points) and simulated (solid lines) series resistance of 28 µm diameter MUTC-4 photodiode at 90 mA photocurrent

Figure 4.16 shows measurement and simulation results of the series resistance of a 28µm diameter MUTC-4 photodiode at 90 mA photocurrent and different bias voltages. Figure 4.17 illustrates the corresponding electric field distribution inside the device. The photodiode has the smallest NDR at -3V, despite the fact that at this bias voltage the portion of electric field in the InP collector that falls in the negative differential mobility regime (10 kV/cm ~ 35

kV/cm) is the largest. This argues against the view that NDR is introduced by transferred electron effect in the InP collector. The fact that the NDR stops growing after the bias voltage exceeds a certain limit has been observed at other photocurrent levels as well (data not shown here). It suggests that the NDR depends on both photocurrent and bias voltage.

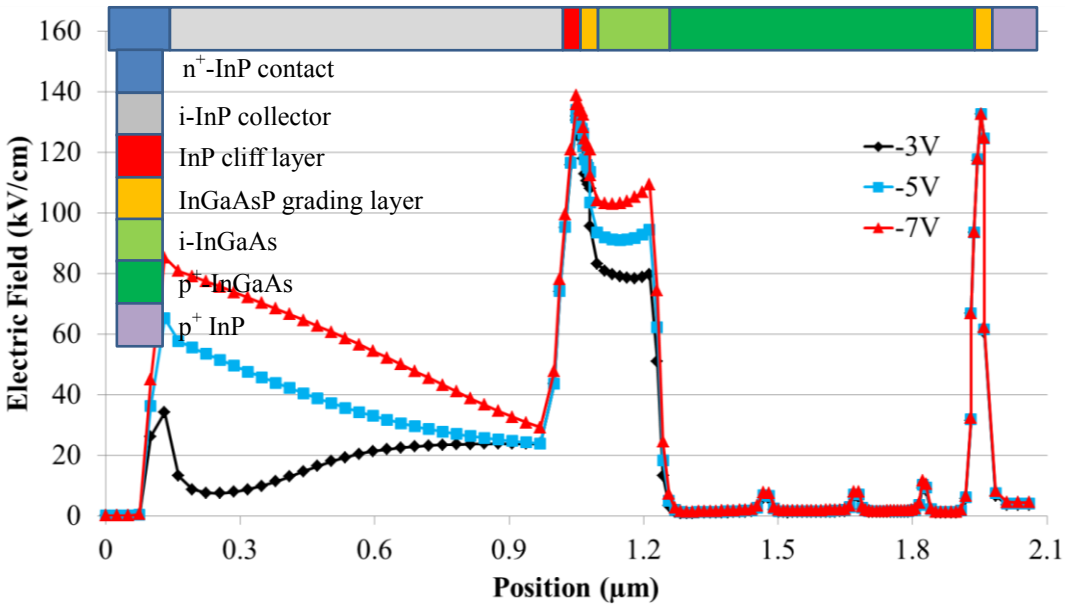

Figure 4.17 Electric field profile in a 28 µm-diameter MUTC-4 photodiode at 90 mA photocurrent

A heterojunction barrier can sometimes introduce NDR in semiconductor devices. Most cases involve tunneling in thin quantum well structures [94] or the real-space electron transfer effect that is utilized in High-Mobility Electron Transistors (HEMTs) [95]. Both are unlikely to occur in the MUTC-4 photodiode structure due to its physical dimensions. To investigate the influence of heterojunctions I have used the model to calculate the series resistance of MUTC-

4 photodiode structures with several variations related to heterojunction barrier and material properties. The results are shown in Figure 4.18. First the energy barrier between the InGaAs absorber and the InP collector is removed by forcing the InP to assume the same bandgap and affinity as InGaAs, but light absorption is prevented. The resulting change in NDR is negligible. Another heterojunction barrier in the MUTC-4 structure is located between the p-InGaAs absorber and the p-InP electron blocking layer. When it is removed, the NDR becomes much smaller but still exists. This seems to suggest that the carrier dynamic around this heterojunction barrier interface is a major contributor to the NDR. Another simulation changes the electron transport in InP from a GaAs-like model with negative differential mobility to a Si-like model. This change only causes a relatively small reduction of the NDR and preserves its frequency dependence. This indicates that the transfer electron effect, or Gunn effect [96], in InP may only play a minor role here. It is worth mentioning that the saturation effect in the MUTC-4 photodiode is more severe when the Si-like transport model is employed for InP due to reduced electron velocity. The saturation results in larger positive resistance, which would further reduce the role of the transfer electron effect.

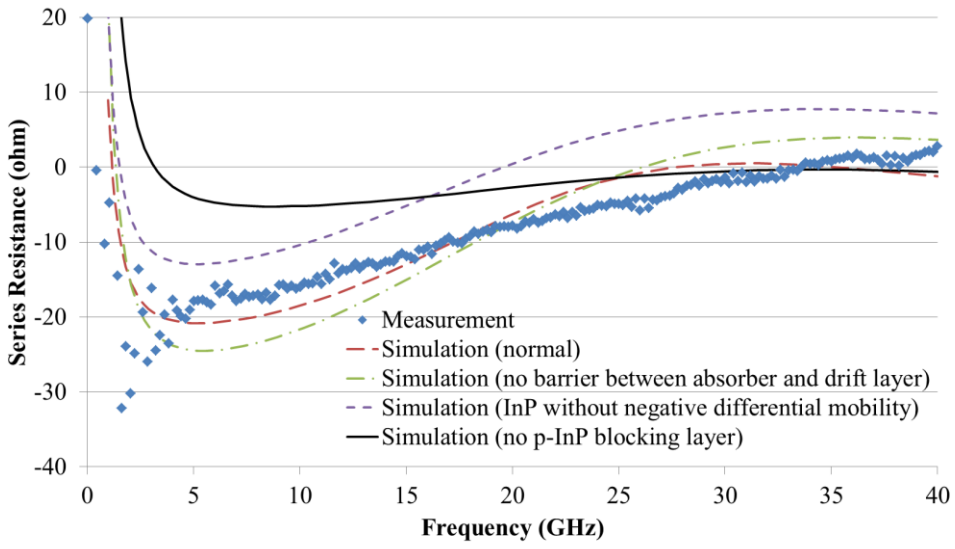

Figure 4.18 The series resistance of a 28µm diameter MUTC-4 photodiode at -5V and 90 mA photocurrent. Simulation results assuming different material properties are compared with measurement.

I have also simulated MUTC photodiodes with different p-type doping concentrations in the undepleted InGaAs absorber, since there is evidence in Figure 4.18 that indicates the carrier dynamics near the anode may give rise to the NDR. As we can see from Figure 4.19, the NDR disappears at low doping concentrations, where the absorber is almost completely depleted. The value of NDR essentially doesn't change after the doping concentration exceeds 0.5 times of its original level. The maximum electric field inside the p-type absorber is approximately 1.5 kV/cm at this doping level, which means that the absorber can be considered quasi-neutral. As a result the holes respond to minority carrier or electron concentration changes almost instantaneously (within dielectric relaxation time <1.0 ps). Therefore the NDR most probably originates from

electron diffusion inside the p-type InGaAs absorber. The existence of the InP blocking layer apparently enhances this effect by increasing the directivity of electron diffusion.

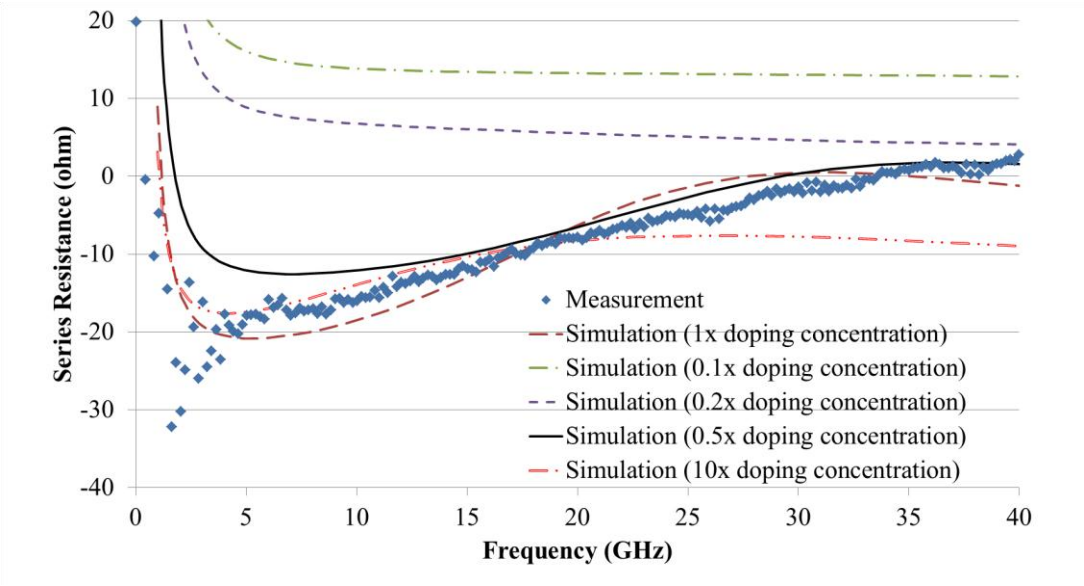

Figure 4.19 The series resistance of a 28 µm-diameter MUTC-4 photodiode at -5V and 90 mA photocurrent. The p-type doping concentration in the undepleted InGaAs absorber is changed from 1/10 to 10 times its original value ($5\times10^{23}cm^{-3}$ to $2\times10^{24}cm^{-3}$).

4.3 Summary

In this chapter, the impedance and bandwidth of MUTC-4 photodiodes have been systematically characterized. Both small-signal impulse response and two-laser heterodyne tests show similar bandwidth results, which indicate that the DC current offset rather than the RF component is the primary factor determining the 3-dB bandwidth. The S-parameter measurement reveals the existence of NDR

while the photodiode is under optical illumination. A model for the MUTC-4 photodiode is established using Crosslight Apsys software and the simulation results agree well with measurement data. The model is also used to investigate the origin of NDR, which has been traced back to the p-type InP electron blocking layer and the carrier transport in the undepleted InGaAs absorber. The discovery of NDR and establishment of the model improves our understanding of the fundamental operation of MUTC photodiodes and will be useful for future photodiode development.

Chapter 5 MUTC Photodiode Array with Monolithically Integrated Wilkinson Combiner

5.1 Introduction

Power combining is widely used to increase the power output from various electronic devices. The linearity of the system also improves due to reduced power level on each device being combined. Photodiode arrays with integrated microwave circuits have been the subject of numerous research programs. V. J. Urick reported a four-photodiode array with 28 dBm third-order intercept point (OIP3) at 5 MHz [97]. S. Itakura achieved 32.6 dBm of OIP3 at 5 GHz using a four-element photodiode array with hybrid integration [98]. A photodiode array was also used to generate sub-terahertz radiation by N. Shimizu and T. Nagatsuma [99].

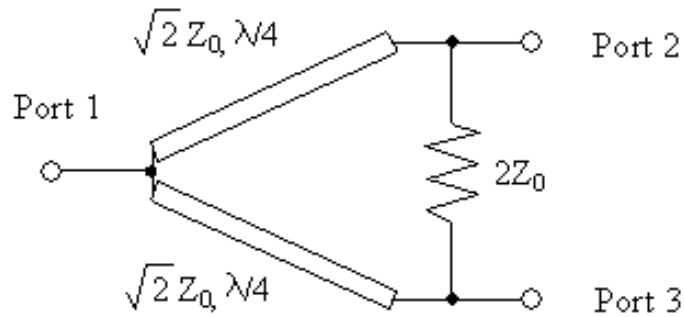

Figure 5.1 Schematic diagram of a 2×1 Wilkinson power combiner. Z_0 is the system characteristic impedance.

The Wilkinson power combiner was invented by E. J. Wilkinson in 1960 [100] and has many applications in RF systems. In its simplest form, as shown in Figure 5.1, a 2×1 Wilkinson combiner consists of two quarter-wave (90-degree) transmission lines and an isolation resistor. Assuming the system has a characteristic impedance of Z_0, the quarter-wave transmission lines have an impedance of $\sqrt{2}Z_0$ and the resistor is $2Z_0$. The scattering matrix for the 2×1 Wilkinson combiner at its center frequency is:

$$\boldsymbol{S} = \begin{bmatrix} \mathbf{0} & -\frac{\boldsymbol{j}}{\sqrt{\mathbf{2}}} & -\frac{\boldsymbol{j}}{\sqrt{\mathbf{2}}} \\ -\frac{\boldsymbol{j}}{\sqrt{\mathbf{2}}} & \mathbf{0} & \mathbf{0} \\ -\frac{\boldsymbol{j}}{\sqrt{\mathbf{2}}} & \mathbf{0} & \mathbf{0} \end{bmatrix} \tag{5.1}$$

The Wilkinson combiner adds the power of the two equal-phase input signals at port 2 and 3 and the output signal is at port 1. The output power is 3 dB

larger than either of the inputs, while the voltage swing at the input ports does not change. This is different from the case for the direct connection of two input ports, where the currents are added together. For this configuration of a "current" combiner, the output power is 6 dB larger than either of the inputs, but the voltage swing at both input ports equals that at the output, which is twice their original value. The ability to increase the total output power while maintaining the voltage swing at input ports is a major advantage of the Wilkinson power combiner. Larger voltage swing causes the devices connected to the input ports, e.g. photodiodes in this work, to saturate earlier and generate more nonlinear distortions. This is the main reason why I chose to integrate a Wilkinson power combiner with high-power, high-linearity photodiodes.

Figure 5.2 shows S-parameters of an ideal 2×1 Wilkinson power combiner designed for a center frequency of 20 GHz. The fractional bandwidth is ~ 30% determined from -20 dB reflection points.

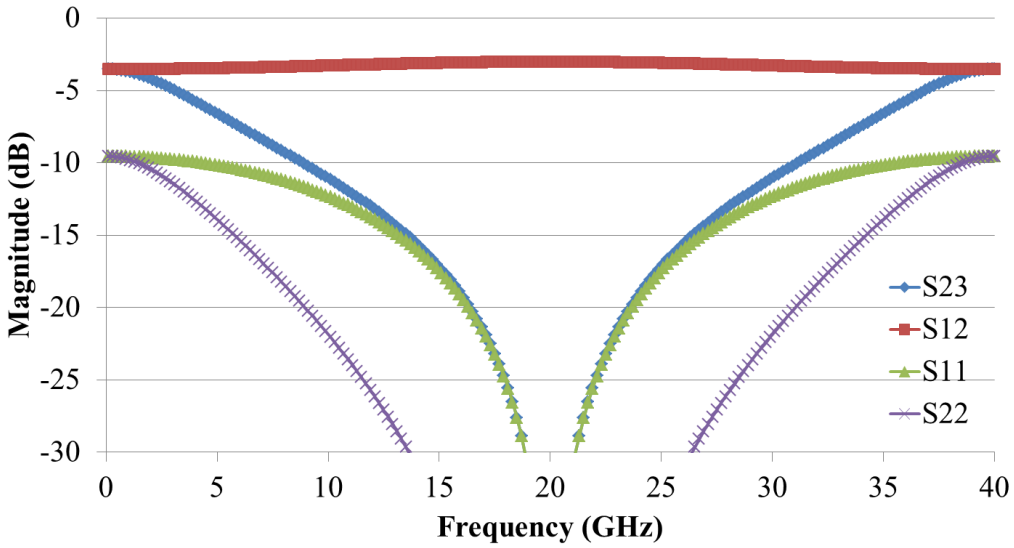

Figure 5.2 The S-parameters of an ideal 2×1 Wilkinson power combiner with 20 GHz center frequency

The Wilkinson power combiner is matched at all three ports. The same circuit can be also used as a divider since it only consists of passive components and is thus reciprocal. The Wilkinson combiner provides good isolation between the two input ports at the center frequency. There is no power dissipation in the ideal circuit if the input signals are in phase. Multiple-stage structures can be used to combine more input signals. In this chapter, I will demonstrate photodiodes monolithically integrated with 2×1 and 4×1 Wilkinson combiners.

5.2 First generation circuits

5.2.1 Design and fabrication

An InGaAs/InP PDA photodiode with heavily-doped absorber (HD-PDA) [101] was used in the first generation circuits. Figure 5.3 shows its epitaxial structure. The motivation for utilizing heavily-doped absorbing layers is to decrease the frequency dependence of OIP3 through reduced variation of junction capacitance with bias voltage [45, 101]. The photodiodes used in this study have a diameter of 40 μm.

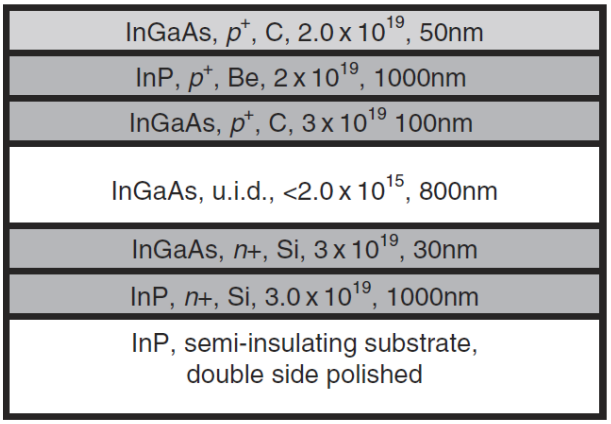

Figure 5.3 The epitaxial structure of the HD-PDA photodiode [101]

The center frequency for this work is 20 GHz. I used the Agilent ADS momentum software for the electromagnetic (EM) design and simulation. An open-stub tuner was designed to match the photodiode impedance to 50 ohm at the center frequency. The layouts for the combiner and stub tuner are shown in

Figure 5.4. The circuits without integrated photodiodes are for S-parameter measurement. Air-bridges are placed in the vicinities of discontinuities (bends, tees and steps) to equalize potential on both ground planes and suppress spurious modes. The distance between the photodiodes (0.5 mm) is determined by the pitch of the fiber array for optical coupling. Thru-Reflect-Line (TRL) patterns for 2-port calibration are included in the same layout for de-embedding.

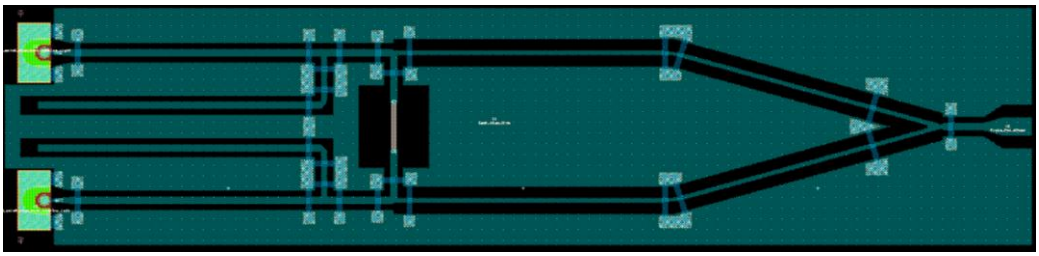

(a)

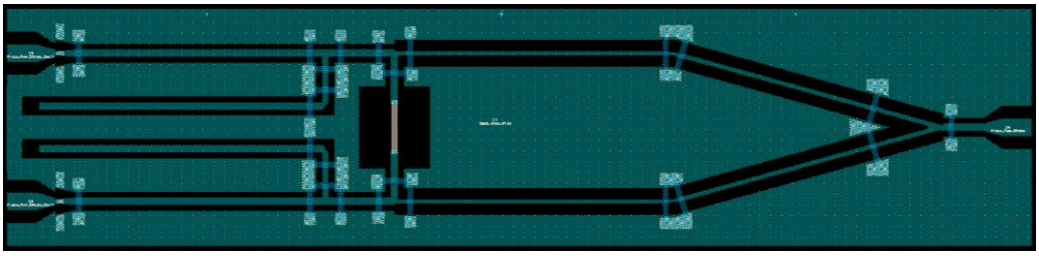

(b)

(c)

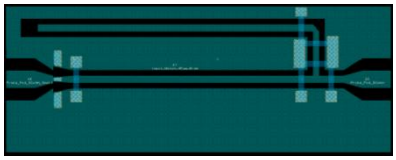

(d)

Figure 5.4 The layouts of the (a) 2×1 Wilkinson power combiner with HD-PDA photodiode pair, (b) 2×1 Wilkinson power combiner without photodiodes, (c) open-stub tuner and the HD-PDA photodiode and (d) open-stub tuner without photodiode. Dimensions: (a) and (b) 3.5 mm × 0.8 mm, (c) and (d) 1.3 mm

× 0.5 mm.

The circuits are fabricated on the same semi-insulating (SI) InP substrate as the photodiode using plated gold CPW transmission lines. The thin film resistor is made of evaporated titanium. Pictures of completed circuits are shown in Figure 5.5. A discrete photodiode is included for comparison. The test structures are not shown here. The three structures in Figure 5.5 will be referred to as Structure A, B and C in this chapter.

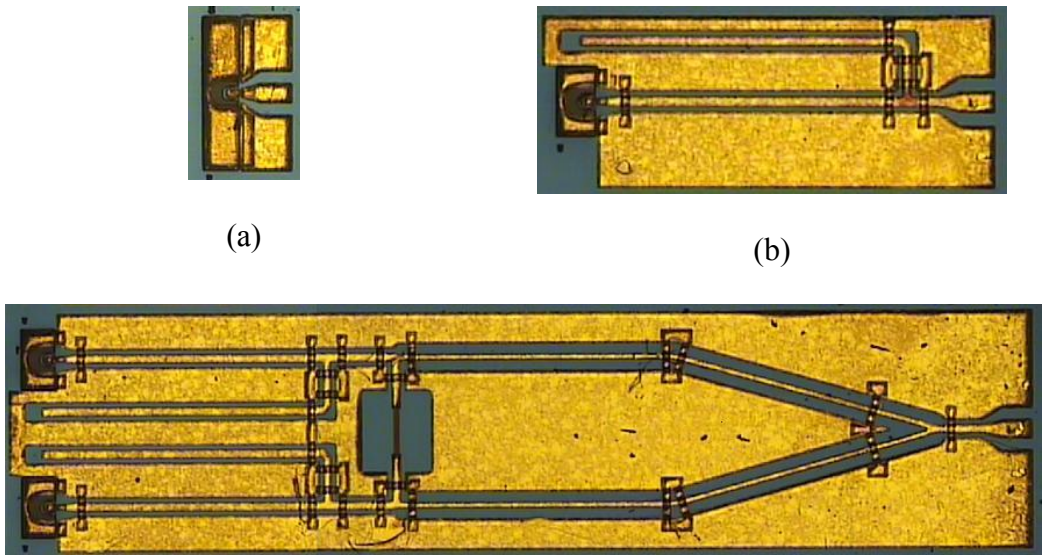

(a) (b) (c)

Figure 5.5 (a) Structure A: HD-PDA photodiode with its electrical output signal directly coupled to testing CPW pads. (b) Structure B: HD-PDA photodiode with an open-stub tuning circuit, followed by the same CPW pads in (a), and (c) Structure C: two HD-PDA photodiodes with the same open-stub tuning circuits coupled to the two input ports of a Wilkinson power combiner.

5.2.2 S-parameter measurements

The S-parameters was measured using the HP8510C vector network analyzer (VNA). TRL calibration was used to de-embed the impedance of the contact pads. The frequency range in the measurement (5~40 GHz) was limited by the length of the line standard in the on-wafer TRL patterns. Although the Wilkinson power combiner is a 3-port circuit, only 2-port S-parameters can be measured since there are only two test ports on the HP8510C VNA. The remaining port in the test structures was left open. The 2-port S-parameters still serve as good performance indicators for the circuits. The measurement results for the test circuits (the ones without integrated photodiodes) are compared with ADS momentum simulation in Figure 5.6 and there is good agreement.

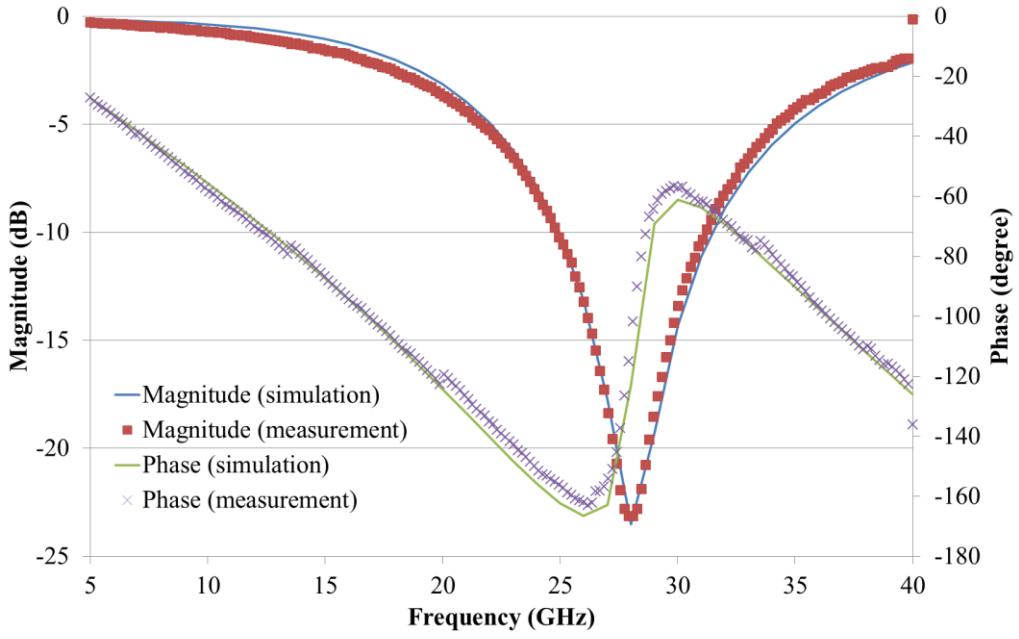

(a)

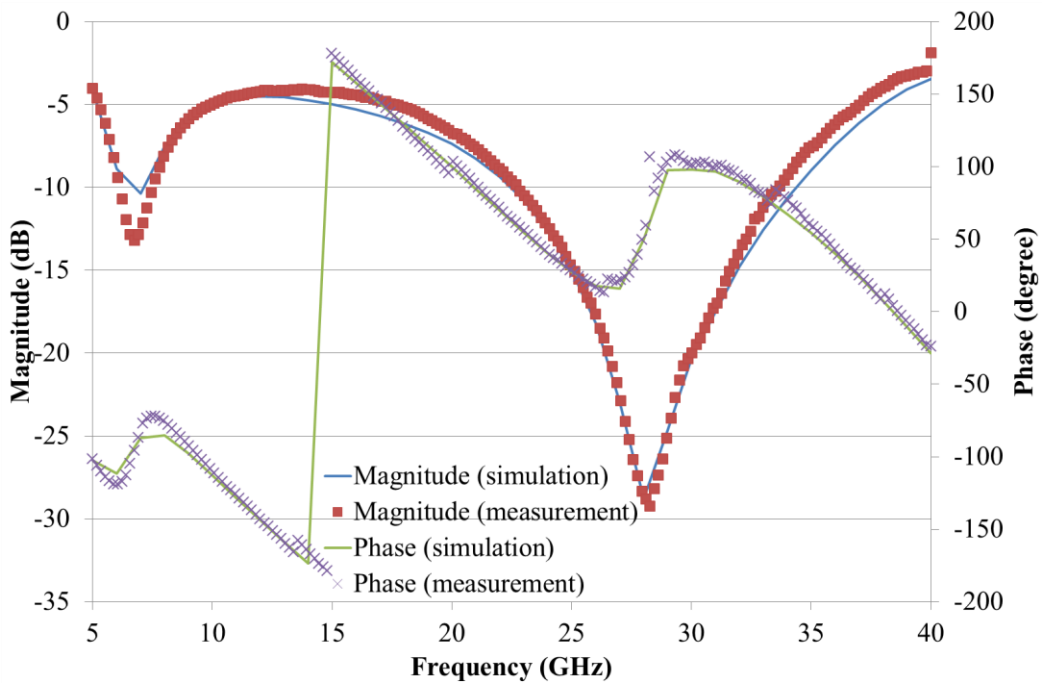
0
-5
-10
-15
-20
-25
-30
-35
Magnitude (dB)
200
150
100
50
0
-50
-100
-150
-200
Phase (degree)
5
10
15
20
25
30
35
40
Frequency (GHz)
Magnitude (simulation)
Magnitude (measurement)
Phase (simulation)
Phase (measurement)

(b)

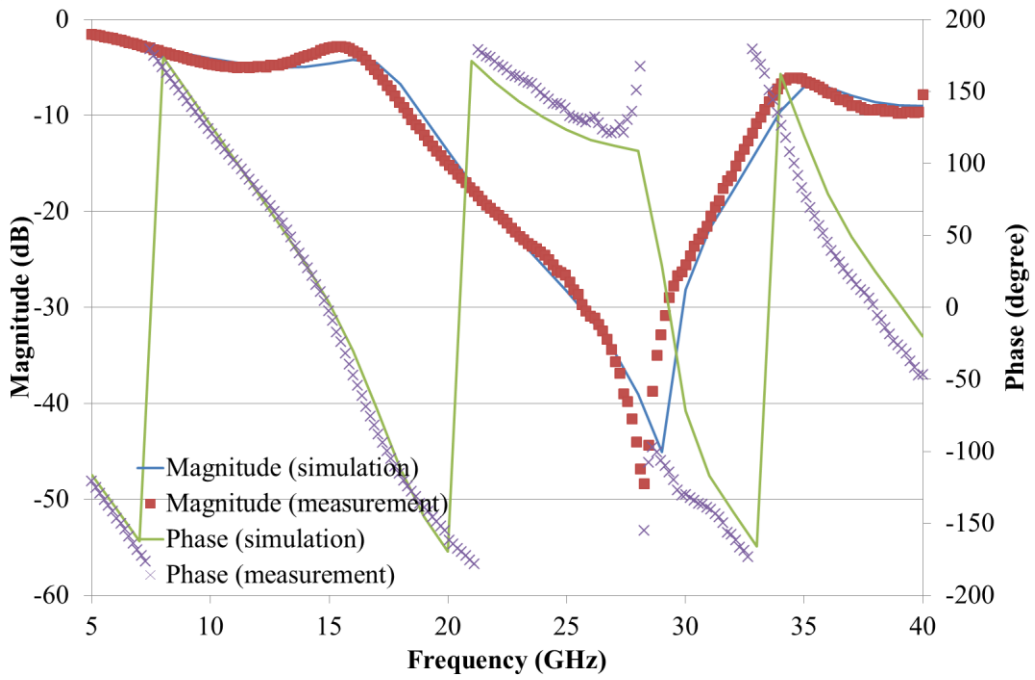

(c)

Figure 5.6 Comparison of measured and simulated (a) S12 of the stub tuner in Error! Reference source ot found.**(d), (b) S12 and (c) S23 of the Wilkinson combiner with stub tuner (port-1 is the output port) in** Error! Reference source not found.**(b) .**

The RF resistance of the 100 ohm Ti thin film resistor (TFR) has beeen extracted from S-parameter measurement, as shown in Figure 5.7. The S-parameters of the Ti TFR (Figure 5.7(a)) is very close to that of an ideal 100 ohm resistor. The layout of the resistor test pattern is also included as the inset. The resistances seen from both sides of the Ti TFR were calculated from S11 and S22 and shown in Figure 5.7 (b). The 50 resistance of the test ports were subtracted from the calculation results. The resistance was 100~110 ohm across the whole frequency range. The fractional error was less than 10%.

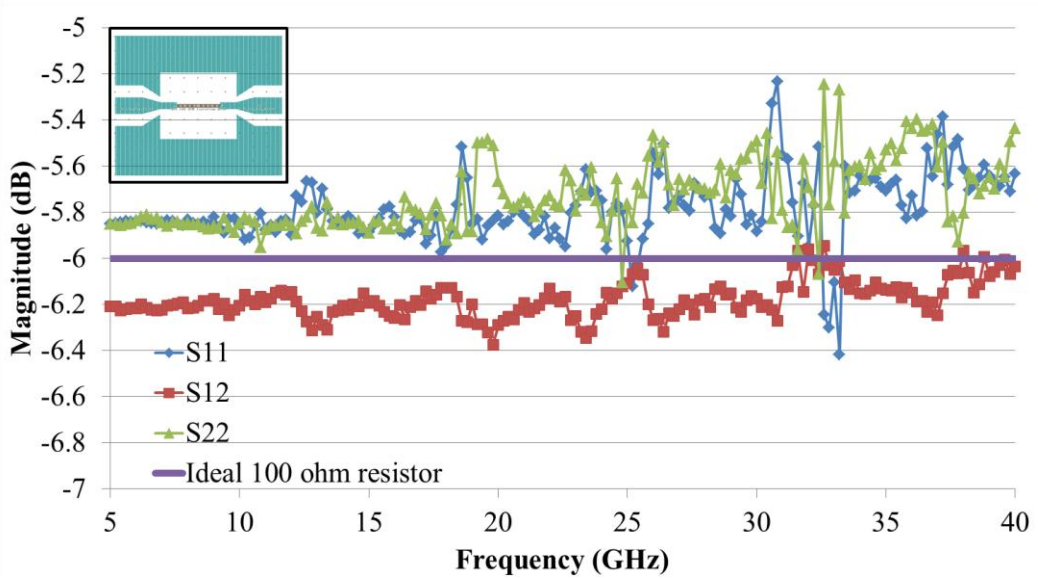

(a)

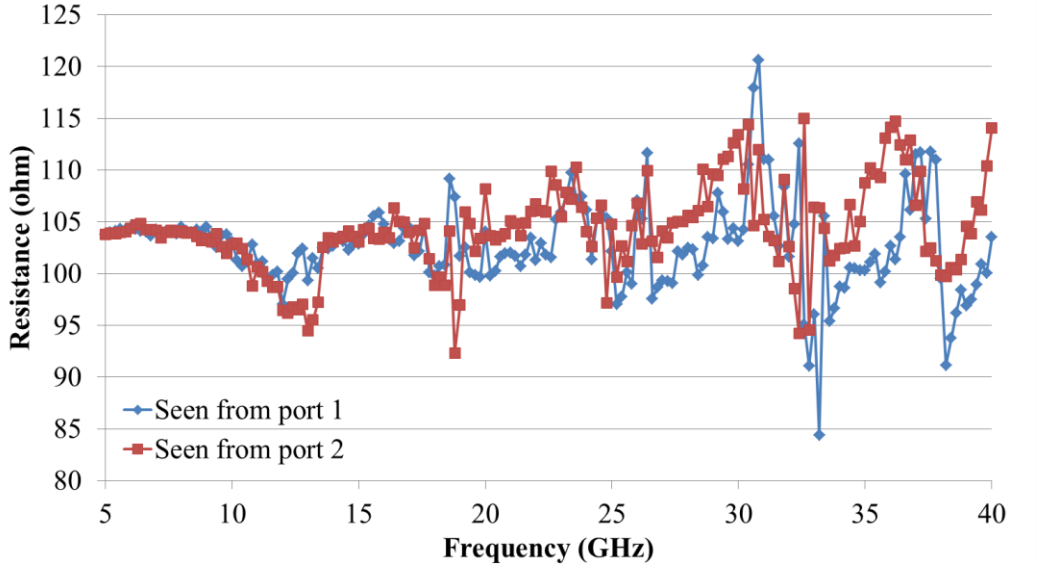

(b)

Figure 5.7 (a) S-parameters of the Ti thin film resistor and an ideal 100 ohm resistor, and (b) the resistance seen from both ports extracted from the S-parameter measurement. The inset in (a) shows the layout of the resistor test pattern. The 50 ohm resistance of the test ports has been subtracted from (b).

Only 1-port S-parameters were measured on Structure B and C, since other ports were terminated by the HD-PDA photodiodes. The results are shown in Figure 5.8. The matching frequency is very close to 20 GHz, with a bandwidth of approximately 3 GHz (-10 dB reflection).

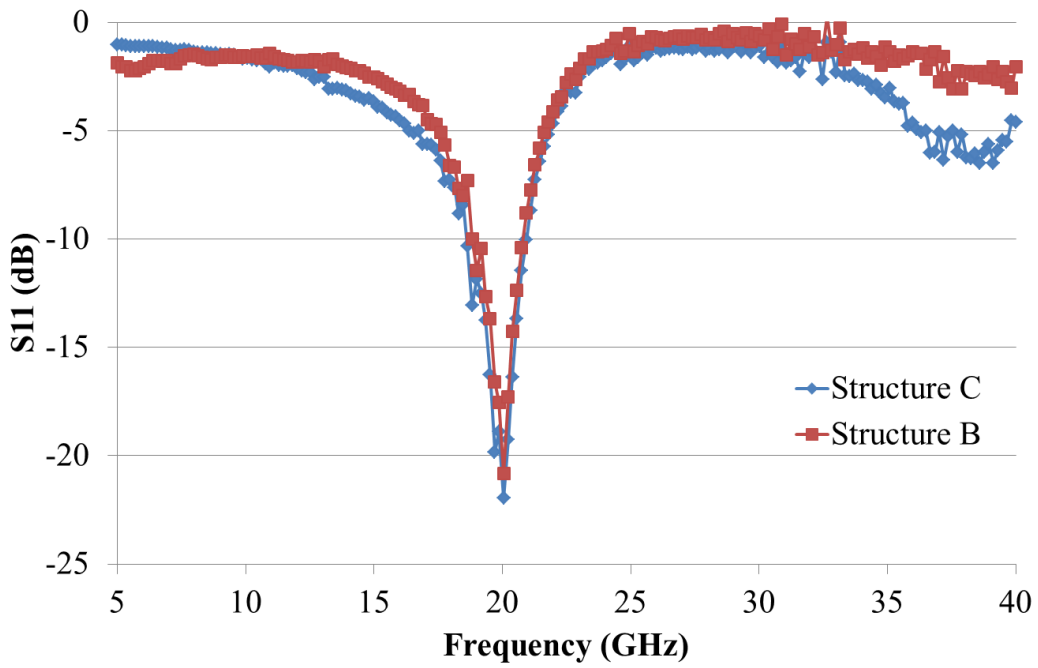

Figure 5.8 The S-parameters of Structure B (single photodiode with stub tuner) and C (photodiode pair with stub tuner and the 2×1 Wilkinson power combiner)

5.2.3 Frequency response measurements

The frequency responses of the three structures were measured using the two-laser heterodyne method described in Chapter 2. The experimental setup was modified to accommodate the photodiode array. The output of an EDFA is split

into two branches, with fiber stretchers and optical attenuators placed in each branch to balance the phase and magnitude of signals. A 2-element lensed fiber array was used to illuminate both photodiodes in Structure C. The frequency response measurements of all three structures were carried out at 1 mA photocurrent and 5 V reverse bias. This means that the total photocurrent for Structure A and Structure B was 1 mA, while that for Structure C was 2 mA. The measurement results are normalized to the output power from Structure C at 0.5 GHz, the lowest measured frequency.

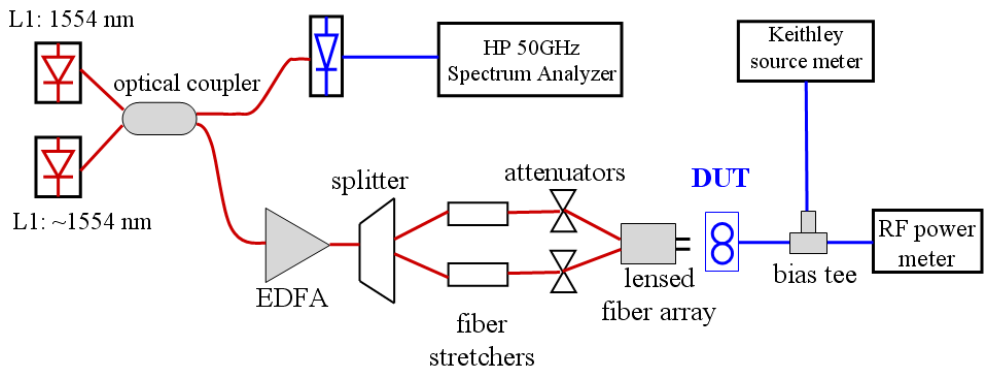

Figure 5.9 The frequency response measurement setup for the photodiode array.

As shown in Figure 5.10, the output power of Structure A decreases monotonically with frequency. The 3-dB bandwidth of Structure A is 13 GHz. The output power of Structure B reaches a maximum at 20 GHz, which is due to the resonance associated with the open-stub tuning circuit. The output power of Structure C at low frequencies is 6 dB higher than that of Structure A or Structure B. This is due to the fact that the Wilkinson combiner does not have isolation between the two input ports at frequencies that are much lower than its designed

center frequency (20 GHz) and thus the photocurrents from the two photodiodes directly combine. At 20 GHz Structure C shows a resonance effect similar to that of Structure B, but its maximum power at 20 GHz is 2.6 dB higher than that of Structure B. This is close to the theoretical value of 3 dB enhancement for the 2×1 Wilkinson power combiner.

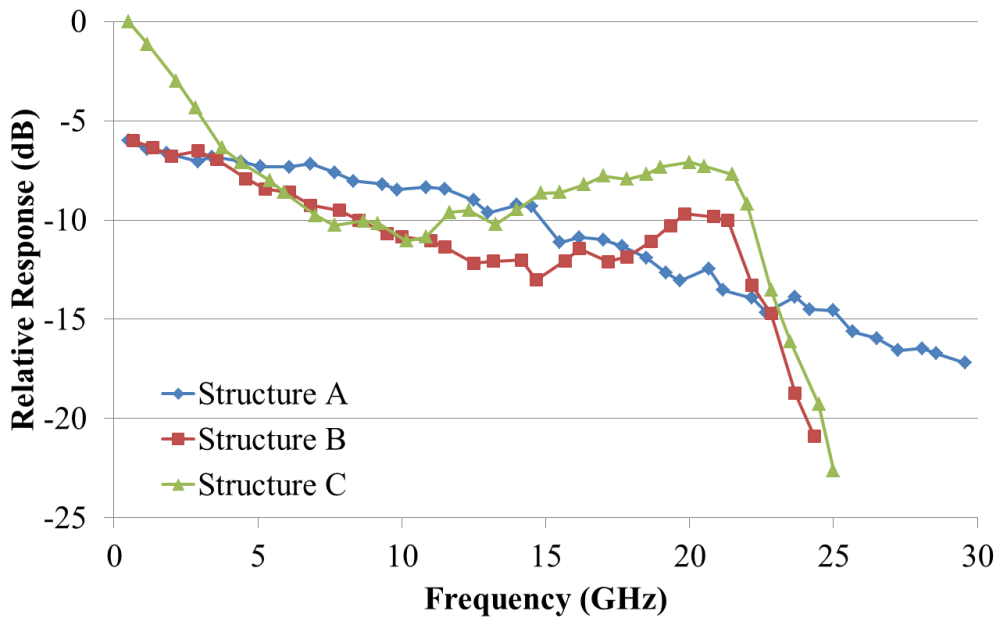

Figure 5.10 Relative frequency response of Structures A, B, and C measured at 1 mA photocurrent and 5V reverse bias.

5.2.4 Measurement and simulation of OIP3

The frequency dependence of OIP3 for the discrete HD-PDA photodiodes (Structure A) with and without the open-stub tuning circuits (Structure B) was measured using the three-tone technique described in Chapter 2. The maximum

measurement frequency of 20 GHz was limited by the signal generators used in the three-tone setup. The wavelengths of the lasers in the three-tone setup were 1541 nm, 1542 nm and 1543 nm. The three fundamental RF signals that were used to modulate the lasers were spaced at 9.6 MHz and 10.4 MHz intervals. The photocurrent and bias were the same for both devices. The OIP3 of Structure A shows little dependence on frequency, which is similar to the results reported in [101]. However, the OIP3 of Structure B, which has a resonance at 20 GHz, increases with frequency, reaches its maximum at 12.3 GHz, and then decreases. This illustrates an interesting performance trade-off; at 12.3 GHz, where the output power of the photodiode reaches a minimum, the OIP3 exhibits its maximum, while at the resonance frequency of 20 GHz, the output power maximum coincides with an abrupt drop in the OIP3.

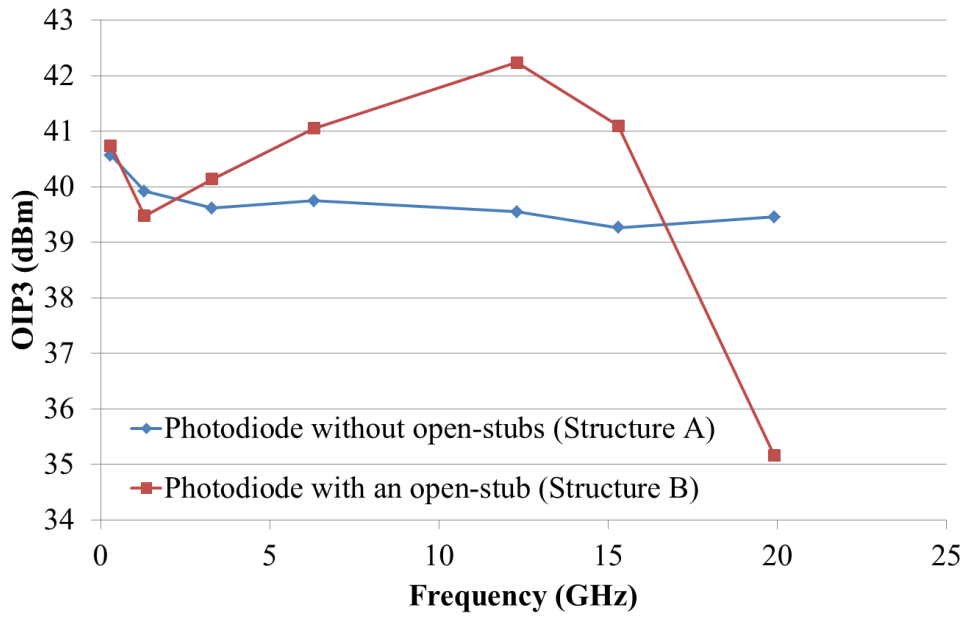

Figure 5.11 Measured OIP3 of HD-PDA photodiodes with and without open-stub at 25 mA photocurrent and 8 V reverse bias.

The photocurrent induces a voltage drop across the series and load resistances. As a consequence, the bias voltage across the photodiode junction is modulated by the photocurrent [42], which will be referred to as "voltage swing" in the following analysis. It has been shown that the change in responsivity caused by the voltage swing is the primary reason for nonlinearities at low frequencies in the HD-PDA photodiodes [101]. Assuming that V_{Load} and V_{PD} are the amplitudes of the voltage swings across the load and photodiode, respectively. In Structure A, where the photodiode is directly connected to the CPW test pad, V_{Load} and V_{PD} are almost the same in the frequency range up to 50 GHz assuming negligible loss on the CPW pad. However, for Structure B, due to the open-stub tuning circuit, V_{Load} and V_{PD} are not the same for all frequencies. V_{Load} and V_{PD} for both Structure A

and Structure B were simulated using Agilent ADS from DC up to 50 GHz. The equivalent circuit model for the PD used in simulation is shown in Figure 5.12. The measured 2-port S-parameters were used for the simulation of the stub tuner.

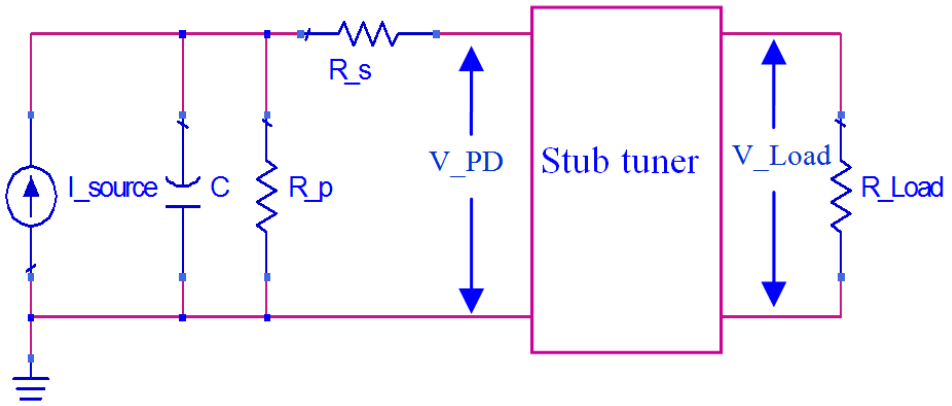

Figure 5.12 The equivalent circuit model used for OIP3 simulation.

The simulation results are shown in Figure 5.13. The ratio of V_{PD} of structure A to that of structure B should not be dependent on photocurrent as long as no significant saturation occurs in the photodiodes. Thus the photocurrent was fixed at 10 mA with 100% modulation for all photodiodes in the simulation. The photodiode voltage swing and that for the load are the same for structure A up to 50 GHz, and thus only the load characteristic is shown for Structure A. The monotonic decrease of the voltage swing across the load with frequency is due to the RC time constant of the junction capacitance and the 50 ohm load. However, for Structure B, the voltage swing across the photodiode shows significant differences compared to the load when the frequency is higher than 7 GHz. The load voltage swing and thus the output power reach a minimum near 12.5 GHz,

where the mismatch between the impedance of the photodiode and that of the load is greatest. At this point the voltage swing across the load is 1.4 times larger than that for the photodiode. Near 20 GHz, where the impedance of the photodiode is well matched to the load, the load voltage swing and the output power exhibit a maxima. At this point the voltage swing across the load is 1.7 times smaller than for the photodiode.

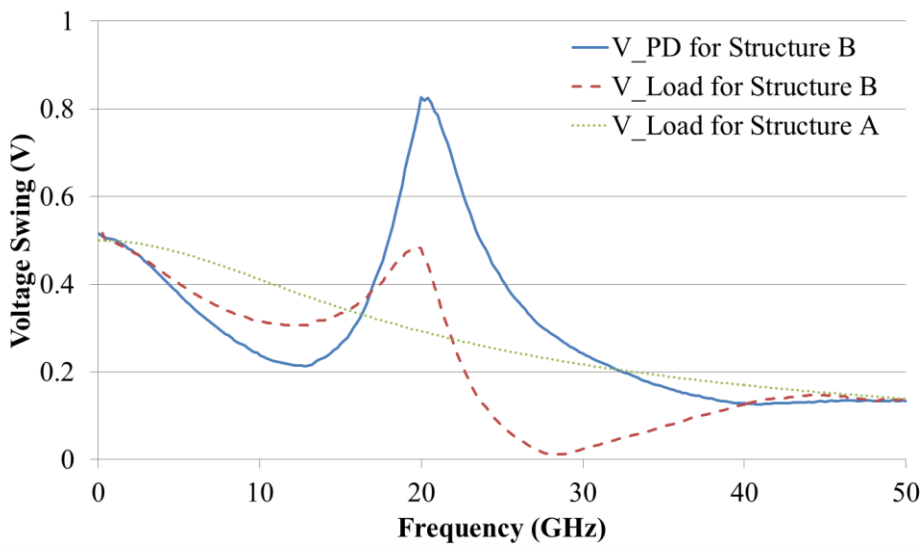

Figure 5.13 Simulation of the amplitude of the voltage swing versus frequency for 10 mA photocurrent. Solid and dashed lines are voltage swing amplitudes across the photodiode and the load resistor, respectively, for structure B. Dotted line: voltage swing amplitude across the load for structure A.

By definition, OIP3 = $P_f + (P_f - P_{IMD3}) / 2$ with P_f and P_{IMD3} measured in dBm. The output power of the fundamental signal on the load can be expressed as $P_f = a \cdot V_{Load}^2$, where a is a constant. If the voltage-dependent nonlinearity is the only source of nonlinearity in the photodiode (i.e. photocurrent-dependent nonlinear terms are negligible), the power of the third-order intermodulation on

the load, which is produced by a second order nonlinear process, is given by the relation: $P_{IMD3} = b \cdot (V_{PD}^3)^2$, where b is a constant that represents the strength of the nonlinear effect. Thus, by definition, $OIP3 = 10log\left[\frac{a^{\frac{3}{2}}}{b^{\frac{1}{2}}}\left(\frac{V_{Load}}{V_{PD}}\right)^3\right]$. For the case of Structure A, $V_{Load} = V_{PD}$ for all frequencies, and thus$OIP3 = 10log\left[\frac{a^{\frac{3}{2}}}{b^{\frac{1}{2}}}\right]$. For the case of Structure B, V_{Load} / V_{PD} changes with frequency, and thus the OIP3 is also frequency dependent. Since the photodiode structures are the same in Structures A and B, the frequency dependence of $\frac{a^{\frac{3}{2}}}{b^{\frac{1}{2}}}$ can be assumed to be the same for both structures. Thus the difference between the OIP3 of the two structures can be represented as:

$$\boldsymbol{OIP\ improvement = OIP3_B - OIP3_A = 10log\left[\left(\frac{V_{Load}}{V_{PD}}\right)^3\right]} \quad \textbf{(5.2)}$$

The simulated OIP3 improvement is calculated from the simulated voltage swing on the load and the photodiode using equation (5.2). Figure 5.14 compares the measurements and the simulation. The good agreement between the two suggests that the tuning circuits can improve the linearity of the photodiode at the cost of reducing output power due to the reduced voltage swing at non-resonating frequencies. At 12.3 GHz, Structure B exhibits an OIP3 of 42.2 dBm, which is a 3 dB improvement relative to Structure A.

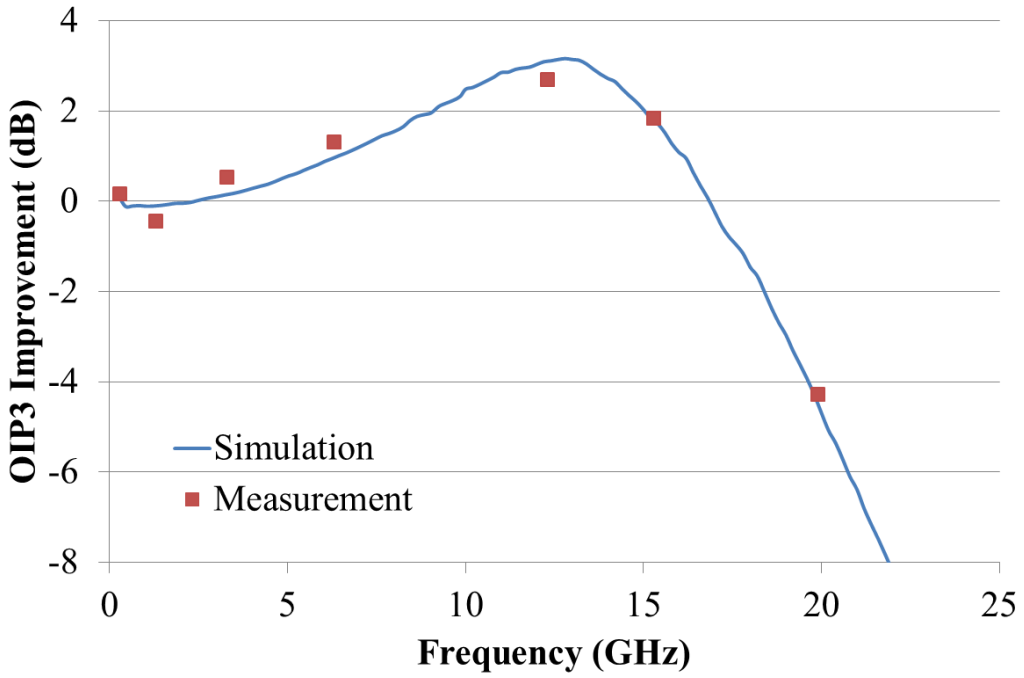

Figure 5.14 Frequency dependence of OIP3 improvement for Structure B compared with Structure A.

The power of the fundamental tones P_f and third-order intermodulation products P_{IMD3} of Structure C will have approximately the same gain of 3dB near 20 GHz compared to Structure B, assuming the same current and bias conditions for the photodiodes in both circuits. Hence, the OIP3 of Structure C would be projected to be 3 dB higher than that of Structure B. Table 5.1 compares the OIP3 of structures B and C. The photocurrent in Table 5.1 refers to the photocurrent of each photodiode, and thus the condition of "8 V, 10 mA" corresponds to 10 mA for Structure B and 10 mA for each photodiode in Structure C. This provides a realistic comparison since the OIP3 of the photodiode might be different under different photocurrent and bias conditions. As shown in Table 5.1, for the same

conditions, the OIP3 of Structure C shows an improvement of approximately 3 dB relative to Structure B.

Conditions	8V, 10 mA	6 V, 10 mA	6 V, 15 mA
Structure B	32.6 dBm	31.3 dBm	31.5 dBm
Structure C	36.9 dBm	35.0 dBm	34.1 dBm
Improvement	4.3 dB	3.7 dB	2.6 dB

Table 5.1 OIP3 comparison between Structure B and C at 20 GHz.

5.3 Second generation circuits

The first generation circuits demonstrated the feasibility of using an integrated Wilkinson combiner to improve the power and linearity performance of photodiodes. I expanded this work in the second generation circuits to include a 4×1 Wilkinson combiner and photodiodes with higher performance. The circuits were also measured at larger photocurrents.

5.3.1 Design and fabrication

The photodiodes used in the second-generation circuits were the more recently designed MUTC photodiode structure with heavily doped absorber (HD-

MUTC). Device design and characterization are described in [71]. Similar to the HD-PDA structure, the HD-MUTC also utilizes heavy carbon doping in the p-type absorber to reduce the dependence of the junction capacitance on voltage and to increase linearity. The HD-MUTC also has higher power handling capability than the HD-PDA photodiode due to the design focus on high-power capability. The epitaxial structure of the HD-MUTC photodiode is shown in Figure 5.15.

InGaAs, p+, C, $2x10^{19}$, 50nm
InP, p+, Be, $8x10^{18}$, 100nm
InGaAs, C, $8x10^{19}$ – $5x10^{18}$, 650 nm
InGaAs, n.i.d, <$5x10^{15}$, 300nm
InGaAs/InAlAs chirped superlattice, n.i.d. <$5.0x10^{15}$, 24nm
InP, Si, $5x10^{16}$, 5nm
InP, n.i.d, <$5x10^{15}$, 400nm
InP, n+, Si, $3.0x10^{19}$, 1000nm
InP, semi-insulating substrate

Figure 5.15 Epitaxial structure of the HD-MUTC photodiode [71].

For the design of the 4×1 Wilkinson power combiner, a single-stage design would have lower insertion loss and smaller footprint compared to a two-stage design with a tree structure. On the other hand, quarter-wave transmission lines with 100 ohm (2 times the system impedance) characteristic impedance are required. This is hard to realize using CPW on InP substrate (dielectric constant = 12.6). For example, the gap between the center conductor and the ground has to be ~50 μm wide even assuming a narrow center conductor width of 5 μm. The

large gap width would give rise to spurious transmission modes and create difficulties in layout design. The narrow center conductor width would also have high resistance, which may very well negate the low loss benefit of the single-stage design. A less severe problem with the single-stage design is the difficulty of implementing equal path lengths from each input port to the output port in a planar environment. This problem can be partially corrected by using serpentine transmission lines or delaying some the inputs in the optical domain.

As a consequence, I chose the two-stage 4×1 Wilkinson power combiner design shown in Figure 5.16. It consisted of three 2×1 Wilkinson combiners. The open-stub tuners were omitted in order to save chip area. The distance between adjacent photodiodes was reduced to 0.25 mm for the same purpose. The path length from each photodiode to the output was roughly the same as in the first generation circuits. 2×1 Wilkinson combiners were also included in the design. Test patterns were changed from the first generation circuits. Any ports that were not needed during a 2-port S-parameter measurement were terminated with 50 ohm Ti thin film resistors. For example, three of the input ports in Figure 5.16 (b) were terminated, leaving only one input and one output port for transmission measurement. Similar test patterns with different combinations of terminated ports were designed for measuring transmission between other ports (layout not shown in Figure 5.16). The TRL calibration patterns were reused from the first generation circuits.

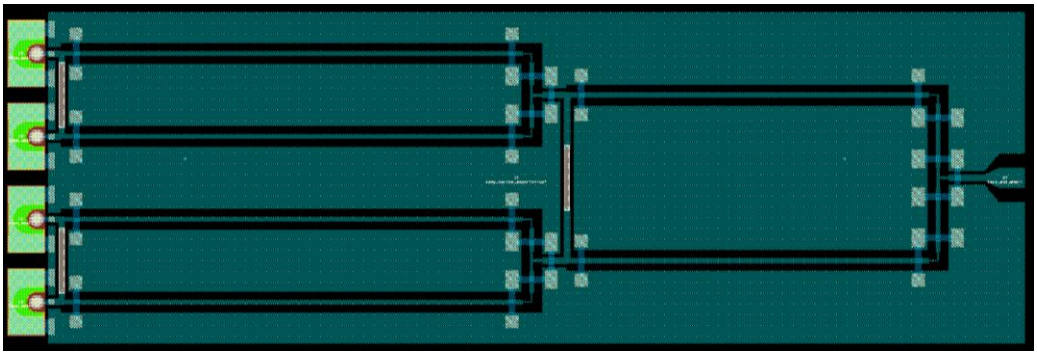

(a)

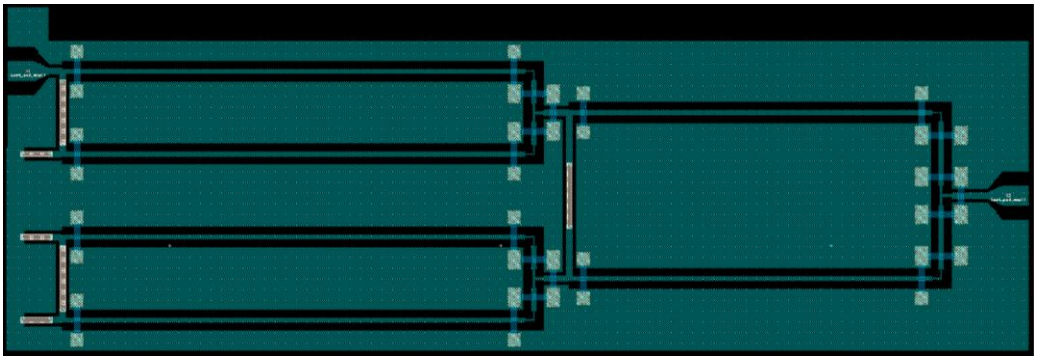

(b)

(c)

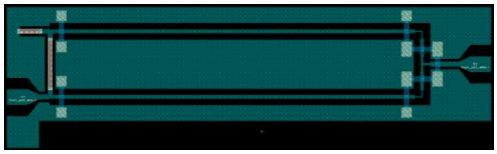

(d)

Figure 5.16 The layouts of (a) 4×1 Wilkinson combiner with 4-elecment photodiode array, (b) 4×1 Wilkinson combiner transmission test pattern, (c) 2×1 Wilkinson combiner and 2-element photodiode array and (d) 2×1 Wilkinson combiner transmission test pattern. Dimensions: (a) and (b) 3.0 mm × 1.0 mm, (c) and (d) 1.8 mm × 0.5 mm

The fabrication process is similar to the one used for the first generation circuits. The completed circuits are shown in Figure 5.17.

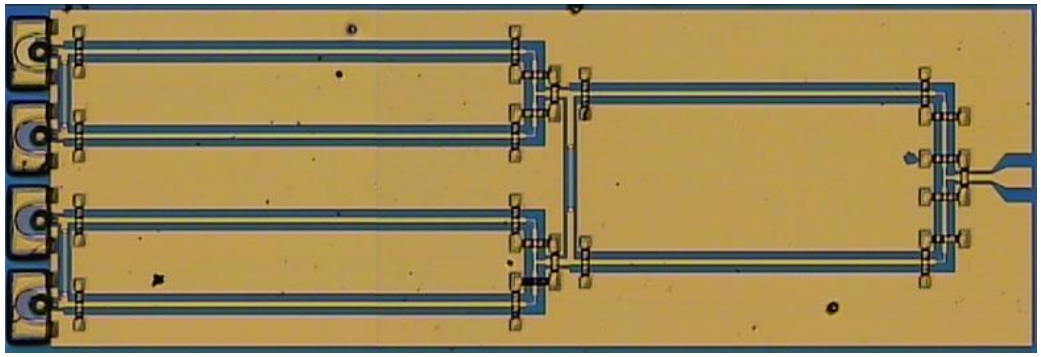

(a)

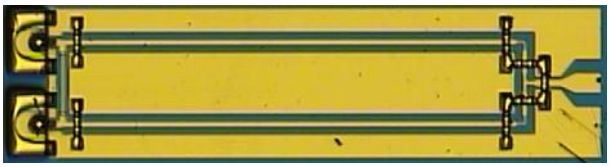

(b)

Figure 5.17 Pictures of completed (a) 4×1 Wilkinson power combiner and 4-element photodiode array and (b) 2×1 Wilkinson power combiner and 2-element photodiode array.

5.3.2 S-parameter measurements

The S-parameters of both 4×1 and 2×1 Wilkinson power combiners were measured using the HP8510C VNA and results are shown in Figure 5.18. Calibration was carried out using the on-wafer TRL method. We can see that matching and isolation bandwidths are much wider than those of the first-generation circuits. This is expected since no tuning stubs were incorporated for the second-generation circuits. The insertion loss can be determined from the S12 transmission data. Note that there are 6 dB and 3 dB of built-in “splitting loss” for

the 4×1 and 2×1 Wilkinson power combiners, due to the way that S-parameters are defined. By subtracting those losses from the S12 data, the insertion losses for the 4×1 and 2×1 Wilkinson power combiner were found to be 2.0 dB and 1.0 dB, respectively. The attenuation determined from straight transmission lines on the same wafer is ~ 0.55 dB/mm, which amounts to 1.7 dB and 1.1 dB insertion loss for the 4×1 and 2×1 Wilkinson power combiners, respectively. The insertion losses estimated from these two methods agree well.

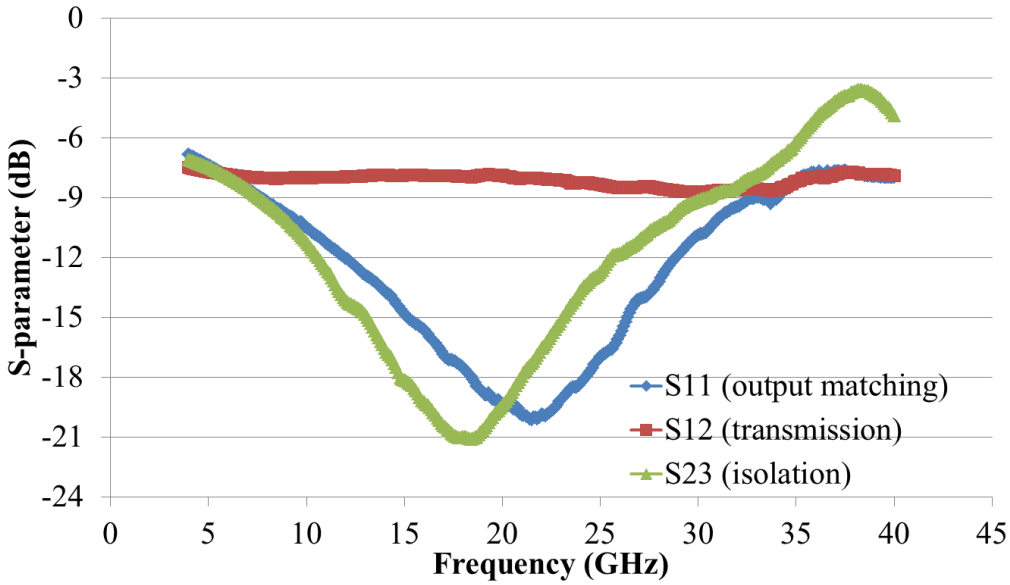

(a)

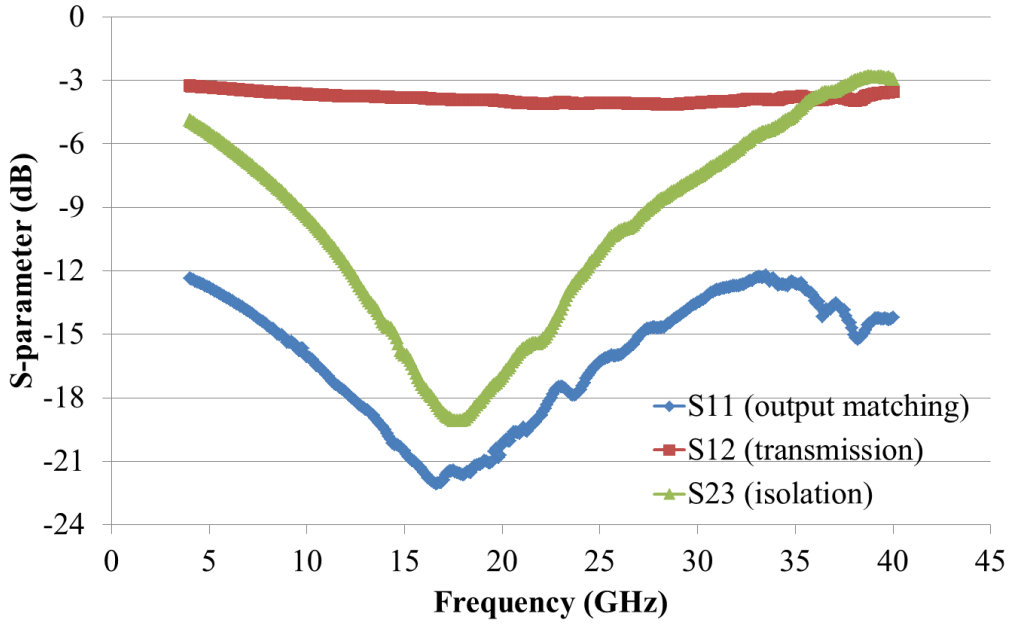

(b)

Figure 5.18 The measured S-parameters of the (a) 4×1 Wilkinson power combiner and (b) 2×1 Wilkinson power combiner

5.3.3 Bandwidth and linearity measurements

The frequency response of the integrated photodiode array-Wilkinson power combiner was measured using the two-laser heterodyne setup shown in Figure 5.9. When testing the 4×1 Wilkinson combiner and photodiode array, four sets of optical delay lines and attenuators were used, as well as a 4-element lensed fiber array.

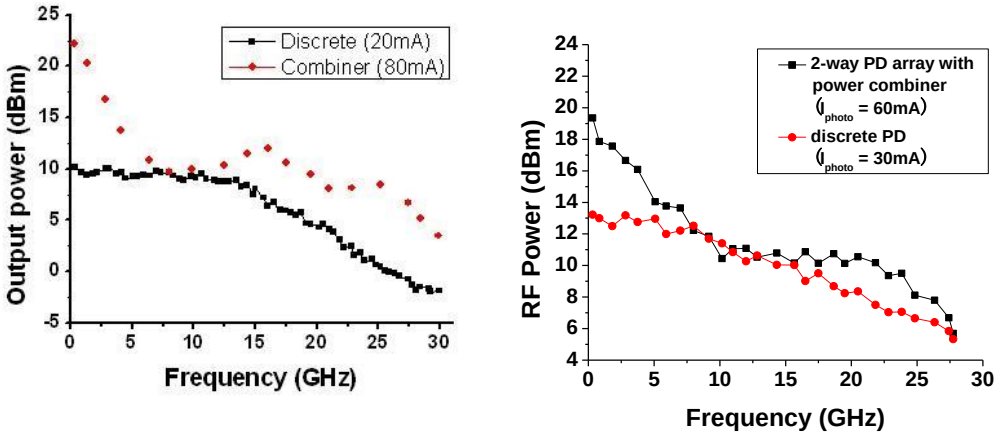

(a) (b)

Figure 5.19 The frequency responses of (a) 4×1 Wilkinson power combiner and 4-element photodiode array and (b) 2×1 Wilkinson power combiner and 2-element photodiode array. The bias voltage was -5 V for both measurements.

The measured frequency responses are shown in Figure 5.19. The insertion loss for the 2x1 combiner circuit is approximately 0.7 dB at 20 GHz and 1.5 dB for the 4x1 combiner circuit. This is consistent with the measurement results presented in the previous section. We can see the "current combining" effect (12 dB gain for the 4×1 combiner and 6 dB gain for the 2×1 combiner) at very low frequency. The two separate peaks and the larger than 6 dB gain near 25 GHz in the frequency response of the 4×1 combiner circuit are indications of a resonance effect, e.g. the resonance between stages of the Wilkinson combiner. The maximum photocurrents were limited by the coupling efficiency of the lensed fiber array.

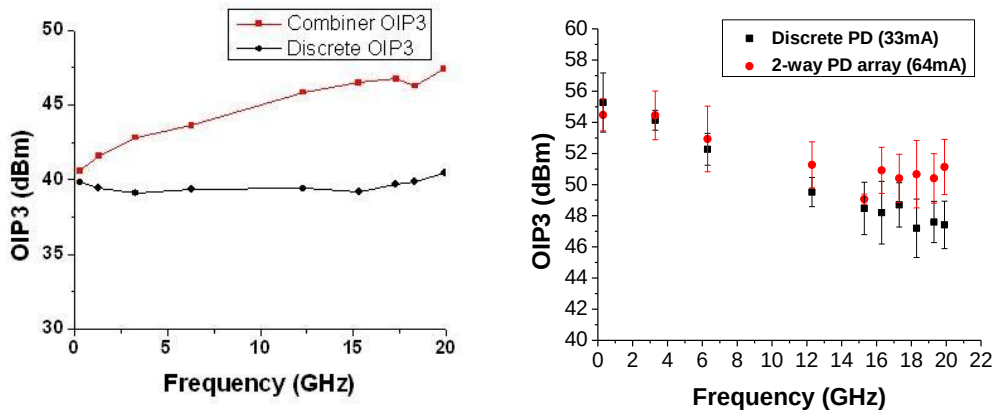

(a) (b)

Figure 5.20 The OIP3 of (a) 4×1 Wilkinson power combiner and 4-element photodiode array and (b) 2×1 Wilkinson power combiner and 2-element photodiode array. The photocurrent used in (a) was 20 mA for discrete photodiode and 80 mA for the combiner. The bias voltage for both measurements was -9 V.

The OIP3 measurement results are shown in Figure 5.20. The OIP3 increases in both cases as a result of the reduced voltage swing on each photodiode in the arrays, compared to that of a discrete photodiode. At low frequencies, the Wilkinson power combiners are electrically short and the voltage swing across the photodiode, V_{PD}, is the same as that across the load, V_{Load}. As the frequency increases, the ratio of V_{PD}/V_{Load} decreases due to the isolation effect of the Wilkinson power combiner, thus resulting in higher OIP3 values.

5.4 Summary

In this chapter, I first demonstrated effective power combining and enhanced linearity performance using a monolithically integrated 2×1 Wilkinson

power combiner and 2-element HD-PDA photodiode array. The influence of an open-stub tuning circuit on photodiode performance was also studied. The OIP3 improvement of the tuning stub circuit can be well explained by the responsively change caused by the voltage swing on the photodiodes. I expanded the study to include 4×1 Wilkinson combiners and HD-MUTC photodiode arrays in order to achieve higher output power and improved linearity. A 6 dB OIP3 improvement has been shown with the 4×1 combiner circuit and the 2×1 combiner circuit reaches over 50 dBm OIP3 at 20 GHz.

Chapter 6 Characterizing and Modeling MUTC Photodiode Nonlinearity

6.1 Introduction

Various measurement-based models have been developed to explain photodiode nonlinearities [71, 102, 103], mostly in terms of voltage-dependent responsivity. However, there are few studies on the physical effects that cause nonlinear phenomena in the PDs that employ the UTC concept. A. Hastings et al. reported that the nonlinear distortion in partially-depleted-absorber (PDA) PDs is related to the Franz-Keldysh Effect (FKE) and impact-ionization in the depleted InGaAs absorber [104]. The voltage-dependent responsivity has been identified as the primary mechanism that determines PD nonlinearities at low frequencies. As the frequency increases, the nonlinear capacitance starts to dominate PD nonlinearities [71]. The goal of this chapter is to develop a physics-based model to explain intermodulation distortions in MUTC photodiodes at low frequencies.

InGaAs, p+, C, $2x10^{19}$, 50nm
InP, p+, Be, $8x10^{18}$, 100nm
InGaAs, C, $8x10^{19}$ – $5x10^{18}$, 650 nm
InGaAs, n.i.d, <$5x10^{15}$, 300nm
InGaAs/InAlAs chirped superlattice, n.i.d. <$5.0x10^{15}$, 24nm
InP, Si, $5x10^{16}$, 5nm
InP, n.i.d, <$5x10^{15}$, 400nm
InP, n+, Si, $3.0x10^{19}$, 1000nm
InP, semi-insulating substrate

Figure 6.1 The epitaxial layer structure of an HD-MUTC photodiode

I used the MUTC photodiode with heavily doped absorber (HD-MUTC) [71] for this study. It has been previously described in Chapter 5 and its epitaxial structure is shown again in Figure 6.1. The device is a mesa structure with back-illumination. The 3dB bandwidth for devices with 40-µm diameter active area is 13 GHz at -6 V bias. No active cooling was used during the measurements.

6.2 Responsivity and OIP3 measurements

The responsivity of the 40 µm-diameter PD was measured at the wavelength of 1543 nm and different bias voltages. The results are shown in Figure 6.2. The responsivity increases at larger photocurrent and bias voltage due to InGaAs bandgap reduction at higher temperatures and improved carrier collection efficiency. The responsivity data were then used to determine fitting

parameters in the model.

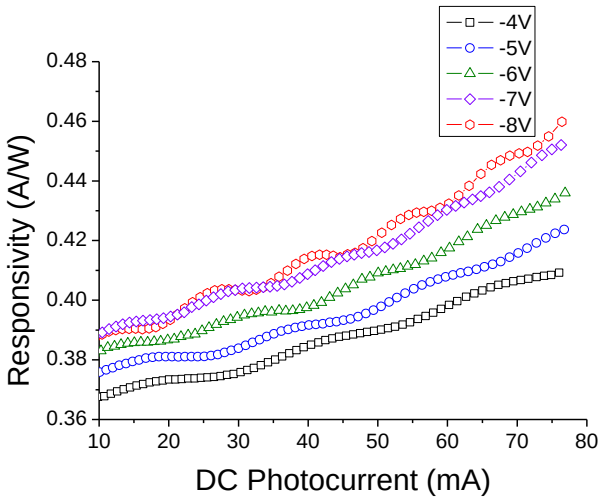

Figure 6.2 Responsivity's dependence on DC photocurrent and bias voltage of a 40-µm diameter HD-MUTC photodiode

The OIP3 was measured using the 3-tone intermodulation distortion setup described in Chapter 2. The wavelengths of the three carrier tones were 1542 nm, 1543 nm and 1544 nm. The fundamental modulation frequencies were f_1 = 300.7 MHz, f_2 = 311.1 MHz and f_3 = 320.7 MHz, respectively. It is worth mentioning that the third-order intermodulation distortion products (IMD_3) are the largest among the in-band distortion products (IMD_3, IMD_5, IMD_7…) for all measured photocurrent / bias voltage / modulation depth conditions. It follows that it is appropriate to use OIP3 as the figure of merit for characterizing nonlinearities.

The measurement results are shown in Figure 6.3. The OIP3 curve at a given bias voltage exhibits two peaks as the photocurrent increases from 10 mA to 80 mA. Similar peaking behavior or OIP3 'sweet spots' have been observed in

other photodiodes [82] and RF amplifiers [76, 105]. Pan et al. have previously reported the presence of the first OIP3 peak [71]. The observation of the second peak provides the potential for larger RF power output while maintaining high linearity performance. When the reverse bias voltage is increased, the positions of the OIP3 peaks shift toward larger photocurrent and the OIP3 values between the two peaks, i.e. the 'valleys', become higher.

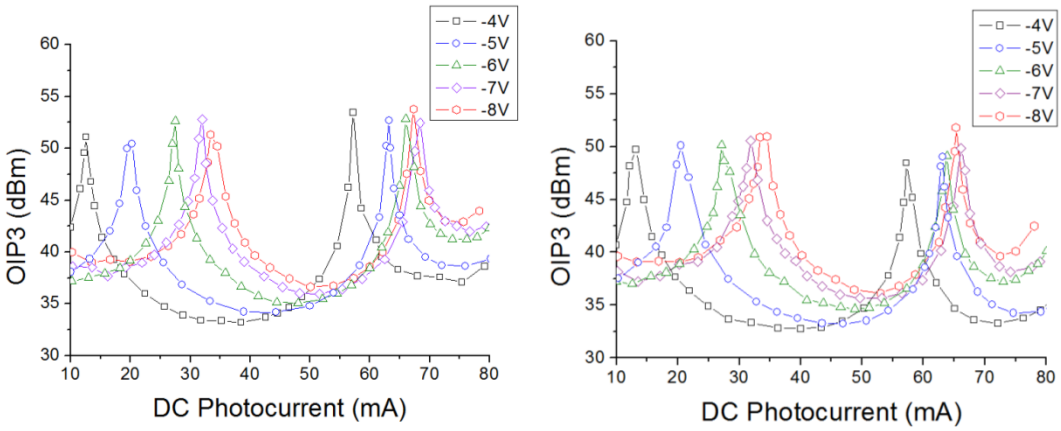

Figure 6.3 Dependence of OIP3 on DC photocurrent and bias voltage. (a) 80% modulation depth and (b) 25% modulation depth

The OIP3 curves measured at different signal modulation depth are almost the same for photocurrents smaller than 50 mA. The difference between OIP3 measured at large and small signal modulation depth becomes more pronounced with larger photocurrent. This suggests the presence of large-signal nonlinear effects such as expansion and saturation, which are usually observed in microwave devices including photodiodes [35, 40] and power amplifiers [76, 77, 105]. The combination of high photocurrent level and high modulation depth can

drive the photodiode into saturation and thus generate the large-signal nonlinearity, which is dependent on both the quiescent point and RF signal amplitude, whereas the small-signal nonlinearity is only determined by the quiescent point [105].

6.3 Nonlinear mechanisms in the MUTC photodiode

The refractive indices of the InP and InGaAs layers are affected by electric field, carrier density, and temperature changes in the PD. This can influence absorption in the InGaAs region and give rise to nonlinearity. However, for the photodiodes studied here the changes in the electric field strength and carrier density are too small to produce a significant refractive index change [47, 106]. Temperature-induced refractive index changes are too slow to produce the intermodulation distortions observed for the MUTC photodiodes because the fundamental frequencies are too high. Hence the model described in this paper does not include nonlinear mechanisms from these effects.

The band edges of a semiconductor are tilted when there is a strong electric field present. The wavefunctions for electrons and holes penetrate into the bandgap, which alters the probabilities for direct transitions involving energies

above the bandgap and photon-assisted tunneling below the bandgap. The absorption coefficient near the bandgap energy is thus dependent on the applied electric field. This is the Franz-Keldysh effect [107, 108]. It has been suggested as one of the key nonlinear mechanisms in MUTC and PDA PDs [71, 103, 104] and is a primary focus of this study. The impact-ionization effect in the InGaAs absorber is also included in the model. Neither the nonlinear stored charge nor the carrier transit time are considered in the model since the analysis and measurements are confined to the low frequency range near 300 MHz. Large-signal effects such as expansion and saturation are not included.

6.4 The nonlinear model

6.4.1 Electric field calculation

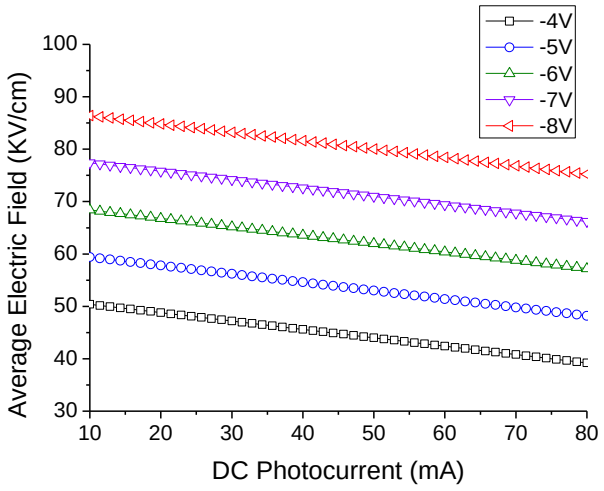

Figure 6.4 The average electric field in the InGaAs absorber at different bias voltages and photocurrent levels.

The electric field strength in the depleted InGaAs absorber is calculated using Crosslight APSYS. Linear fitting of the average electric field is used in the model for simplicity and is shown in Figure 6.4.

6.4.2 Franz-Keldysh effect

To model the Franz-Keldysh effect I used equations developed by Callaway [107]and Lambert [108]. The absorption coefficient is given by

$$\alpha = \alpha_1 + \alpha_2$$

$$\alpha_{1,2} = \pi\varphi\hbar \frac{2\mu\beta^{\frac{1}{3}}}{\left[(2\mu_1)^{\frac{3}{2}} + (2\mu_2)^{\frac{3}{2}}\right]} \times \left[\left(\frac{dAi(y)}{dy}\right)^2_{y_0} - y_0 Ai^2(y_0)\right] \tag{6.1}$$

Where the parameters are defined as

$$\beta = \frac{2\mu F}{\hbar^2}$$
$$\frac{1}{\mu_1} = \frac{1}{m_e^*} + \frac{1}{m_{hh}^*}$$
$$\frac{1}{\mu_2} = \frac{1}{m_e^*} + \frac{1}{m_{lh}^*}$$
$$y_0 = \frac{2\mu}{\hbar^2\beta^{\frac{2}{3}}}\left(E_g - \hbar\omega\right).$$

The total absorption coefficient α is the sum of contributions α_1 from heavy holes and α_2 from light holes; Ai(y) is the Airy function of the first kind; F is the electric force strength; and μ is the reduced mass of electrons and holes. The temperature dependence of the bandgap energy is adopted from [109] and φ is a fitting parameter that can be estimated from the responsivity measurement. The values of the parameters used in the model are listed in Table 6.1.

	Value	Unit	Meaning and Reference
m_0	9.1×10^{-31}	Kg	electron mass
m_e^*	$0.041m_0$	Kg	effective mass of electron [110]
m_{hh}^*	$0.43m_0$	Kg	effective mass of heavy hole [111]

m_{lh}^*	$0.04m_0$	Kg	effective mass of light hole [110]
E_g	0.74	eV	bandgap of $In_{0.53}Ga_{0.47}As$ at 300K [109, 110]
φ	1.48×10^4	$cm^{-1}eV^{-\frac{1}{2}}$	fitting parameter

Table 6.1 Values of model parameters

6.4.3 Impact ionization

The model adopts the impact-ionization data for $In_{0.53}Ga_{0.47}As$ obtained by Ng et al. [112] since it specifically addresses the low field scenario. Only electron impact-ionization is considered since α, the electron ionization coefficient, is at least an order of magnitude larger than the hole ionization coefficient, β, in $In_{0.53}Ga_{0.47}As$. The electron ionization coefficient is can be expressed as

$$\boldsymbol{\alpha(E) = 2.03 \times 10^3 \exp\left(-\left(\frac{1.98 \times 10^5}{E}\right)^{1.05}\right), \qquad E < 150\frac{kV}{cm}.} \quad (6.2)$$

6.4.4 Device temperature

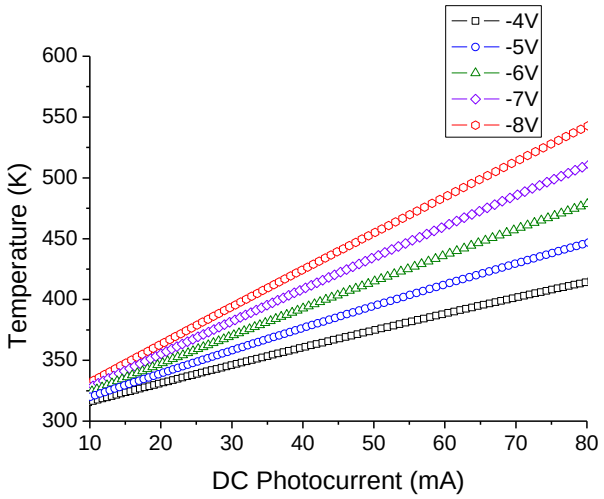

Figure 6.5 Estimated device temperature at different bias voltages and photocurrent levels.

The device temperature model is adapted from previous thermal analysis reported in Refs. [69] and [28]. Relative to these curves slight adjustments to the internal temperature are made for both responsivity and OIP3 simulation, i.e., the internal temperature of the device is a fitting parameter with initial values selected using previously reported measurements for specific values of the DC photocurrent. In Figure 6.5 the internal temperature is plotted versus DC photocurrent for bias voltage in the range 4 V to 8 V.

6.4.5 Coupling of physical effects in the photodiode

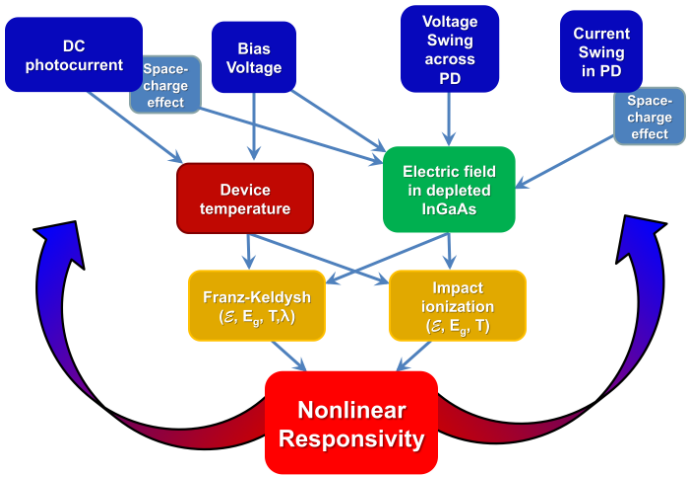

Figure 6.6 Block diagram of physical effects that contribute to nonlinearities at low frequencies (300MHz).

The coupled physical effects that contribute to nonlinearities at low frequencies (300MHz) are shown in Figure 6.4. The DC photocurrent through the space-charge effect and the DC bias both affect the device temperature and the electric field in the depleted InGaAs absorber. The AC photocurrent and voltage swing across the photodiode alter the electric field profile. The temperature and the internal electric field strongly influence impact ionization and the Franz-Keldysh effect, which, in turn, give rise to the nonlinear responsivity. Changes in the responsivity feed back to the DC photocurrent, electric field, and AC voltage and photocurrent.

Nonlinear responsivity has been previously interpreted in terms of voltage

dependence and current dependence [71, 81]. However, the electric field dependent responsivity is a better descriptor of the nonlinear mechanisms since the changing electric field in the depleted InGaAs absorber is the root cause of nonlinearities at low frequencies.

6.4.6 Simulation procedure

For each bias voltage and average optical power, the quiescent point is first calculated for the PD by solving the responsivity and temperature equations simultaneously. The simulation process is frequency-independent since no capacitance effect is included in the model. The fundamental frequencies are chosen in such a way that the IMD products do not overlap in frequency. Next the response for the 3-tone stimuli is solved for progressive temporal steps with the PD biased at the quiescent point. Fast Fourier Transform (FFT) is used to obtain the output frequency spectrum from which the OIP3 is calculated. The simplified flowchart of the simulation program is shown in Figure 6.7.

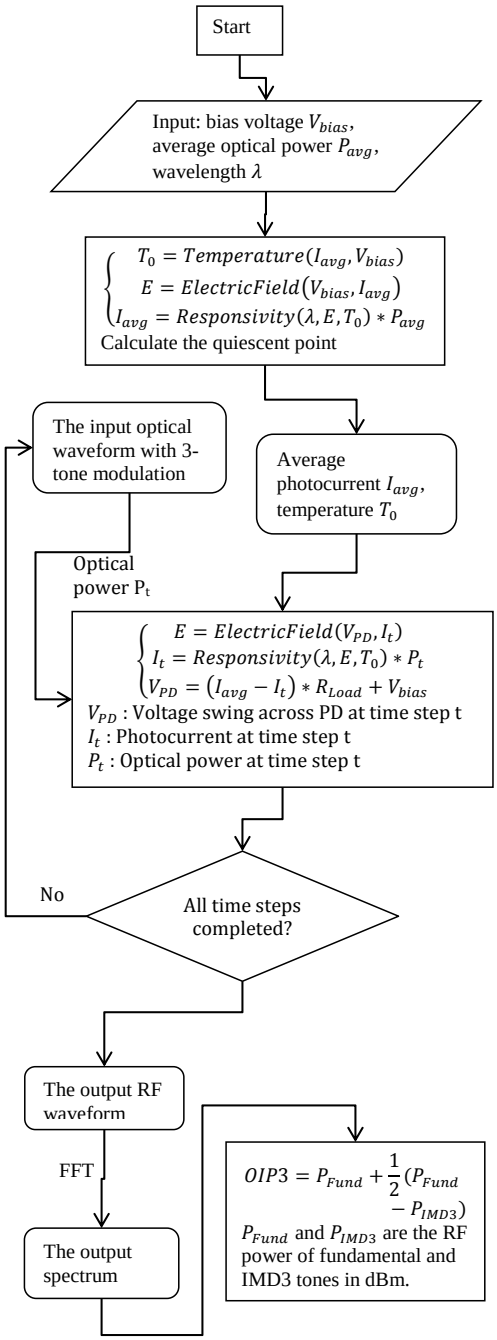

Figure 6.7 Simplified flowchart of the simulation program

6.5 Simulation results and discussion

6.5.1 Responsivity versus wavelength

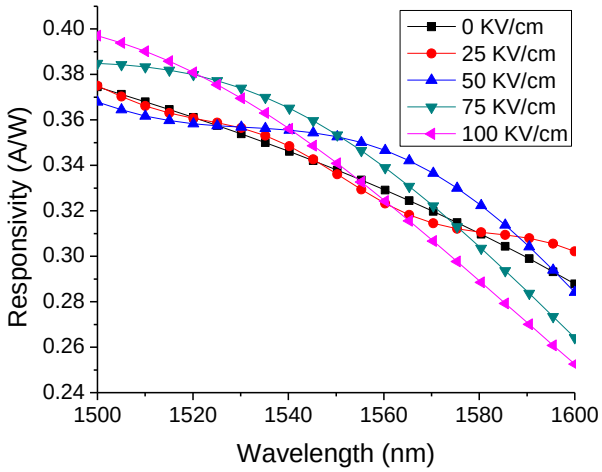

Figure 6.8 Simulated wavelength and electric field dependence of responsivity at 300K.

The wavelength and electric field dependence of the responsivity were simulated from 1500 nm to 1600 nm and are shown in Figure 6.8. The effect of electric-field-dependent responsivity can be clearly seen at each wavelength.

6.5.2 Responsivity versus electric field

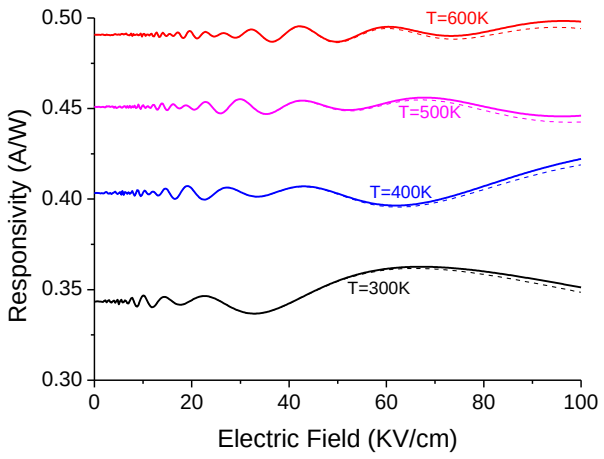

Figure 6.9 Simulated responsivity versus electric field in the depleted InGaAs absorber. (solid lines: with impact-ionization, dashed lines: without impact-ionization)

The responsivity as a function of the electric field in the depleted InGaAs absorber was simulated at 1543 nm. The results are plotted in Figure 6.9. The oscillation in responsivity is caused by the Franz-Keldysh effect. This is the primary source of nonlinear distortions in the MUTC PD at low frequencies. A few percent of change in the first order transfer function (responsivity) is enough to induce significant difference in higher order intermodulation distortion products [40, 71, 103, 113]. For small-signal nonlinearities, a more generalized argument can be made that the linearity (OIP3) curve is closely related to high order derivatives of the transfer function. The intermodulation distortion products approach zero (indefinite OIP3 value) where the derivatives of transfer function change signs (zero-crossing point). This relationship has been widely observed in

the nonlinear analysis of RF amplifiers [76, 77, 105, 114].

The solid lines in Figure 6.9 include impact ionization and the dashed lines were calculated without impact ionization. It is clear that the contribution from impact-ionization is negligible in the electric field range where the PD operates. However, the temperature strongly affects the quiescent point of the PD.

6.5.3 Responsivity versus photocurrent

The variation of the responsivity with photocurrent under different bias voltages was simulated at 1543 nm (Figure 6.10). The fitting parameter, φ, in the model was extracted from these curves.

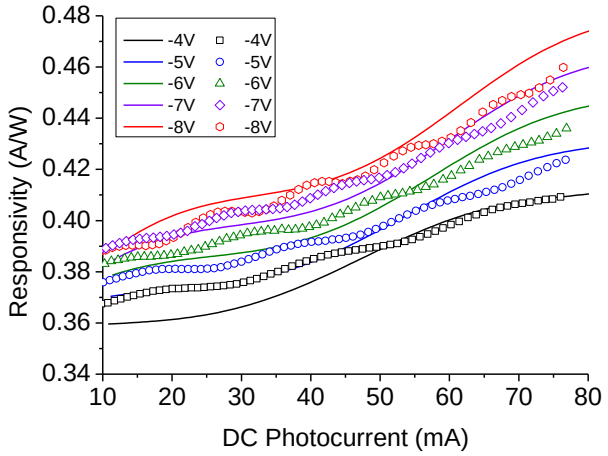

Figure 6.10 Responsivity versus DC photocurrent under different bias voltages. (solid line: simulation, scattered: measurement)

6.5.4 OIP3 versus photocurrent

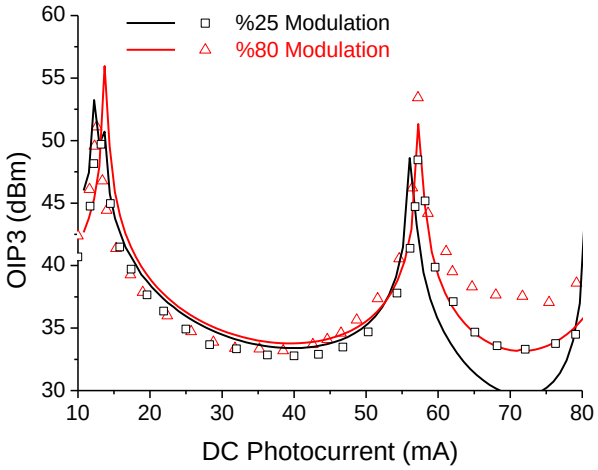

Figure 6.11 OIP3 versus DC photocurrent at -4V (solid line: simulation, scattered: measurement)

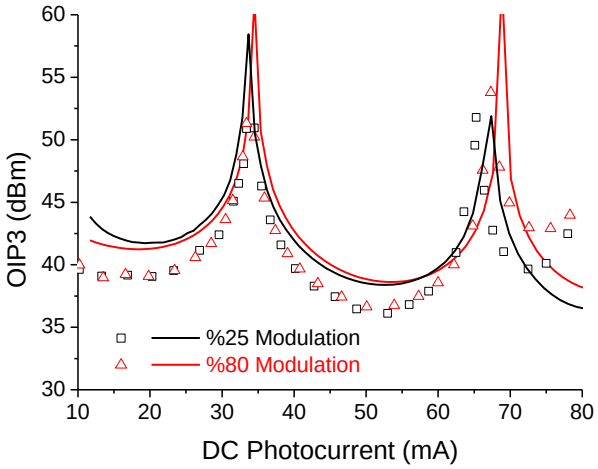

Figure 6.12 OIP3 versus photocurrent at -8V (solid line: simulation, scattered: measurement)

Figure 6.11 and Figure 6.12 show the simulated dependence of OIP3 on photocurrent for -4V and -8V bias voltages at 1543 nm. Stimuli with both large (80%) and small (25%) signal modulation depth were used in the simulations. Comparisons of simulated and measured OIP3 at other bias voltages are not shown because the graphs become too cluttered.

The simulated OIP3 curves show good agreement with measurements. The quasiperiodic appearance of OIP3 peaks can be viewed as the result of the oscillating nature of the Franz-Keldysh effect. The fact that the OIP3 peak can be tuned with bias voltage may be beneficial in optimizing the PD linearity performance.

6.6 IMD phase measurement and discussion

Only the magnitudes of IMDs can be obtained from conventional two-tone and three-tone measurements for nonlinearity characterization. Knowledge of the IMD phase information will aid understanding of the nonlinear distortion phenomenon, as well as facilitate the development of linearization techniques [6, 115]. While several techniques exist to measure IMD phase for RF amplifiers [116, 117], there are no reports on the phase of IMDs in photodiodes in the published literature.

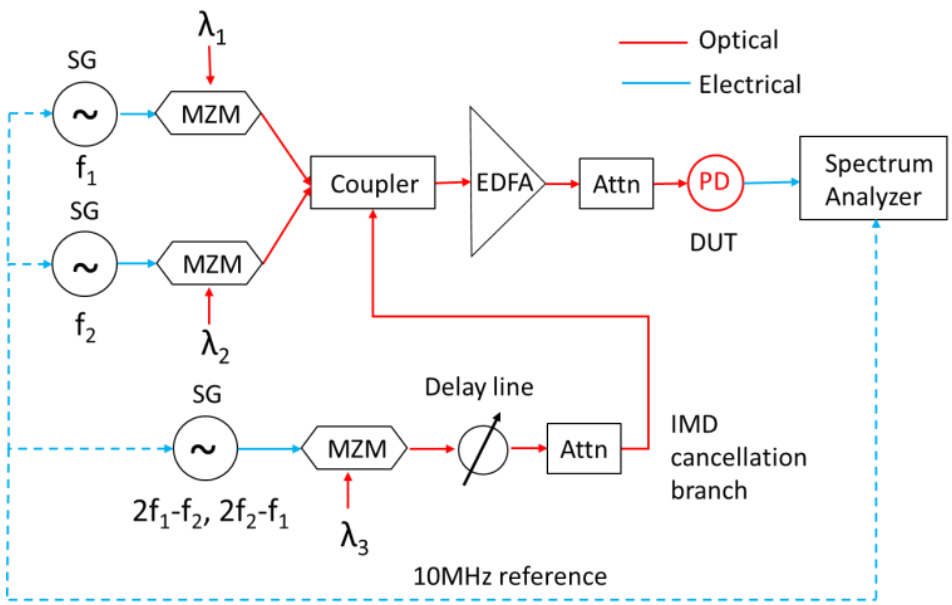

Figure 6.13 The IMD phase measurement setup

I designed the IMD phase measurement setup, which is shown in Figure 6.13. It consists of a conventional two-tone setup and an additional "IMD cancellation" branch. The light sources are three DFB lasers at the wavelengths of 1544nm, 1545nm and 1546 nm. The three signal generators and the spectrum analyzer share a common 10 MHz reference frequency. The signal generator in the IMD cancellation branch is set at the frequency of the IMD tone being measured. The phase and magnitude of the signal in this branch are controlled by a tunable optical delay line and an attenuator. The RF output from the photodiode is directed into the spectrum analyzer through AC coupling.

The IMD magnitude is determined the same way as for a two-tone setup while the light signal in the third branch is blocked. The phase measurement is

accomplished through cancellation of the IMD tone in the output spectrum of the photodiode by adjusting the phase and magnitude of the signal in the "IMD cancellation" branch. The power level of the signal generators and EDFA are kept constant during measurements to avoid introducing extraneous phase shifts. The frequencies of the fundamental tones (f_1, f_2) were 3.3111 GHz and 3.3207 GHz. A constant modulation depth of 55% was maintained during the test.

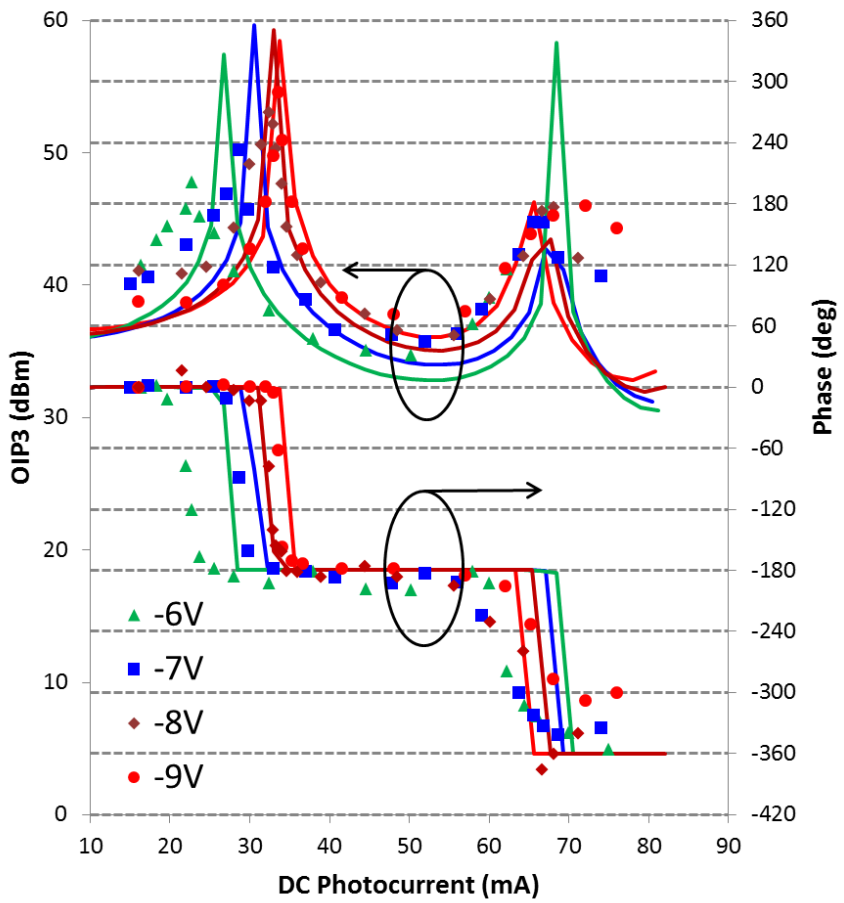

Figure 6.14 The measured OIP3 and relative phase of the upper IMD3 product (IMD3U) for MUTC photodiode at different dc photocurrents and bias voltages.

Both measurement and simulation for OIP3 and IMD3 phase are shown in

Figure 6.14. Only the results for the upper IMD3 product (IMD3U) are included for sake of clarity. The nonlinearity model fully explains the variation of OIP3 with photocurrent and bias voltage.

The most striking feature in the IMD3 phase plot is the existence of 180 degree transitions at the photocurrent levels where OIP3 peaks, although the second transition at larger photocurrent is not as well defined as the first one. The 180 degree phase changes can be attributed to the sign change of the third-order nonlinear coefficient. The more gradual phase transition near the second OIP3 peak may indicate competing nonlinearities with different phase characteristics instead of a single dominate mechanism. Photodiode linearity can be improved by taking advantage of these phase changes. For example, multiple photodiodes could be biased at appropriate photocurrents and voltages and combining their outputs so that the IMD3 products cancel each other.

6.7 Summary

In this chapter, I have systematically characterized the third-order intermodulation distortion phenomenon in the HD-MUTC photodiode and developed a physics-based model to explain the IMD3 characteristics at low frequencies (<3 GHz). The electric-field-dependent responsivity caused by the Franz-Keldysh effect in the depleted InGaAs absorber has been identified as the

primary contributor to intermodulation distortions. The simulation results agree well with measurement data. I have also built an experimental setup to measure the relative phase of IMDs. I discovered a unique 180-degree phase transitions near the OIP3 peaks. This provides further confirmation for the model since it predicts the IMD phase equally well. The knowledge gained on nonlinear distortions in the MUTC-photodiode is very useful in optimizing photodiode performance. One such example is presented in Chapter 8.

Chapter 7 High-Power Photodiode for Ultra-Low Phase Noise Microwave Signal Generation

7.1 Introduction

As we have discussed in Chapter 1, photonic technology provides unique benefits for generating low phase noise microwave signals since optical cavities have much higher Q values than their electrical counterparts [21, 37]. High fidelity photo-detection is essential to transfer the frequency stability from the optical domain into the electrical domain [118-122].

Two of the fundamental noise sources are the thermal (Johnson) noise and shot noise. The voltage variance caused by thermal noise in 1-Hz bandwidth is given by

$$\overline{V_n^2} = 4k_B TR\ [V^2] \tag{7.1}$$

where T is the temperature (300K), k_B is the Boltzmann constant and R is the resistance. The single-sideband (SSB) phase noise introduced by thermal noise in

the photo-detection process can be expressed as [118]

$$\boldsymbol{L(f) = 10log\frac{k_BT}{2P_0}} \approx \boldsymbol{-177 - 10log[P_0]\ [dBc/Hz]} \tag{7.2}$$

where P_0 is the power delivered to the load resistor in units of mW. The current variance caused by shot noise in a 1-Hz bandwidth is given by

$$\overline{I_n^2} = 2eI_s\ [A^2] \tag{7.3}$$

where e is the electron charge and I_s is the average photocurrent. The SSB phase noise introduced by shot noise can be expressed as [118]

$$\boldsymbol{L(f) = 10log\frac{eI_sR}{4P_0}} \approx \boldsymbol{-177 + 10log\frac{I_s}{P_0}\ [dBc/Hz]} \tag{7.4}$$

Combining eqn. **(7.2)** and eqn. **.(7.4)** yields the following equation which describes the contributions from thermal and shot noise [118].

$$\boldsymbol{L(f) = 10log\frac{eI_sR + 2k_BT}{4P_0}\ [dBc/Hz]} \tag{7.5}$$

Before the photodiode enters the saturation region, the power delivered to the load, P_0, is proportional to I_s^2. Therefore the thermal-noise-limited phase noise floor improves at a rate of 20 dB/decade with increasing photocurrent, while the shot noise limited floor improves with 10 dB/decade rate. The shot noise tends to dominate the total phase noise when the photocurrent is larger than 1 mA at 300K.

Another major phase noise source in the photo-detection process is the amplitude-to-phase (AM/PM) conversion or power-to-phase conversion (ppc)

[118-122]. The AM noise or relative intensity noise (RIN) in the optical signal can be converted into electrical PM noise by the photo-detector. The figure of merit, $\alpha_{AM/PM}$, that is used to characterize this phenomenon and defined as [121]

$$\boldsymbol{\alpha_{AM/PM} = \frac{\Delta\varphi}{\Delta P/P}} \tag{7.6}$$

where the $\Delta P/P$ is the percentage of amplitude change, and $\Delta\varphi$ is the corresponding phase change. The AM/PM conversion is closely related to nonlinear distortions in the photodetector [76] and is determined primarily by the photo-detector design and operation parameters such as photocurrent and bias voltage. Depending on the operating condition, the phase noise contribution from AM/PM conversion can be much greater than from thermal and shot noise.

7.2 Initial measurements at NIST

Dr. Scott Diddams' group at NIST has been working on a photonics approach to ultra-low phase noise microwave generation. Their recently developed 10 GHz oscillator based on an optical frequency division method has demonstrated record low phase noise performance [37]. A schematic diagram of the optical frequency division method is shown in Figure 7.1. The optical pulse train produced by the frequency comb is converted into electrical pulse train by the photodiode and the 10 GHz signal is selected using a band-pass filter (BPF),

as shown Figure 7.2. Comparisons of phase noise performances for leading 10 GHz oscillators are shown in Figure 7.3.

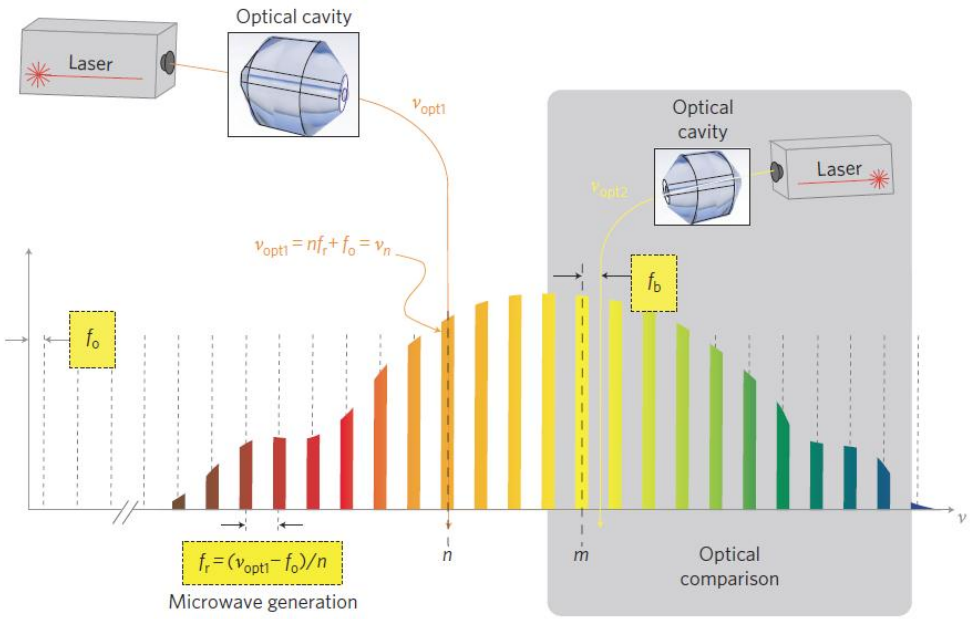

Figure 7.1 Optical frequency division for low phase noise microwave generation [37]

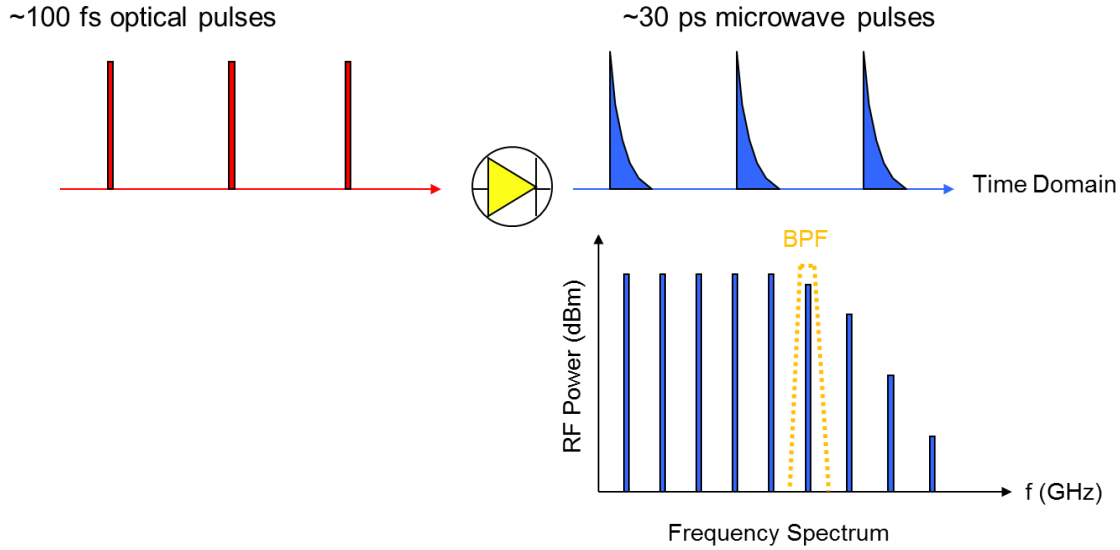

Figure 7.2 Time domain waveform and frequency spectrum of the oscillator

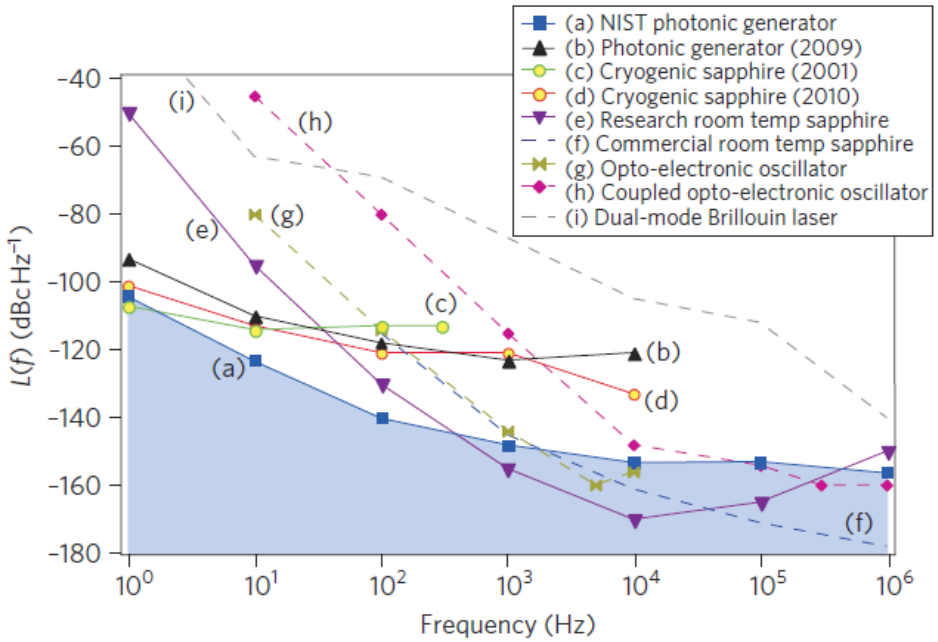

Figure 7.3 SSB phase noise comparison of leading microwave oscillators in the 10 GHz range [37]

Further improvement of the NIST oscillator phase noise performance is limited by the power handling capability and linearity of the photodiode used in the system. The high-power MUTC photodiode developed by our group holds great potential in this application. Dr. Diddams' group and our group launched a joint research project to investigate the MUTC photodiode performance in the pulse mode and its application in the 10 GHz low phase noise oscillator.

I measured the impulse response of MUTC-4 photodiodes together with Dr. Diddams' students at NIST. The light source was an Erbium-doped fiber laser at 1.55-µm wavelength. The pulse width is less than 100 fs and repetition rate is 250 MHz. The light was coupled into the back-illuminated photodiode using a

lensed fiber. The electrical pulse was recorded using a high-speed sampling oscilloscope and RF power was measured with a 50 GHz spectrum analyzer. The loss and dispersion of the RF cable/attenuator/bias tee assembly was measured using a network analyzer and was taken into account during data analysis.

The impulse response measurement results are shown in Figure 7.4. When the average optical power is less than 2 mW, the peak voltage of the electrical pulse does not change with the bias voltage, which suggests linear operation. The photodiode bias voltage can be completely collapsed by large photocurrent, which causes saturation and a significant increase in the pulse. The time domain waveforms clearly illustrate this phenomenon.

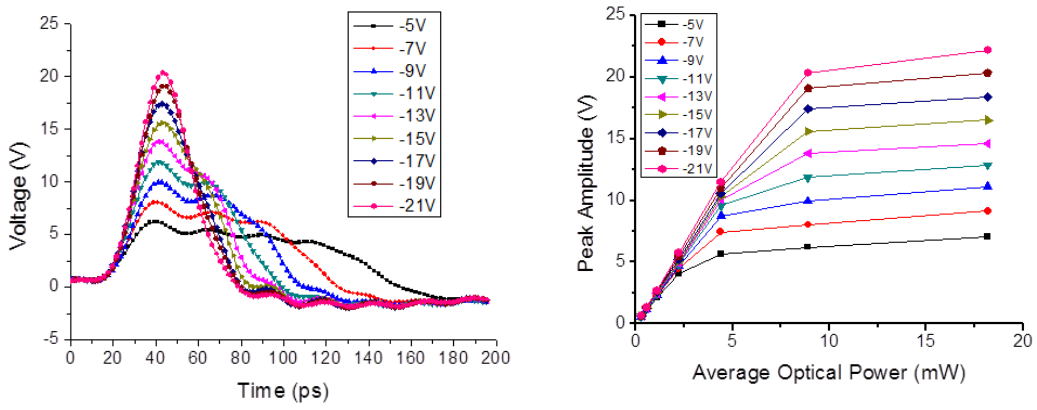

(a) (b)

Figure 7.4 (a) Impulse response of a 34 µm MUTC-4 photodiode at 8.9 mW optical power and (b) corresponding saturation plot

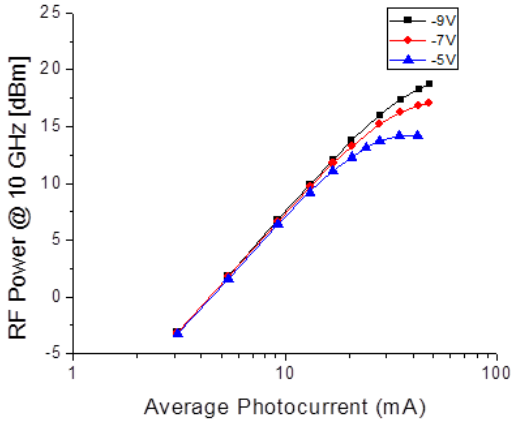

Figure 7.5 RF output power at 10 GHz of a 34-µm MUTC-4 photodiode

Figure 7.5 shows the RF output power measured with a spectrum analyzer. The maximum RF power is 8~10 dB larger than that from the commercial photodiode that NIST previously used in the system.

The AM/PM conversion factor was measured using the phase bridge setup described in [119, 121]. A 20 kHz amplitude modulation was used as the "AM noise" and the resultant "PM noise" was measured at the mixer output. The mixer was biased at the point where it was only sensitive to the phase difference between the input ports rather than amplitude difference.

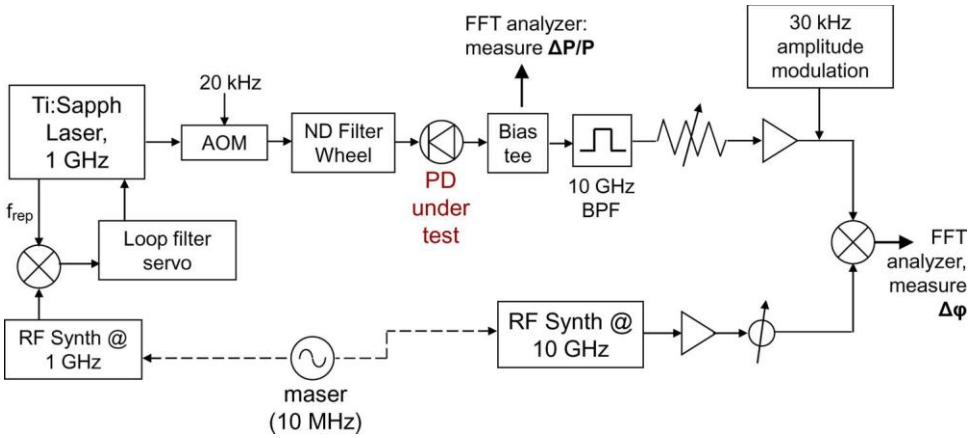

Figure 7.6 The phase bridge setup used to measure the AM/PM conversion factor [37, 121]

The AM/PM conversion measurement results are shown in Figure 7.7. The MUTC photodiode has smaller conversion factor and larger photocurrent range than the commercial photodiodes. Both properties are desirable for low-phase-noise microwave generation.

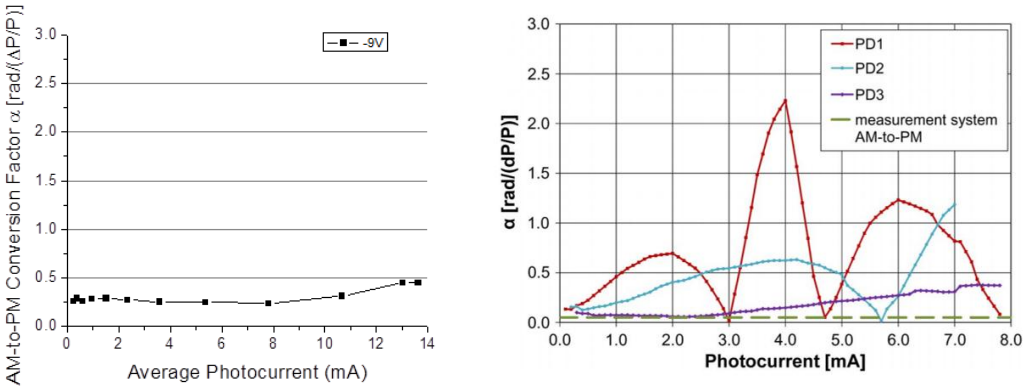

Figure 7.7 AM/PM conversion factors of (a) a 34-µm MUTC-4 photodiode and (b) commercial photodiodes previously used in the system [121]

\

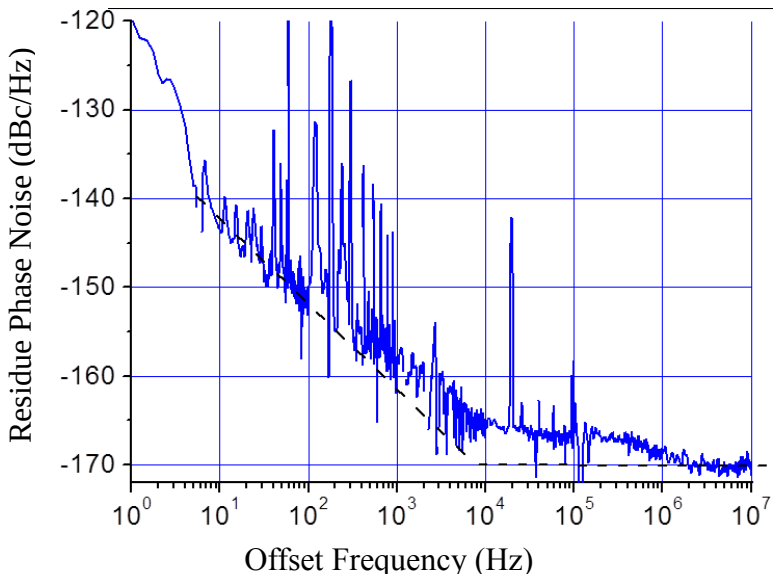

Figure 7.8 The residue phase noise of 34-µm MUTC-4 photodiode at -9 V

The residual phase noise measurement result is shown in Figure 7.8. The noise floor has been reduced to -170 dBc/Hz, which is 10 dB lower than the results achieved by commercial photodiodes.

7.3 Impulse response measurement at UVa

In order to better understand the performance of the MUTC photodiodes in pulse mode operation, I carried out large-signal impulse response measurements at UVa using our fiber pulse laser. The experimental setup was similar to that used in Chapter 4 for small-signal impulse response measurements. The light source was the fiber pulse laser from Toptica Photonics with 100 femtosecond pulse width and 100 MHz repetition rate. No CW laser was used

since there was no need for a DC light offset in this measurement. The response waveform was recorded using a 50 GHz Agilent Infiniium digital sampling oscilloscope. A 25 dB RF attenuation was incorporated in the signal path since a large dynamic range was required in this measurement and the input of the oscilloscope was limited to 0.8 V maximum. The trigger signal was provided by the pulse laser module. The average photocurrent was measured by a Keithley source meter, which also supplied the bias voltage to the photodiode.

Since this was a phase-sensitive measurement, I paid special attention to ensure that phase changes from sources other the photodiode were kept at a minimum. Digital optical attenuators tend to introduce unwanted phase changes while the attenuation is being adjusted. Therefore a simple variable optical attenuator based on a precision blocking screw was used. The amount of attenuation was determined by the percentage of the beam cross-section that was blocked by this attenuator. Various settings on the sampling oscilloscope, such as the scale and voltage offset settings, were found to introduce phase change to the signal as well. Consequently all these settings were kept constant once the measurements started. With the above precautions, signal phase change with constant photodiode bias voltage and photocurrent settings was less than 0.05 degrees at 100 MHz over 4 hours.

MUTC-4 photodiodes with different diameters were studied in this measurement, including 20-μm, 28-μm, 40-μm and 56-μm. Their performance

characteristics under CW and small pulse operation have also been discussed in Chapter 4. The voltage bias was changed from -5 V to -21 V for each photodiode in 4 V steps. The breakdown voltage for the MUTC-4 photodiodes was in the range 26 ~30 V. The device heating was limited due to the low duty cycle of the electrical pulse signals (<0.5%). The average photocurrent was swept from 50 μA to 1 mA in 50 μA steps. The maximum photocurrent was limited by the dynamic range of the sampling oscilloscope and available RF attenuation.

7.3.1 Bandwidth and saturation analysis

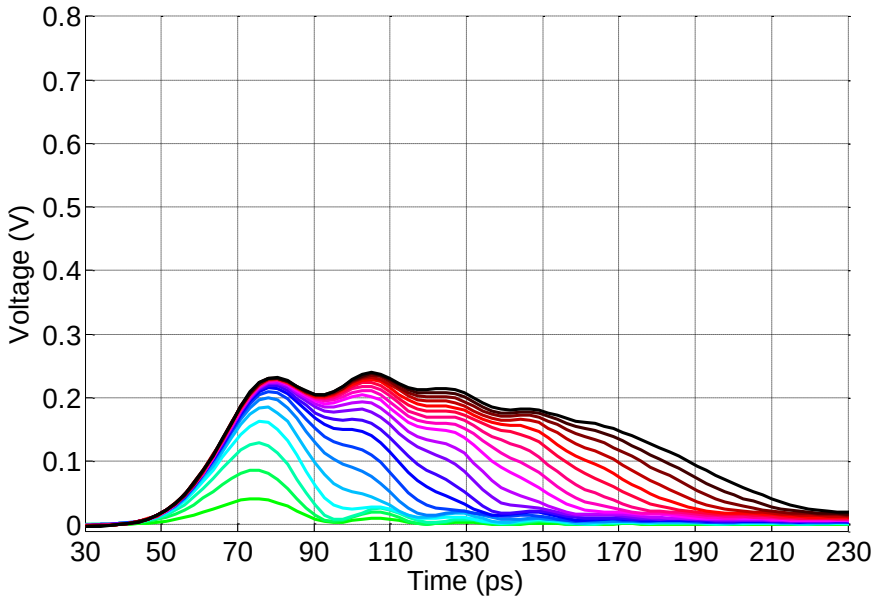

(a)

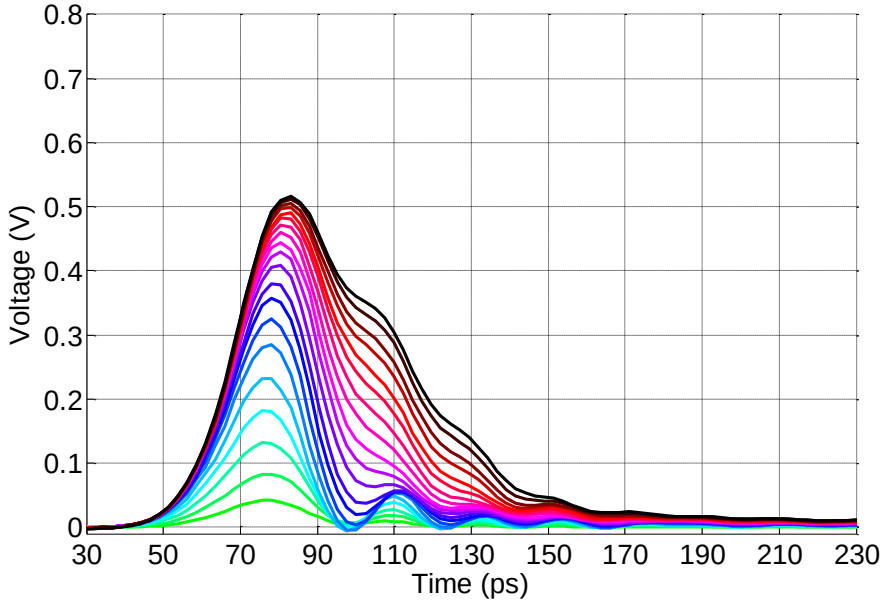

(b)

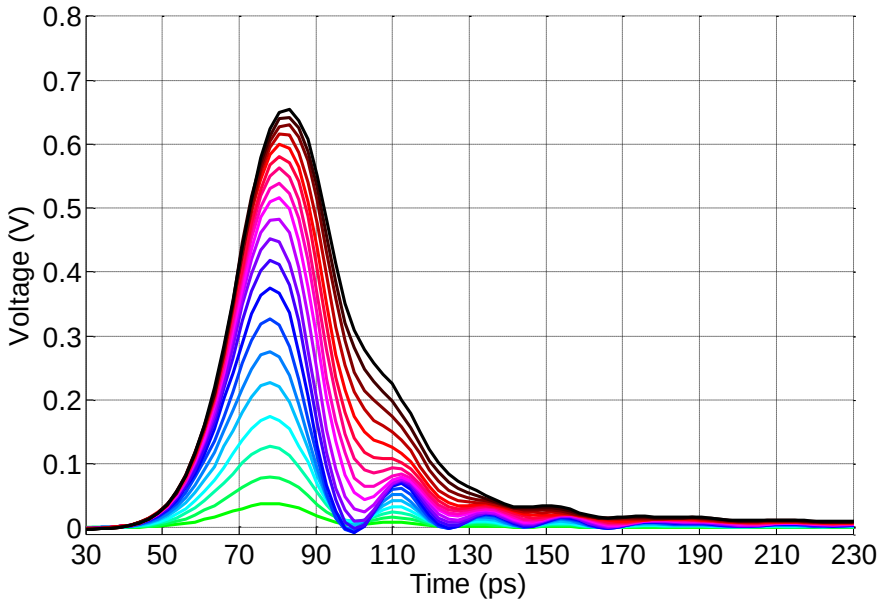

(c)

Figure 7.9 Impulse response waveforms of a 20-µm diameter MUTC-4 photodiode at (a) -5 V, (b) -13 V and (c) -21 V bias voltages. The average photocurrent in each plot is changed from 50 µA (light green) to 1 mA (black) in 50 µA steps. A more intense the color, the larger the average photocurrent.

Examples of impulse response waveforms of a 20-μm diameter MUTC-4 photodiode are shown in Figure 7.9. The bias voltages are -5 V, -13 V and -21 V in (a), (b) and (c), respectively. The average photocurrent in each plot is changed from 50 μA to 1 mA in 50 μA steps. The insertion loss of the RF attenuator and cable assembly is not subtracted from Figure 7.9. The actual voltage waveforms on the photodiode would be ~18 times larger than the values shown above.

We can see that at -5 V, the photodiode saturates early due to the limited bias voltage. The height of the waveform stops growing with increasing photocurrent after it reaches ~0.24 V, which corresponds to 4.3 V on the photodiode. At this point, most of the bias voltage on the photodiode has been screened and the electric field inside the device collapses. After this point, the waveform can only grow in the lateral direction and the pulse width increases almost linearly with average photocurrent. In Figure 7.9 (b) and (c), the photodiode saturation is less severe due to the increased bias voltages. The timing delay of the voltage peaks with increasing photocurrent is also visible in each plot.

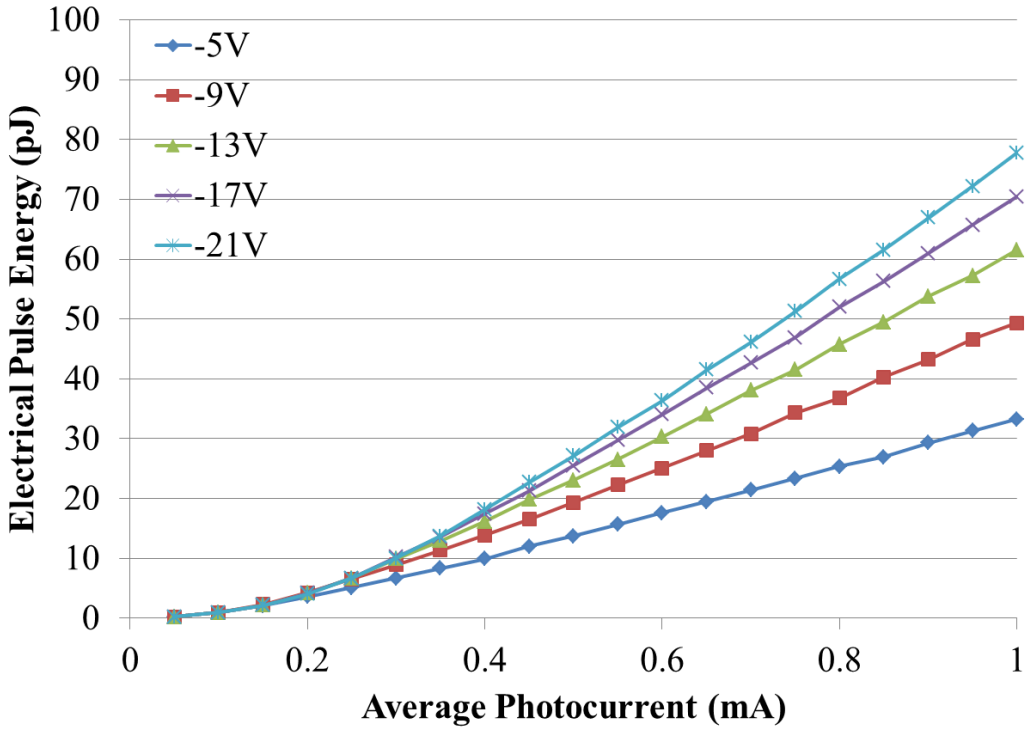

Figure 7.10 The electrical pulse energy of the impulse response of a 20-µm diameter MUTC-4 photodiode at different bias voltages and average photocurrent.

The electrical pulse energy has been calculated by integrating the area underneath the curve using the impulse response waveform approach [122] and the results are shown in Figure 7.10. At small photocurrent (<0.2~0.3 mA), the electrical pulse energy increases proportional to the square of the photocurrent. This is the direct result of the square-law nature of the photo-detection process. At larger photocurrent, the electrical pulse energy scales linearly with photocurrent, which indicates the presence of saturation. This can also be explained using the following equation:

$$E_{pulse} = \int I(t)^2 R_{load} dt = \frac{Q_{pulse}^2}{\Delta t^2} R_{load} \Delta t = Q_{pulse} \frac{Q_{pulse}}{\Delta t} R_{load} \quad (7.7)$$

where E_{pulse} is the electrical pulse energy, $I(t)$ is the photocurrent, R_{load} is the load resistance, Q_{pulse} is the total charge in the pulse, and Δt is the pulse width. Q_{pulse} is proportional to optical pulse energy and average photocurrent. From the impulse response waveforms in Figure 7.9, we can see that the pulse width Δt is constant at low photocurrent, and thus E_{pulse} is proportional to the square of Q_{pulse} or average photocurrent. After saturation, the pulse width, Δt, increases linearly with photocurrent as a result of the lateral expansion of the waveform. As a result, E_{pulse} scales linearly with Q_{pulse} and average photocurrent. The authors of [122] point out that in their work the electrical pulse energy is linear with respect to optical pulse energy or average photocurrent over the full data range. This is a clear indication that the commercial photodiode used in their experiment saturates at rather low power levels.

Figure 7.11 shows the 3-dB bandwidths calculated from the impulse response waveforms of the MUTC-4 photodiode using Fast Fourier Transform (FFT). Similar to the small-signal impulse response and two-laser heterodyne CW measurements we have discussed in Chapter 4, the bandwidths of MUTC-4 photodiodes under large-signal pulse excitation initially increase with the photocurrent. This is more evident for smaller devices (20-μm diameter and 28-μm diameter) due to their lower RC delays. The bandwidth reaches a maximum

value then starts to drop with increasing photocurrent. The photocurrent at which the bandwidth maximizes increases with growing bias voltage and scales approximately with the active area of the photodiode. The maximum bandwidth calculated from large-signal impulse response measurement is less than (50%~80%) that from small-signal impulse response and two-laser heterodyne CW measurements in Chapter 4. This early saturation of the MUTC-4 photodiode under large-signal pulse excitation can be attributed to two factors. First the large-signal pulse signal has much higher modulation depth (>>100%) than the signals used in the other two measurements (<1% for small-signal pulse and ≈ 100% for two-laser heterodyne). In other words, a pulse signal has much larger peak-to-average ratio than the signals in the other two measurements. For signals with the amount of RF power, pulse excitations have larger peak values, which cause them to saturate early. Secondly, the assumption that the frequency response obtained from impulse response equals that from method based on frequency sweep as in the two-laser heterodyne measurement relies on the linear properties of the system. This assumption usually does not hold when considering large-signal saturation, which is nonlinear process in nature. In a CW frequency sweep measurement, only one major RF frequency component exists as the input. The multiply frequency components present in an impulse response measurement interact with each other and it is possible that higher frequency components are suppressed by the lower frequency components through nonlinear saturation

effects.

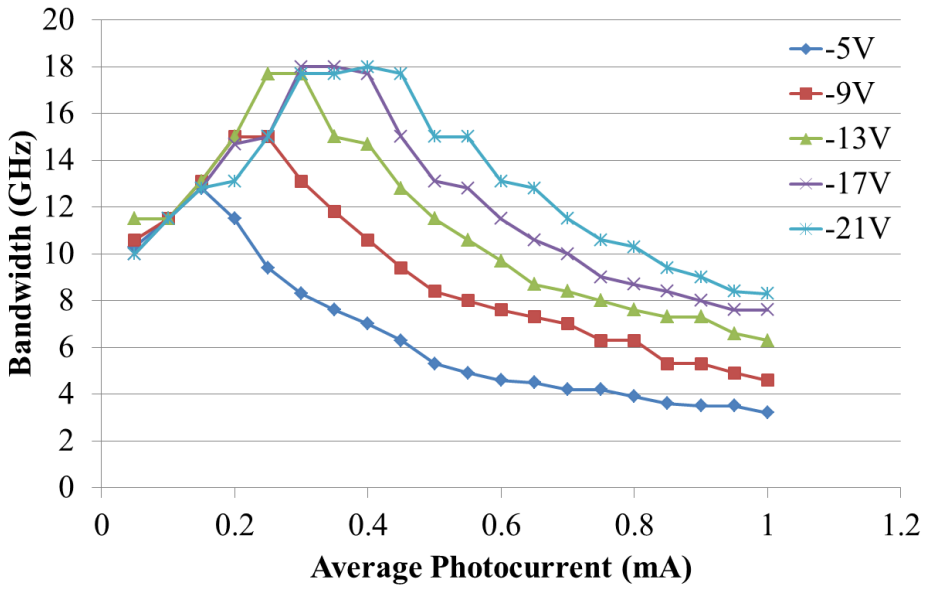
20
18
16
14
12
10
8
6
4
2
0
Bandwidth (GHz)
0
0.2
0.4
0.6
0.8
1
1.2
Average Photocurrent (mA)
-5V
-9V
-13V
-17V
-21V

(a)

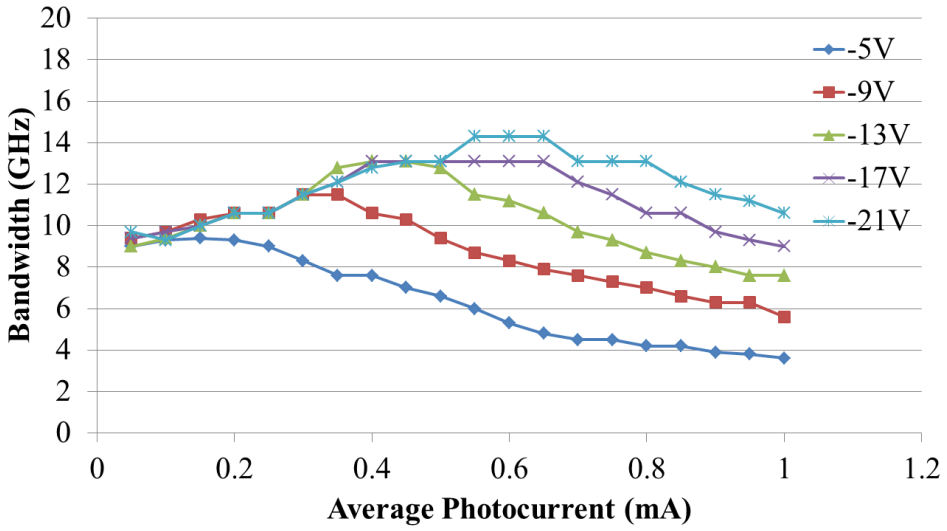
20
18
16
14
12
10
8
6
4
2
0
Bandwidth (GHz)
0
0.2
0.4
0.6
0.8
1
1.2
Average Photocurrent (mA)
-5V
-9V
-13V
-17V
-21V

(b)

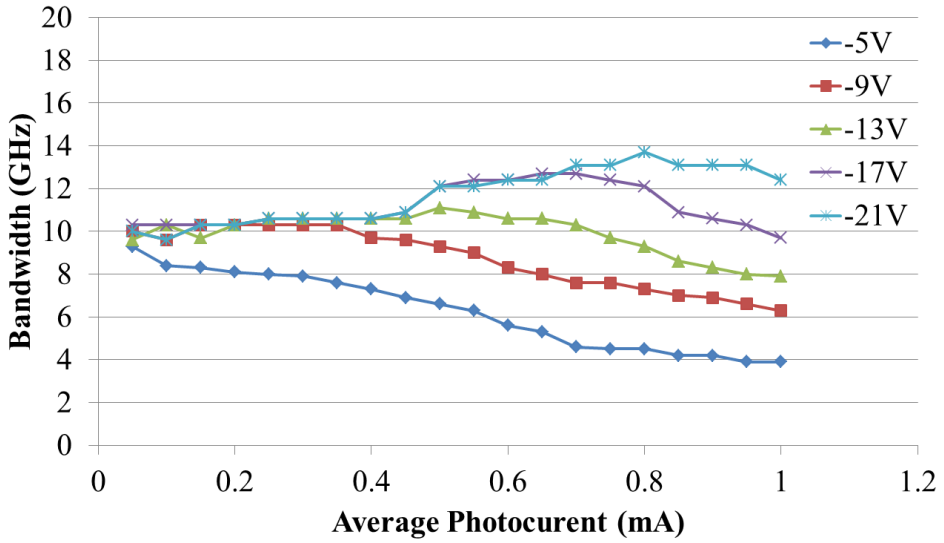

(c)

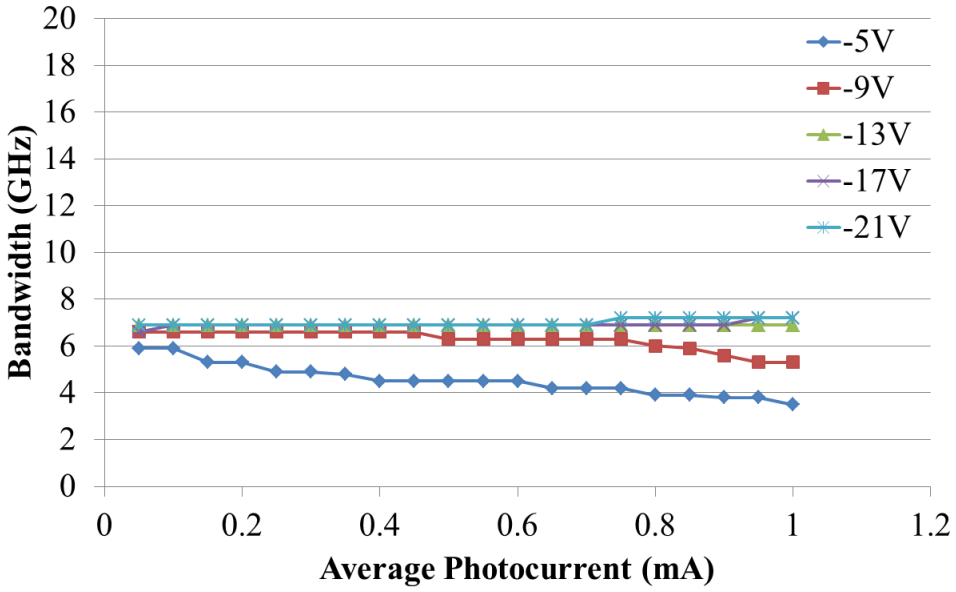

(d)

Figure 7.11 The 3-dB bandwidth calculated from the impulse response waveforms of (a) 20-µm, (b) 28-µm, (c) 40 µm and (d) 56 µm diameter MUTC-4 photodiodes at different bias voltages and average photocurrent.

7.3.2 The AM-to-PM conversion factor

The AM-to-PM conversion factor of the MUTC-4 photodiode is calculated using FFT analysis of the impulse response waveforms [121]. The results for a 20-μm MUTC-4 photodiode at -9 V bias voltage are shown in Figure 7.12. The phase of harmonics is directly extracted using FFT analysis. A 7-th order polynomial is used to fit each harmonic phase curve in order to reduce the discontinuities when calculating the first-order differentials. The polynomial order is chosen in such a way that the resulting differential curve can capture the primary features of the discrete data without introducing significant artifacts. It is worth mentioning that when comparing pulse measurement data, the difference in pulse repetition rate should be considered. The data shown in this section are measured with 100 MHz repetition rate pulses and the average photocurrent needs to be multiplied by 10 in order to compare with data measured at 1 GHz in the previous section.

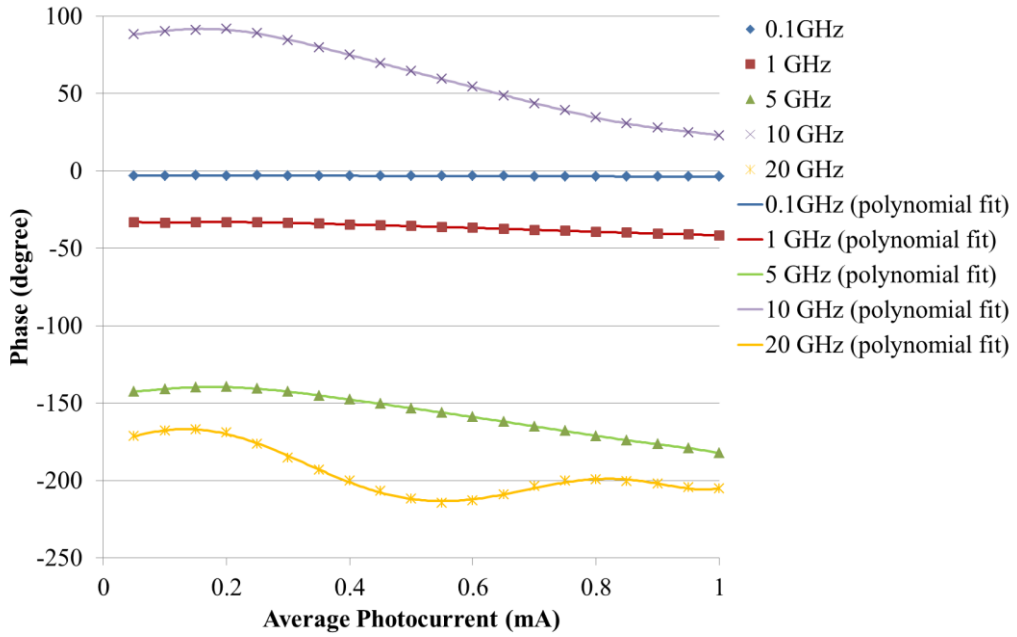
100
50
0
-50
-100
-150
-200
-250
Phase (degree)
0
0.2
0.4
0.6
0.8
1
Average Photocurrent (mA)
0.1GHz
1 GHz
5 GHz
10 GHz
20 GHz
0.1GHz (polynomial fit)
1 GHz (polynomial fit)
5 GHz (polynomial fit)
10 GHz (polynomial fit)
20 GHz (polynomial fit)

(a)

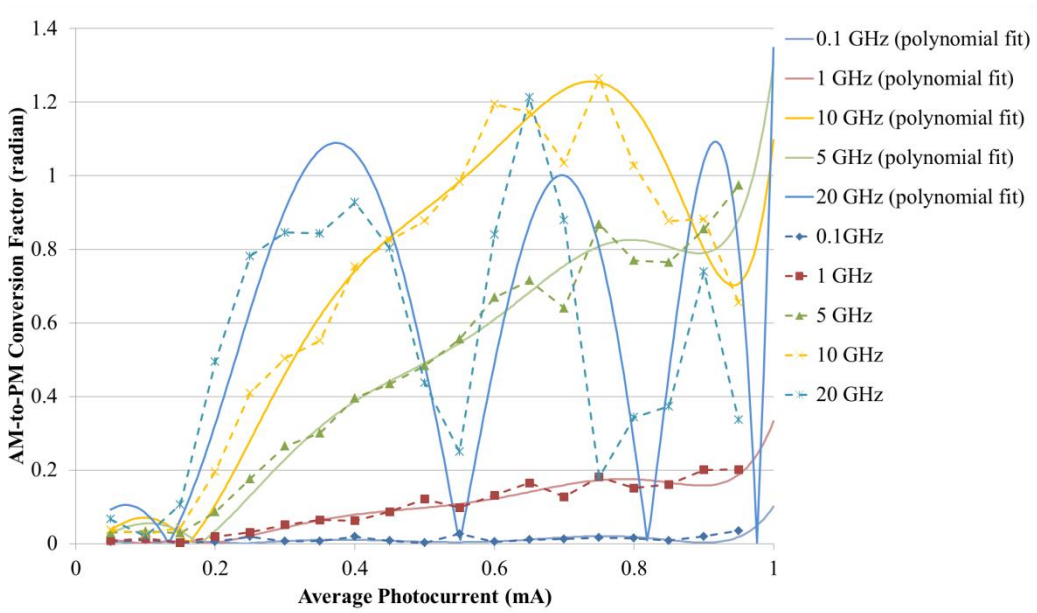
1.4
1.2
1
0.8
0.6
0.4
0.2
0
AM-to-PM Conversion Factor (radian)
0
0.2
0.4
0.6
0.8
1
Average Photocurrent (mA)
0.1 GHz (polynomial fit)
1 GHz (polynomial fit)
10 GHz (polynomial fit)
5 GHz (polynomial fit)
20 GHz (polynomial fit)
0.1GHz
1 GHz
5 GHz
10 GHz
20 GHz

(b)

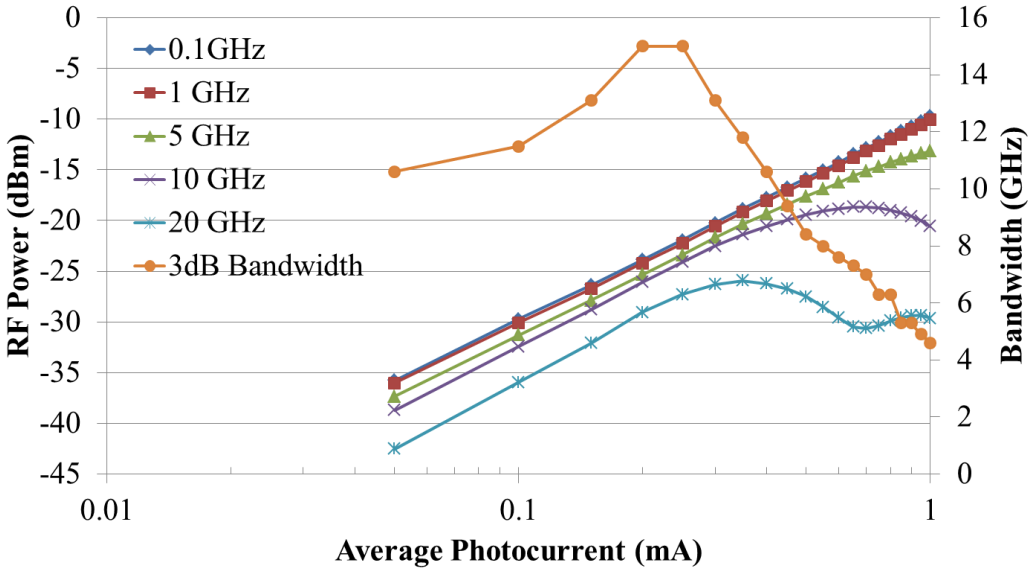

(c)

Figure 7.12 The (a) phase, (b) AM-to-PM conversion factor, and (c) RF power of different harmonics for a 20-µm diameter MUTC-4 photodiode at -9 V bias voltage. The 3dB bandwidth is also shown in (c).

The phases of harmonics at lower frequencies change slowly with photocurrent. At higher frequencies, the phase change is larger and more rapid. There are even oscillatory features in the 20 GHz phase curve. As expected, the AM-to-PM conversion factor generally increases with both frequency and photocurrent. The most distinctive feature in Figure 7.12 is the existence of "zeros" in AM-to-PM conversion factors at certain photocurrent levels. More zeros appear with smaller spacing as the harmonic frequency increases. This phenomenon has been observed in other PIN photodiodes [119-122] and the authors in [122] and [123] have provided phenomenological explanations. It is obvious that operating the OEOs at these zero points could reduce the phase noise

of the system [37, 119, 121].

Comparing the AM-to-PM conversion factors of different harmonics in Figure 7.12 (b), we can see that they all reach zero near 0.15 mA photocurrent. This is slightly before the photocurrent at which the bandwidth of the photodiode reaches a maximum in Figure 7.12 (c). This suggests that this particular zero in the AM-to-PM conversion factor may have a different origin than those that appear at higher photocurrent in a repetitive fashion. If so, the zeros in the AM-to-PM conversion factor can be divided into two categories: the common zero, i.e. the one shared by all harmonics, which occurs right before saturation; and the other zeros after saturation whose positions depend on the harmonic frequency. The correlation between the common zero in the AM-to-PM conversion factor of the MUTC-4 photodiode and its saturation can be seen more clearly in Figure 7.13. Only the AM-to-PM conversion factors at 10 GHz are shown for clarity.

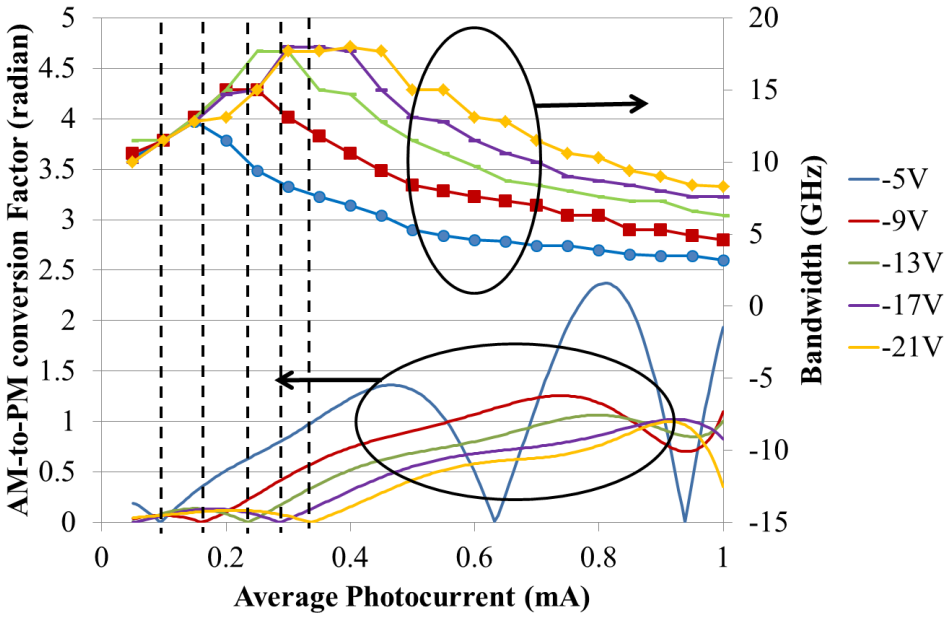

Figure 7.13 The AM-to-PM conversion factor of a 20-μm diameter MUTC-4 photodiode at 10 GHz and its bandwidth at different bias voltages. Dashed lines indicate positions of the zeros in the AM-to-PM conversion factor.

The increase in bandwidth with photocurrent illustrates that as the photodiode speeds up signal phase advances. After the saturation point, the photodiode slows down and retards the signal phase. It follows that there is a photocurrent near the saturation point where the signal phase is relatively independent of photocurrent or power. This is the origin of the common zero in the MUTC-4 photodiode AM-to-PM conversion factors.

Several other observations can be made from Figure 7.13. Before saturation or bandwidth reduction, the AM-to-PM conversion factor is small and only has weak dependence on either bias voltage or photocurrent. This is understandable since before saturation, the carrier transit time in the MUTC-4

photodiode is dominated by the electron transport in the p-type InGaAs absorber. The primary factor that causes the transit time to change is the self-induced field in the p-type absorber, which is determined by photocurrent instead of bias voltage. This results in weak dependence of the AM-to-PM factor on bias voltage. Moreover, the carrier transit time has a quasi-linear dependence on photocurrent (Figure 4.12 in Chapter 4). Therefore, its first-order derivative with respect to photocurrent is almost a constant, which means that the device speed does not change much with varying photocurrent and explains the weak dependence of the AM-to-PM factor on photocurrent. After saturation, the electric field in a significant portion of the depletion region collapses to a small value where the carrier speed is very sensitive to the field strength (velocity modulation regime). Consequently, a small change in either photocurrent or bias voltage can lead to large changes in carrier transit time and signal phase. This gives rise to larger AM-to-PM conversion factors.

The AM-to-PM conversion factors of the MUTC-4 photodiodes with different active areas are compared in Figure 7.14 (a). Larger photodiodes have smaller AM-to-PM conversion factor due to the fact that their bandwidth changes less with photocurrent (RC limited rather than transit time limited) and saturation is not as pronounced. At the same time, we need to consider the RF power output from the photodiode since it is directly related to the shot-noise-limited noise floor. In Figure 7.14 (b), the 56-μm diameter photodiode has low RF power due to

its large RC constant, while the RF power of the 20-µm photodiode saturates at high photocurrent levels.

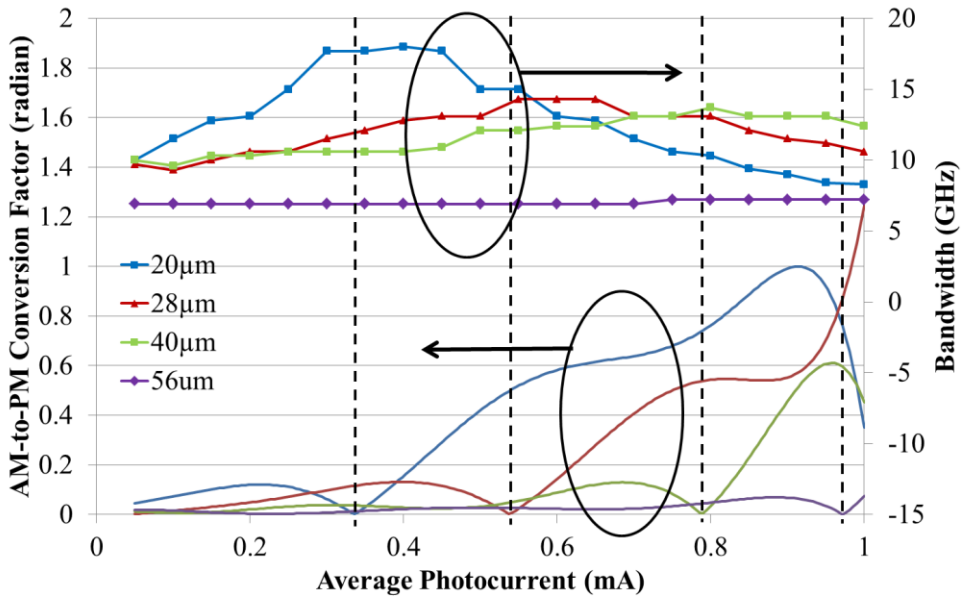

(a)

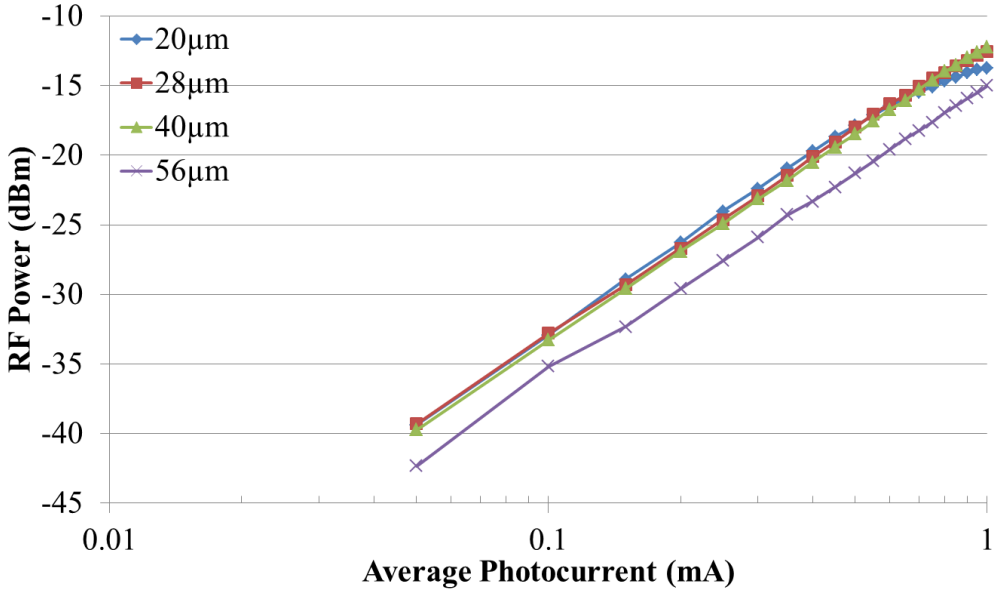

(b)

Figure 7.14 The measurement results for different size MUTC-4 photodiodes at 10 GHz and -21 V bias voltage: (a) AM-to-PM conversion factor and (b) RF power. The 3-dB bandwidth for each photodiode measured at -21 V is also included in the upper half of (a). Dashed lines in (a) mark the positions of zeros in the AM-to-PM conversion factors.

7.4 Summary

In this chapter, the importance of high-power photodiodes for ultra-low phase noise microwave signal generation is discussed. High output power and low phase distortion from the photodiode are both required in order to achieve superior phase noise performance. In collaboration with Dr. Scott Diddams' group at NIST, I successfully integrated the high-power MUTC photodiode into the photonic OEO. The noise floor has been reduced by 10 ~ 20 dB. I continued this work at UVA and systematically characterized the performance of the MUTC-4 photodiode under large-signal pulse excitation. The large-signal pulse bandwidth was found to be quite different from that obtained from small-signal pulse and CW frequency sweep measurements. The AM-to-PM conversion factor of the MUTC-4 photodiode was studied with respect to bias voltage, photocurrent, and device area. A physics explanation was provided for the common "zero" in the AM-to-PM conversion factor. This work may prove beneficial for improving the phase noise performance of photonic OEOs and developing photodiode structures specifically optimized for large-pulse operation.

Chapter 8 Summary and Future Work

8.1 Summary

The primary motivation behind this dissertation has been to study the power and linearity performance of advanced PIN photodiode designs with respect to both internal physical parameters and external microwave circuits. The knowledge gained from this study can then be applied for developing improved photodiode structures.

The first step has been to analyze the basic operation of advanced PIN photodiodes. This not only serves as a solid foundation for future research, but can lead to new discoveries. The MUTC-4 photodiode that has achieved record-high power performance is a good candidate for this purpose. It has proven to be a successful design for RF photonics applications, while at the same time it presents some important questions that need to be answered. First I carried out systematic bandwidth measurements in order to extract the parameters needed to build an accurate model for the MUTC-4 photodiode. I compared the bandwidth results from two measurement techniques: the small-signal impulse response and the

two-laser heterodyne CW measurements. The goal was to distinguish the effects from the DC current offset and the RF component on the photodiode bandwidth. The similar bandwidth results from these two approaches indicate that the DC current offset rather than the RF component is the primary factor that determines the 3-dB bandwidth before saturation. A model for the MUTC-4 photodiode has been developed using Crosslight Apsys software and the simulation results agree well with measurement data. Next by using S-parameter measurements I discovered the existence of negative differential resistance (NDR) while the photodiode is under optical illumination. Through measurements and software modeling, the origin of NDR has been traced back to the p-type InP electron blocking layer and the carrier transport in the undepleted InGaAs absorber. The discovery of NDR and establishment of the model improves our understanding of the fundamental operation of MUTC photodiodes and is useful for future photodiode development.

Next, in order to circumvent limitations on the output power and linearity of a single photodiode, I investigated power combining and resonance techniques. I demonstrated effective power combining and enhanced linearity performance using a monolithically integrated 2×1 Wilkinson power combiner and 2-element HD-PDA photodiode array. The trade-off between output power and linearity was studied using an integrated open-stub tuning circuit. The OIP3 improvement of the tuning stub circuit can be well explained by the responsively change caused

by the voltage swing on the photodiodes. Then I expanded this effort to include 4×1 Wilkinson combiners and HD-MUTC photodiode arrays in order to achieve higher output power and improved linearity. A 6 dB OIP3 improvement has been shown with the 4×1 combiner circuit and an improved 2×1 combiner circuit achieved over 50 dBm OIP3 at 20 GHz.

Studying nonlinear distortions in high-power photodiode has always been a difficult yet quite important task. Fortunately previous and current members of our group (Haupu Pan and Andreas Beling) have developed a measurement-based model that works well to explain intermodulation distortions in high-power photodiodes. I extended this work by building a physics-based model for intermodulation distortion analysis in high-power photodiodes. To this end, I did extensive intermodulation distortion measurements on HD-MUTC photodiodes and found out that the electric-field-dependent responsivity caused by the Franz-Keldysh effect in the depleted InGaAs absorber was the major contributor to photodiode nonlinearities at low frequencies. The simulation results agree with measurement data very well. After building this model, I found out that the simulations of the third-order intermodulation distortions (IMD3s) showed 180 degree phase transitions near the OIP3 peaks. Then I built a phase-sensitive IMD3 measurement setup and confirmed the model predictions. This discovery not only added support for my model, but can also be used to improve photodiode linearity through IMD3 cancellation.

My most recent pursuit involves application of high-power MUTC photodiodes in ultra-low phase noise microwave generation systems. Dr. Scott Diddams' group at NIST had demonstrated champion results of low phase noise OEO at 10 GHz. However, further noise reduction was limited by the power handling capability of the photodiode under large-signal pulse excitation. In collaboration with Dr. Scott Diddams' group members at NIST, I successfully integrated the high-power MUTC photodiode into the photonic OEO. The results were very promising and the noise floor had been reduced by 10 ~ 20 dB. I continued this work at UVA and systematically characterized the performance of the MUTC-4 photodiode under large-signal pulse excitation. The large-signal pulse bandwidth was found to be quite different from that obtained from small-signal pulse and CW frequency sweep measurements. The AM-to-PM conversion factor of the MUTC-4 photodiode was studied with respect to bias voltage, photocurrent and device area. I have provided a physical explanation for the common "zero" in the AM-to-PM conversion factor. This work was useful for improving the phase noise performance of photonic OEOs and may be a useful development tool for photodiode structures specifically optimized for large-pulse operation.

8.2 Future Work

8.2.1 High-linearity MUTC photodiode with graded-bandgap InGaAsP absorber

Although the HD-MUTC photodiode has achieved very high peak OIP3 values (55 dBm), it is always desirable to increase the OIP3 values in the "valleys" that constitute the largest portion on the photocurrent scale. This would also greatly relax the precision needed to control the photocurrent. We have previously seen in Chapter 6 that the electric field dependent responsivity caused by Franz-Keldysh effect in the depleted InGaAs absorber is the primary source of nonlinear distortions at low frequencies. Therefore if the dependence of the responsivity on electric field can be reduced then higher OIP3 values can be achieved. One way to accomplish this goal is to use graded-bandgap InGaAsP as the depleted absorber.

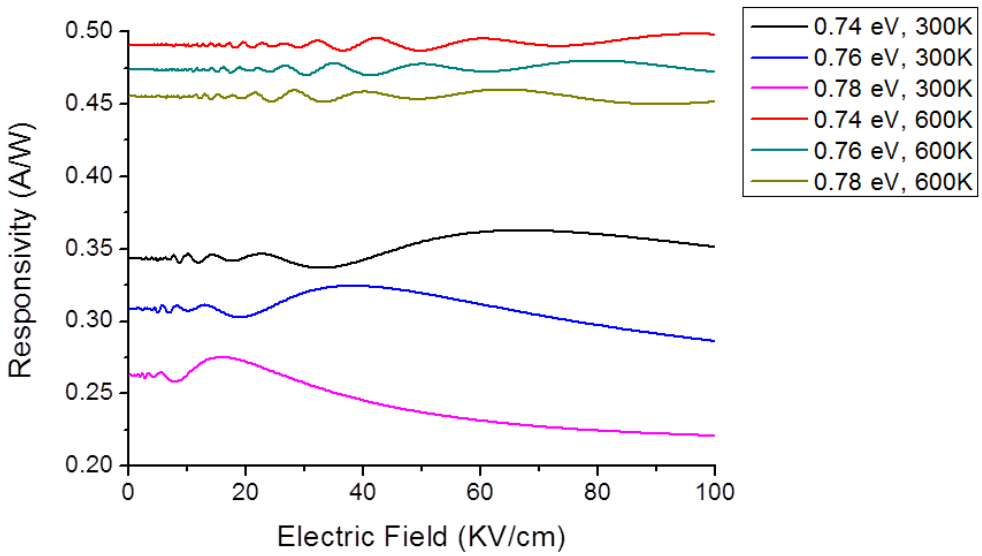

Figure 8.1 Calculated responsivity of depleted InGaAsP absorber with different bandgaps. Bias voltage = -7 V, modulation depth = 80%, light wavelength = 1543 nm

Figure 8.1 shows the calculated responsivity of an HD-MUTC photodiode with the depleted InGaAs absorber replaced by InGaAsP layers with different bandgaps. It can be seen that the responsivity curves of InGaAsP with different bandgaps are "out of phase" with each other with respect to electric field. This is a very important observation. If the depleted absorber consists of InGaAsP layers with multiple bandgaps, then with proper design, the total responsivity can have less dependence on electric field, which will result in higher OIP3. One such example is shown in Figure 8.2. The InGaAsP absorber consists of two different bandgaps, 0.74 eV and 0.76 eV. Their individual responsivity curves are almost "out of phase" with each other and the resultant total responsivity is much "flatter".

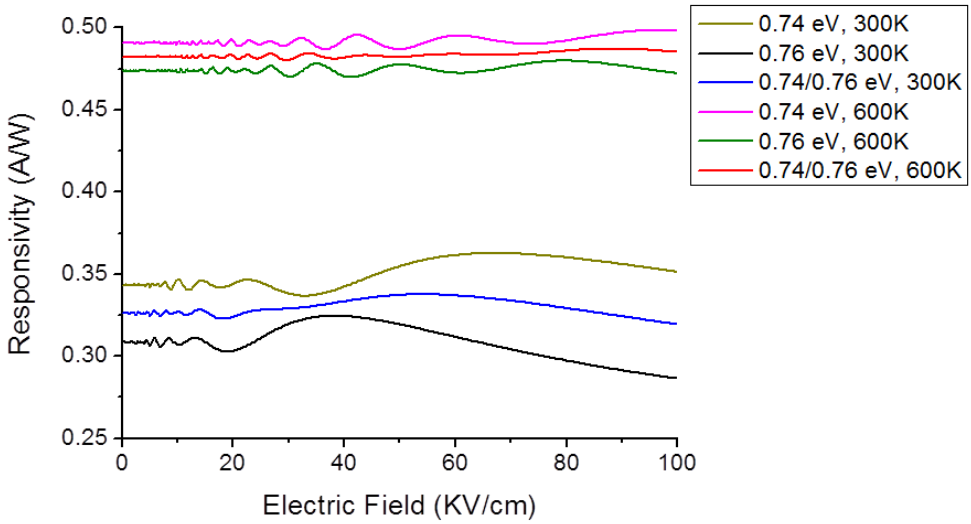

Figure 8.2 Calculated responsivity of InGaAsP absorber with two different bandgap layers, 0.74 eV and 0.76 eV.

The calculated OIP3 of three design examples with different InGaAsP compositions are shown in Figure 8.3. It can be seen that the OIP3 value increases by almost 8 dB in the design with 0.74/0.78 eV InGaAsP absorbers and 4 dB in the other two designs. Therefore larger bandgap difference is desirable for improving OIP3. Designs with more than two grading steps have also been simulated, but do not show much improvement over the basic two-step grading design.

There are several challenges for the graded-bandgap design. The bandgap discontinuities can impede carrier transport. The responsivity of larger bandgap InGaAsP layer is lower than InGaAs. Material quality might be an issue for multiple InGaAsP layers. The precision needed in InGaAsP bandgap control has

approached the capability limit of some commercial epitaxial wafer vendors.

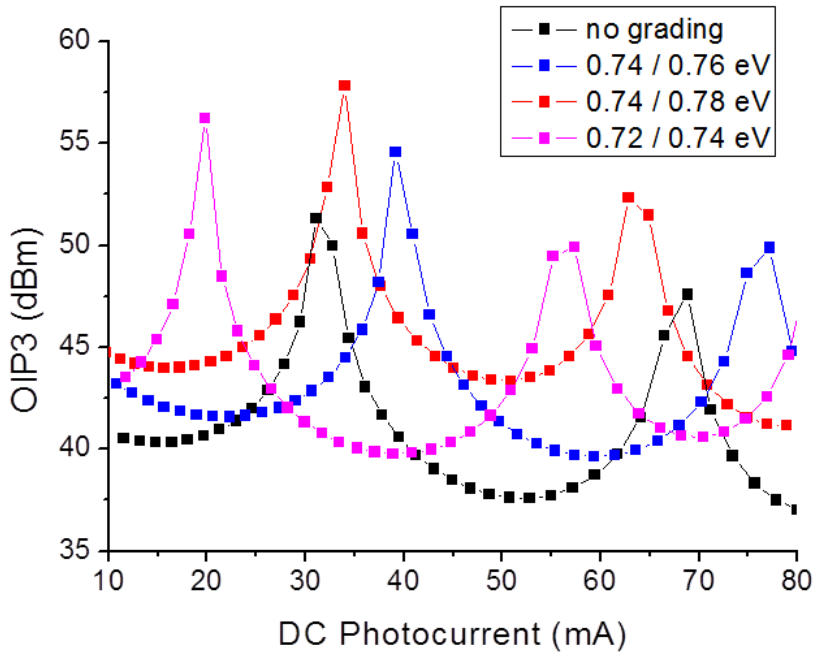

Figure 8.3 The calculated OIP3 value of three graded-bandgap absorber designs. The depleted absorber in each design is made up by InGaAsP layers with two different bandgaps. The OIP3 of a single bandgap absorber design (HD-MUTC) is included for comparison.

The MUTC photodiode with graded-bandgap absorber I have designed is shown in Figure 8.4.

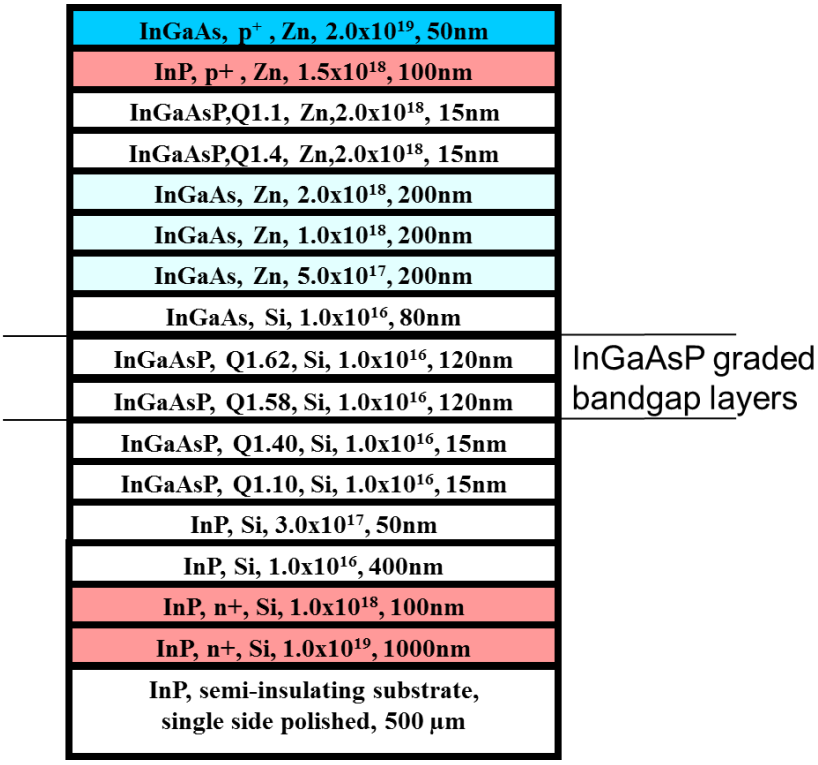

Figure 8.4 The epitaxial structure design of MUTC photodiode with graded-bandgap InGaAsP absorber.

8.2.2 Integrated lumped element Wilkinson combiner with high-power photodiodes

The distributed Wilkinson power combiner has a major disadvantage of being physically large at lower frequencies due to the requirement for quarter-wave transmission lines. This consumes a large amount of valuable chip area. A hybrid design based on flip-chip bonding could solve this problem by placing the

Wilkinson combiner on inexpensive substrates such as AlN. But the process variation of flip-bonding presents a large uncertainty for the electromagnetic (EM) design. An alternate approach is to use a lumped element Wilkinson power combiner.

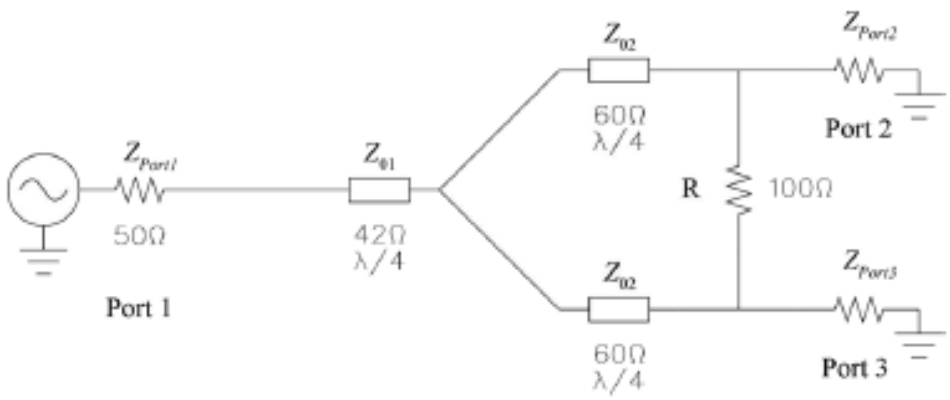

(a)

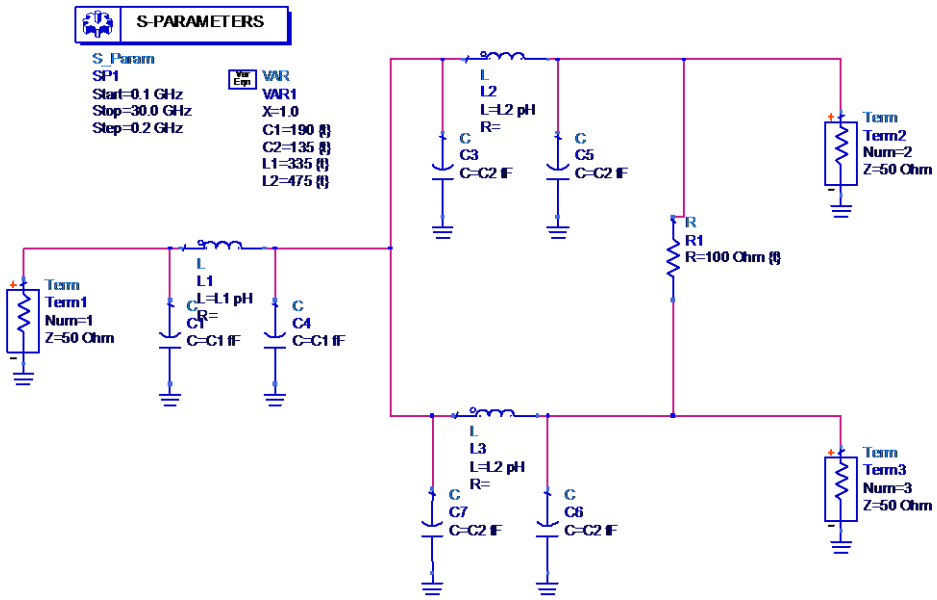

(b)

Figure 8.5 A broadband Wilkinson power combiner design realized in (a) distributed form and (b) lumped element form.

A broadband Wilkinson power combiner design based on transmission lines is shown in Figure 8.5 (a). An extra section of quarter-wave transmission line has been added at the system output to increase the bandwidth. To make a lumped element design, each transmission line section is replaced with a π-LC circuit. Spiral inductors and Metal-Insulator-Metal (MIM) capacitors are used in a planar environment. The lumped element Wilkinson power combiner I have designed is shown in Figure 8.6. The center frequency is 20 GHz. The substrate is semi-insulating InP (dielectric constant = 12.6). The area of the lumped Wilkinson power combiner is 0.3 mm × 0.4 mm, which is much smaller than the original distributed design (2.6 mm × 0.8 mm).

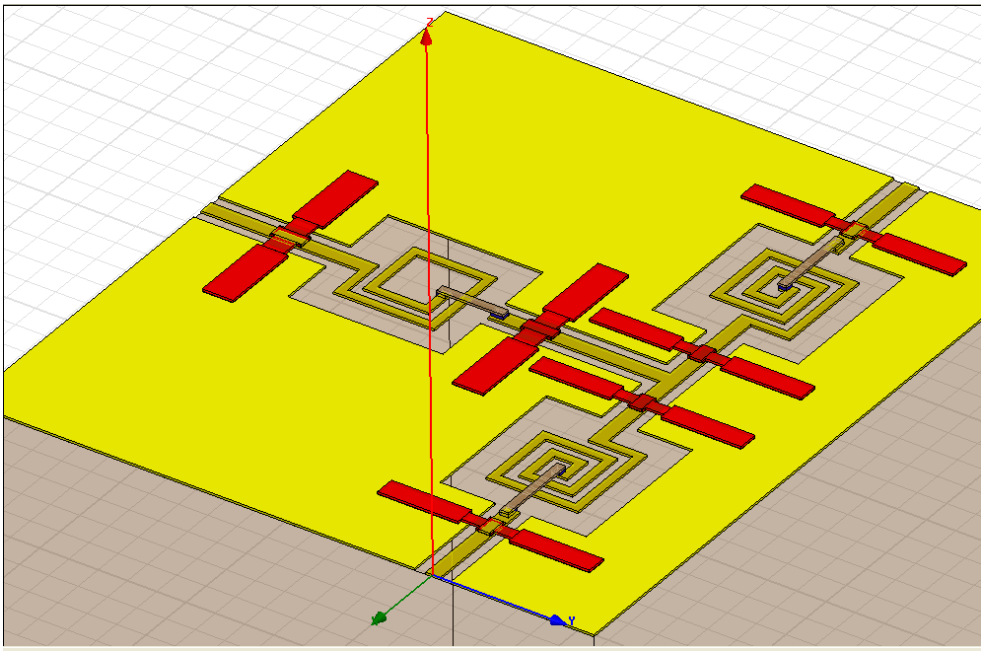

Figure 8.6 Lumped element Wilkinson power combiner in Ansoft HFSS

The S-parameter simulation results for the lumped element Wilkinson power combiner are shown in Figure 8.7. The excess insertion loss is approximately 1 dB at the center frequency and the bandwidth (-10 dB) is ~ 6 GHz. Major challenges include fabrication of the tightly wound inductor loops and the dielectric material quality used in the MIM capacitors.

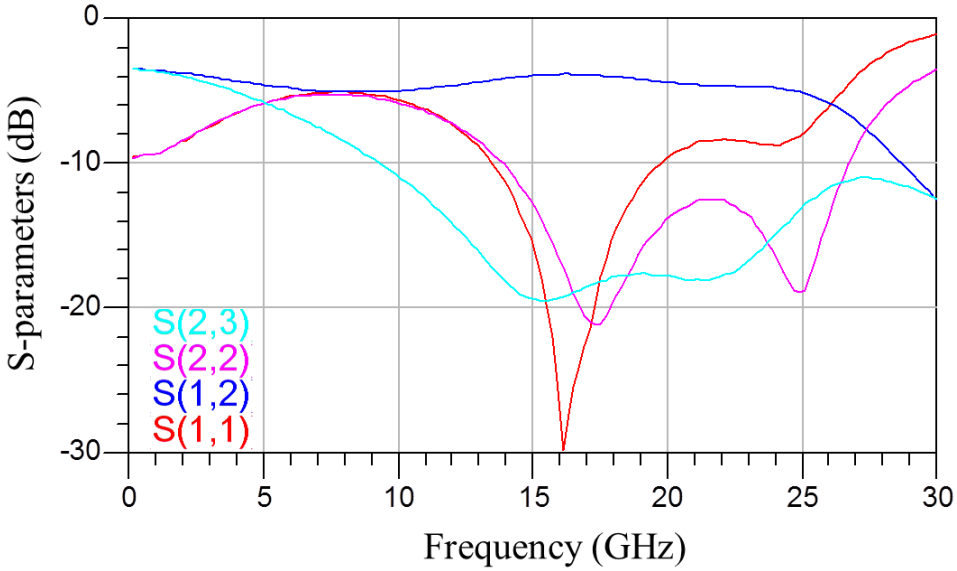

Figure 8.7 Simulated S-parameters of the lumped element Wilkinson combiner.

Appendix I Parameters for Crosslight Apsys Simulation

The GaAs-type field-dependent mobility model with negative differential mobility (NDM) was used for electrons in InGaAs and InP.

$$\mu_n = \frac{\mu_{0n} + (v_{sn}/F_{0n})(F/F_{0n})^3}{1 + (F/F_{0n})^4}.$$

Where μ_n is the electron mobility, F is the electric field strength, v_{sn} is the electron saturation velocity, and F_{0n} is the normalization electric field.

The Si-type field-dependent mobility model was used for holes in InGaAs and InP.

$$\mu_p = \frac{\mu_{0p}}{(1 + (\mu_{0p}F/v_{sp})^{\beta_p})^{1/\beta_p}}.$$

Where μ_p is the hole mobility, F is the electric field strength, v_{sp} is the hole saturation velocity, and μ_{0p} is the low-field hole mobility.

The low-field mobility's dependence on doping concentrations is described by the following equations:

$$\mu_{0n} = \mu_{1n} + \frac{(\mu_{2n} - \mu_{1n})}{1 + \left(\frac{N_D + N_A + \sum_j N_{tj}}{N_{rn}}\right)^{\alpha_n}},$$

$$\mu_{0p} = \mu_{1p} + \frac{(\mu_{2p} - \mu_{1p})}{1 + \left(\frac{N_D + N_A + \sum_j N_{tj}}{N_{rp}}\right)^{\alpha_p}}$$

Where μ_{0n} is the low-field electron mobility, μ_{1n} is the minimum electron mobility, μ_{2n} is the maximum electron mobility, N_D and N_A are doping concentrations for donors and acceptors, respectively, N_{tj} is the trapping concentration, N_{rn} is the reference doping/trapping concentration and α_n is a coefficient.

The parameter values are listed in the following table.

Parameter	InGaAs	InP
Energy bandgap (eV)	0.74	1.34
Dielectric constant	13.9	12.6
Electron affinity (eV)	4.32	4.07
Electron mass (m0)	0.041	0.078
Hole mass (m0)	0.54	0.588
μ_{1n} $(m^2V^{-1}S^{-1})$	0.34	0
$\mu_{2n}(m^2V^{-1}S^{-1})$	1.0	0.45
μ_{1p} $(m^2V^{-1}S^{-1})$	0.0075	0.002

μ_{2p} $(m^2V^{-1}S^{-1})$	0.036	0.015
N_{rn} (m^{-3})	9×10^{22}	6×10^{23}
N_{rp} (m^{-3})	1×10^{24}	7×10^{23}
α_n	0.76	0.46
α_p	1.37	0.96
v_{sn} (ms^{-1})	0.75×10^5	0.8×10^5
$v_{sp}(ms^{-1})$	0.6×10^5	0.45×10^5
β_n	2	2
β_p	1	1
F_{0n} (Vm^{-1})	4.5×10^5	15×10^5

Publication list

- **Yang Fu**, H. Pan and J. C. Campbell, “Photodiodes With Monolithically Integrated Wilkinson Power Combiner”, *IEEE Journal of Quantum Electronics*, vol. 46, no. 4, Apr. 2010
- **Yang Fu**, H. Pan, Z. Li and J. C. Campbell, “High linearity photodiode array with monolithically integrated Wilkinson power combiner”, *Microwave Photonics (MWP), 2010 IEEE Topical Meeting on* , Montreal, QC, Oct. 2010
- **Yang Fu**, H. Pan and J. C. Campbell, “Photodiodes With Monolithically Integrated Wilkinson Power Combiner”, *Optical Fiber Communication Conference (OFC)*, paper JWA39, San Diego, CA, Mar. 2010
- **Yang Fu**, Huapu Pan, Andreas Beling and Joe Campbell, “Phase Characterization of Intermodulation Distortion in High-Linearity Photodiodes”, IEEE ISCS/IPRM 2012, Santa Barbara, CA, Aug. 2012
- **Yang Fu**, H. Pan, Z. Li, A. Beling, and J. C. Campbell, "Characterizing and Modeling Nonlinear Intermodulation Distortions in Modified Uni-Traveling Carrier Photodiodes," *IEEE Journal of Quantum Electronics*, vol.47, no.10, Oct. 2011
- H. Pan, **Yang Fu**, Z. Li and J. C. Campbell, "High-linearity modified uni-

traveling carrier photodiodes," *Optical Fiber Communication Conference (OFC)*, San Diego, CA, Mar. 2010

- Z. Li, H. Pan, **Yang Fu** and J. C. Campbell, "Optoelectronic mixer based on high power modified uni-traveling-carrier photodiode," Microwave Photonics (MWP), 2010 IEEE Topical Meeting on, Montreal, QC, Oct. 2010
- **Yang Fu**, Z. Li, A. Beling, J.C. Campbell, J. Taylor, H. Jiang, F. Quinlan, T. Fortier, S. A. Diddams, "Pulse mode characterization of high-power modified uni-traveling carrier photodiodes", 2011 IEEE Photonics Conference (PHO 2011), Oct. 2011
- H. Jiang, J. Taylor, **Yang Fu**, Z. Li, F. Quinlan, T. Fortier, J. C. Campbell and S. A. Diddams, "Photodetection noise reduction of a 10 GHz fiber-laser-based photonic microwave generator", 2012 IEEE International Frequency Control Symposium (IFCS 2012), Baltimore, MD, May. 2012
- Z. Li, **Yang Fu**, M. Piels, H. Pan, A. Beling, J. E. Bowers, J. C. Campbell, "High-power high-linearity flip-chip bonded modified uni-traveling carrier photodiode," Opt. Express 19, B385-B390, 2011
- A. Beling, **Yang Fu**, Z. Li, H. Pan, Q. Zhou, A. Cross, M. Piels, J. Peters, J. E. Bowers, and J. C. Campbell, "Modified Uni-Traveling Carrier Photodiodes Heterogeneously Integrated on Silicon-on-Insulator (SOI)", Integrated Photonic Research Conference, Colorado Springs, CO, Jun.

2012

Bibliography

1. Agrawal, G.P., *Fiber-optic communication systems*. Vol. 222. 2012: Wiley.
2. Savage, N., *Linking with light [high-speed optical interconnects]*. Spectrum, IEEE, 2002. **39**(8): p. 32-36.
3. Cox III, C.H., *Analog optical links: theory and practice*. 2006: Cambridge University Press.
4. Capmany, J. and D. Novak, *Microwave photonics combines two worlds.* Nature Photonics, 2007. **1**(6): p. 319-330.
5. Seeds, A.J., *Microwave photonics.* Microwave Theory and Techniques, IEEE Transactions on, 2002. **50**(3): p. 877-887.
6. Urick, V.J., et al., *Long-Haul Analog Photonics.* Lightwave Technology, Journal of, 2011. **29**(8): p. 1182-1205.
7. Yao, J., *Microwave photonics.* Lightwave Technology, Journal of, 2009. **27**(3): p. 314-335.
8. Phillips, M.R. and T.E. Darcie, *Lightwave analog video transmission.* Optical Fiber Telecommunications IIIA, 1997: p. 523-559.
9. Wilson, B., Z. Ghassemloooy, and I. Darwazeh, *Analogue optical fibre communications*. Vol. 32. 1995: Iet.
10. Williamson, R.C. and R.D. Esman, *RF Photonics*. Lightwave Technology,

Journal of, 2008. **26**(9): p. 1145-1153.

11. Frankel, M.Y., P.J. Matthews, and R.D. Esman, *Fiber-optic true time steering of an ultrawide-band receive array.* Microwave Theory and Techniques, IEEE Transactions on, 1997. **45**(8): p. 1522-1526.

12. Loo, R.Y., et al. *Photonics for phased-array antennas*. in *Society of Photo-Optical Instrumentation Engineers (SPIE) Conference Series*. 1996.

13. Shillue, B. *Atacama Large Millimeter Array photonic local oscillator: femtosecond-level synchronization for radio astronomy*. in *Frequency Control Symposium (FCS), 2010 IEEE International*. 2010.

14. Kiuchi, H., M. Saito, and S. Iguchi, *Photonic local oscillator technics for large-scale interferometers.* 2012: p. 84442O-84442O.

15. Minasian, R.A., *Photonic signal processing of microwave signals.* Microwave Theory and Techniques, IEEE Transactions on, 2006. **54**(2): p. 832-846.

16. Campillo, A., et al., *Phase performance of an eight-channel wavelength-division-multiplexed analog-delay line.* Journal of lightwave technology, 2004. **22**(2): p. 440.

17. Capmany, J., B. Ortega, and D. Pastor, *A tutorial on microwave photonic filters.* Journal of lightwave technology, 2006. **24**(1): p. 201.

18. Chou, J., Y. Han, and B. Jalali, *Adaptive RF-photonic arbitrary waveform generator.* Photonics Technology Letters, IEEE, 2003. **15**(4): p. 581-583.

19. Valley, G.C., *Photonic analog-to-digital converters.* Optics Express, 2007. **15**(5): p. 1955-1982.

20. Shoop, B.L., *Photonic analog-to-digital conversion*. Vol. 81. 2001: Springer.

21. Maleki, L., *Sources: The optoelectronic oscillator.* Nat Photon, 2011. **5**(12): p. 728-730.

22. Yao, X.S. and L. Maleki, *Optoelectronic microwave oscillator.* JOSA B, 1996. **13**(8): p. 1725-1735.

23. Adachi, S., *Physical Properties of III-V Semiconductor Compounds: InP, InAs, GaAs, GaP, InGaAs, and InGaAsP*. 1992: Wiley-Interscience.

24. Luth, H. and H. Ibach, *Solid-State Physics: An Introduction to Principles of Materials Science*. 1995, Springer Verlag.

25. Beling, A. and J.C. Campbell, *InP-Based High-Speed Photodetectors.* Lightwave Technology, Journal of, 2009. **27**(3): p. 343-355.

26. Tulchinsky, D.A., et al., *High-Current Photodetectors as Efficient, Linear, and High-Power RF Output Stages.* Lightwave Technology, Journal of, 2008. **26**(4): p. 408-416.

27. Williams, K.J. and R.D. Esman, *Design considerations for high-current photodetectors.* Lightwave Technology, Journal of, 1999. **17**(8): p. 1443-1454.

28. Ning, D., et al., *Thermal Analysis of High-Power InGaAs–InP*

Photodiodes. Quantum Electronics, IEEE Journal of, 2006. **42**(12): p. 1255-1258.

29. Susumu, H., K. KAWANO, and A. KOZEN, *Design of Ultrawide-Band, High-Sensitivity pin Protodetectors.* IEICE Transactions on Electronics, 1993. **76**(2): p. 214-221.

30. Yong-Liang, H. and S. Chi-Kuang, *Nonlinear saturation behaviors of high-speed p-i-n photodetectors.* Lightwave Technology, Journal of, 2000. **18**(2): p. 203-212.

31. Nagatsuma, T., H. Ito, and T. Ishibashi, *High-power RF photodiodes and their applications.* Laser & Photonics Reviews, 2009. **3**(1-2): p. 123-137.

32. Xiaowei, L., et al., *High-saturation-current InP-InGaAs photodiode with partially depleted absorber.* Photonics Technology Letters, IEEE, 2003. **15**(9): p. 1276-1278.

33. Walker, J., ed. *Handbook of RF and Microwave Power Amplifiers*. 1 ed. 2012, Cambridge University Press: New York. 115-116.

34. Cox, C.H., III, et al., *Limits on the performance of RF-over-fiber links and their impact on device design.* Microwave Theory and Techniques, IEEE Transactions on, 2006. **54**(2): p. 906-920.

35. Williams, K.J., L.T. Nichols, and R.D. Esman, *Photodetector nonlinearity limitations on a high-dynamic range 3 GHz fiber optic link.* Lightwave Technology, Journal of, 1998. **16**(2): p. 192-199.

36. Valley, G.C., *Photonic analog-to-digital converters.* Opt. Express, 2007. **15**(5): p. 1955-1982.

37. Fortier, T.M., et al., *Generation of ultrastable microwaves via optical frequency division.* Nat Photon, 2011. **5**(7): p. 425-429.

38. Ozeki, T. and E.H. Hara, *Measurement of nonlinear distortion in photodiodes.* Electronics Letters, 1976. **12**(3): p. 80-81.

39. Esman, R.D. and K.J. Williams, *Measurement of harmonic distortion in microwave photodetectors.* Photonics Technology Letters, IEEE, 1990. **2**(7): p. 502-504.

40. Williams, K.J., R.D. Esman, and M. Dagenais, *Nonlinearities in p-i-n microwave photodetectors.* Lightwave Technology, Journal of, 1996. **14**(1): p. 84-96.

41. Humphreys, D.A. and R.A. Lobbett, *Investigation of an optoelectronic nonlinear effect in a GaInAs photodiode, and its application of a coherent optical communication system.* Optoelectronics, IEE Proceedings J, 1988. **135**(1): p. 45-51.

42. Dentan, M. and B. de Cremoux, *Numerical simulation of the nonlinear response of a p-i-n photodiode under high illumination.* Lightwave Technology, Journal of, 1990. **8**(8): p. 1137-1144.

43. Williams, K.J. and R.D. Esman, *Photodiode DC and microwave nonlinearity at high currents due to carrier recombination nonlinearities.*

Photonics Technology Letters, IEEE, 1998. **10**(7): p. 1015-1017.

44. Williams, K.J. and P.G. Goetz. *Photodiode compression due to current-dependent capacitance*. in *Microwave Photonics, 2000. MWP 2000. International Topical Meeting on*. 2000.

45. Jiang, H., et al., *The frequency behavior of the third-order intercept point in a waveguide photodiode.* Photonics Technology Letters, IEEE, 2000. **12**(5): p. 540-542.

46. Hastings, A.S., M. Draa, and K. Williams. *Quantifying current-dependant quantum efficiency photodiode nonlinearities*. in *Microwave Photonics, 2011 International Topical Meeting on & Microwave Photonics Conference, 2011 Asia-Pacific, MWP/APMP*. 2011.

47. Bennett, B.R., R.A. Soref, and J.A. Del Alamo, *Carrier-induced change in refractive index of InP, GaAs and InGaAsP.* Quantum Electronics, IEEE Journal of, 1990. **26**(1): p. 113-122.

48. Suzuki, N. and K. Tada, *Electrooptic Properties and Raman Scattering in InP.* Japanese Journal of Applied Physics. **23**(Copyright (C) 1984 Publication Board, Japanese Journal of Applied Physics): p. 291.

49. Stievater, T.H. and K.J. Williams, *Thermally induced nonlinearities in high-speed p-i-n photodetectors.* Photonics Technology Letters, IEEE, 2004. **16**(1): p. 239-241.

50. Fiber-span.com (2012) *Application Note on the Spurious Free Dynamic*

Range.

51. Lerdworatawee, J. and N. Won, *Revisiting spurious-free dynamic range of communication receivers.* Circuits and Systems I: Regular Papers, IEEE Transactions on, 2006. **53**(4): p. 937-943.

52. Sakai, K., et al., *High-Current Back-Illuminated Partially Depleted-Absorber p-i-n Photodiode With Depleted Nonabsorbing Region.* Microwave Theory and Techniques, IEEE Transactions on, 2010. **58**(11): p. 3154-3160.

53. Effenberger, F.J. and A.M. Joshi, *Ultrafast, dual-depletion region, InGaAs/InP p-i-n detector.* Lightwave Technology, Journal of, 1996. **14**(8): p. 1859-1864.

54. Williams, K.J., *Comparisons between dual-depletion-region and uni-travelling-carrier p-i-n photodetectors.* Optoelectronics, IEE Proceedings -, 2002. **149**(4): p. 131-137.

55. Davis, G.A., et al., *A 920-1650-nm high-current photodetector.* Photonics Technology Letters, IEEE, 1996. **8**(10): p. 1373-1375.

56. Ishibashi, T., et al. *Uni-Traveling-Carrier Photodiodes*. 1997: Optical Society of America.

57. Rouvalis, E., et al., *Continuous Wave Terahertz Generation From Ultra-Fast InP-Based Photodiodes.* Microwave Theory and Techniques, IEEE Transactions on, 2012. **60**(3): p. 509-517.

58. Ning, L., et al., *High-saturation-current charge-compensated InGaAs-InP uni-traveling-carrier photodiode.* Photonics Technology Letters, IEEE, 2004. **16**(3): p. 864-866.

59. Zhi, L., et al., *High-Saturation-Current Modified Uni-Traveling-Carrier Photodiode With Cliff Layer.* Quantum Electronics, IEEE Journal of, 2010. **46**(5): p. 626-632.

60. Chtioui, M., et al., *High Responsivity and High Power UTC and MUTC GaInAs-InP Photodiodes.* Photonics Technology Letters, IEEE, 2012. **24**(4): p. 318-320.

61. Huapu, P., A. Beling, and J.C. Campbell, *High-Linearity Uni-Traveling-Carrier Photodiodes.* Photonics Technology Letters, IEEE, 2009. **21**(24): p. 1855-1857.

62. Shi, J.W., et al., *High-Speed, High-Responsivity, and High-Power Performance of Near-Ballistic Uni-Traveling-Carrier Photodiode at 1.55-um Wavelength.* Photonics Technology Letters, IEEE, 2005. **17**(9): p. 1929-1931.

63. Jin-Wei, S., K. Feng-Ming, and J.E. Bowers, *Design and Analysis of Ultra-High-Speed Near-Ballistic Uni-Traveling-Carrier Photodiodes Under a 50-ohm Load for High-Power Performance.* Photonics Technology Letters, IEEE, 2012. **24**(7): p. 533-535.

64. Williams, K. *Comparisons between dual-depletion-region and uni-*

travelling-carrier pin photodetectors. in *Optoelectronics, IEE Proceedings*-. 2002: IET.

65. Joshi, A.M. *DC to 65 GHz Wide Bandwidth InGaAs Photodiodes and Photoreceivers*. in *MRS Proceedings*. 1999: Cambridge Univ Press.

66. Joshi, A. and D. Becker. *GRIN lens-coupled top-illuminated photodetectors for high-power applications*. in *Microwave Photonics, 2007 IEEE International Topical Meeting on*. 2007: IEEE.

67. Ito, H., et al., *InP/InGaAs uni-travelling-carrier photodiode with 220 Ghz bandwidth.* Electronics Letters, 1999. **35**(18): p. 1556-1557.

68. Wu, Y.S. and J.W. Shi, *Dynamic Analysis of High-Power and High-Speed Near-Ballistic Unitraveling Carrier Photodiodes at< formula>< img src=*. Photonics Technology Letters, IEEE, 2008. **20**(13): p. 1160-1162.

69. Hao, C., et al., *A Method to Estimate the Junction Temperature of Photodetectors Operating at High Photocurrent.* Quantum Electronics, IEEE Journal of, 2009. **45**(12): p. 1537-1541.

70. Huapu, P., et al., *A High-Linearity Modified Uni-Traveling Carrier Photodiode With Offset Effects of Nonlinear Capacitance.* Lightwave Technology, Journal of, 2009. **27**(20): p. 4435-4439.

71. Huapu, P., et al., *Characterization of High-Linearity Modified Uni-Traveling Carrier Photodiodes Using Three-Tone and Bias Modulation Techniques.* Lightwave Technology, Journal of, 2010. **28**(9): p. 1316-1322.

72. Xiaowei, L., et al., *A partially depleted absorber photodiode with graded doping injection regions.* Photonics Technology Letters, IEEE, 2004. **16**(10): p. 2326-2328.

73. Inc., C.S. *Crosslight APSYS.*; Available from: http://www.crosslight.com/products/apsys.shtml.

74. Ning, L., *High-Output-Power Photodetectors for Analog Optical Links and Avalanche Photodiodes with undepleted absorber*. 2005, The University of Texas at Austin.

75. *Toptica Photonics*. Available from: http://www.toptica.com/products/ultrafast_fiber_lasers.html.

76. Pedro, J.C. and N.B. Carvalho, *Intermodulation Distortion in Microwave and Wireless Circuits*. 1 ed. 2003: Artech House, Inc. 25-59.

77. Fager, C., et al., *A comprehensive analysis of IMD behavior in RF CMOS power amplifiers.* Solid-State Circuits, IEEE Journal of, 2004. **39**(1): p. 24-34.

78. Ramaswamy, A., et al., *Measurement of intermodulation distortion in high-linearity photodiodes.* Opt. Express, 2010. **18**(3): p. 2317-2324.

79. Ishibashi, T., et al. *Photoresponse characteristics of uni-traveling-carrier photodiodes*. in *Proc. SPIE*. 2001. San Jose, CA, USA: SPIE.

80. Ito, H., et al., *High-speed and high-output InP-InGaAs unitraveling-carrier photodiodes.* Selected Topics in Quantum Electronics, IEEE

Journal of, 2004. **10**(4): p. 709-727.

81. Huapu, P., et al. *The influence of nonlinear capacitance and responsivity on the linearity of a modified uni-traveling carrier photodiode*. in *Microwave photonics, 2008. jointly held with the 2008 asia-pacific microwave photonics conference. mwp/apmp 2008. international topical meeting on*. 2008.

82. Chtioui, M., et al., *High-Power High-Linearity Uni-Traveling-Carrier Photodiodes for Analog Photonic Links.* Photonics Technology Letters, IEEE, 2008. **20**(3): p. 202-204.

83. Sze, S.M. and K.K. NG, *Physics of Semiconductor Devices*. Third Edition ed. 2007, Hoboken, New Jersey: John Wiley & Sons, Inc.

84. Ambree, P., B. Gruska, and K. Wandel, *Dependence of the electron diffusion length in p-InGaAs layers on the acceptor diffusion process.* Semiconductor Science and Technology, 1992. **7**(6): p. 858.

85. Shimizu, N., et al. *Bandwidth characteristics of InP/InGaAs uni-traveling-carrier photodiodes*. in *Microwave Photonics, 1998. MWP '98. International Topical Meeting on*. 1998.

86. Kurishima, K., et al., *Fabrication and characterization of high-performance InP/InGaAs double-heterojunction bipolar transistors.* Electron Devices, IEEE Transactions on, 1994. **41**(8): p. 1319-1326.

87. Windhorn, T.H., et al., *Electron transport in InP at high electric fields.*

Applied Physics Letters, 1983. **42**(8): p. 725-727.

88. Sanchez, T.G., et al., *Electron transport in InP under high electric field conditions.* Semiconductor Science and Technology, 1992. **7**(1): p. 31.

89. Ishibashi, T., et al., *High-Speed Response of Uni-Traveling-Carrier Photodiodes.* Japanese Journal of Applied Physics, 1997. **36**(Copyright (C) 1997 Publication Board, Japanese Journal of Applied Physics): p. 6263.

90. Rohner, M., B. Willen, and H. Jackel, *Sub-ft gain resonance of InP/InGaAs-HBTs.* Electron Devices, IEEE Transactions on, 2002. **49**(2): p. 213-220.

91. Dagli, N., *Physical origin of the negative output resistance of heterojunction bipolar transistors.* Electron Device Letters, IEEE, 1988. **9**(3): p. 113-115.

92. Lampert, M.A., *Double Injection in Insulators.* Physical Review, 1962. **125**(1): p. 126-141.

93. Shockley, W., *Negative Resistance Arising from Transit Time in Semiconductor Diodes.* The Bell System Technical Journal, 1954. **XXXIII**(4): p. 799-826.

94. Zohta, Y., *Negative resistance of semiconductor heterojunction diodes owing to transmission resonance.* Journal of Applied Physics, 1985. **57**(6): p. 2334-2336.

95. Gribnikov, Z.S., K. Hess, and G.A. Kosinovsky, *Nonlocal and nonlinear transport in semiconductors: Real-space transfer effects.* Journal of Applied Physics, 1995. **77**(4): p. 1337-1373.

96. Eisele, H. and R. Kamoua, *Submillimeter-wave InP Gunn devices.* Microwave Theory and Techniques, IEEE Transactions on, 2004. **52**(10): p. 2371-2378.

97. Urick, V.J., et al. *Photodiode linearity requirements for radio-frequency photonics and demonstration of increased performance using photodiode arrays*. in *Microwave photonics, 2008. jointly held with the 2008 asia-pacific microwave photonics conference. mwp/apmp 2008. international topical meeting on*. 2008.

98. Itakura, S., et al., *High-Current Backside-Illuminated Photodiode Array Module for Optical Analog Links.* Lightwave Technology, Journal of, 2010. **28**(6): p. 965-971.

99. Shimizu, N. and T. Nagatsuma, *Photodiode-integrated microstrip antenna array for subterahertz radiation.* Photonics Technology Letters, IEEE, 2006. **18**(6): p. 743-745.

100. Wilkinson, E.J., *An N-Way Hybrid Power Divider.* Microwave Theory and Techniques, IRE Transactions on, 1960. **8**(1): p. 116-118.

101. Beling, A., et al., *Measurement and modelling of high-linearity partially depleted absorber photodiode.* Electronics Letters, 2008. **44**(24): p. 1419-

1420.

102. Draa, M.N., et al. *Voltage-dependent nonlinearities in uni-traveling carrier directional coupled photodiodes*. in *Microwave Photonics (MWP), 2010 IEEE Topical Meeting on*. 2010.

103. Hastings, A.S., D.A. Tulchinsky, and K.J. Williams, *Photodetector Nonlinearities Due to Voltage-Dependent Responsivity.* Photonics Technology Letters, IEEE, 2009. **21**(21): p. 1642-1644.

104. Hastings, A.S., et al., *Minimizing Photodiode Nonlinearities by Compensating Voltage-Dependent Responsivity Effects.* Lightwave Technology, Journal of, 2010. **28**(22): p. 3329-3333.

105. De Carvalho, N.B. and J.C. Pedro, *Large- and small-signal IMD behavior of microwave power amplifiers.* Microwave Theory and Techniques, IEEE Transactions on, 1999. **47**(12): p. 2364-2374.

106. Suzuki, N. and K. Tada, *Electrooptic properties and Raman scattering in InP.* JAP. J. APPL. PHYS., 1984. **23**(3): p. 291-295.

107. Callaway, J., *Optical Absorption in an Electric Field.* Physical Review, 1964. **134**(4A): p. A998-A1000.

108. Lambert, L.M., *Optical absorption in an electric field in semi-insulating gallium arsenide.* Journal of Physics and Chemistry of Solids, 1965. **26**(9): p. 1409-1418.

109. Zielinski, E., et al., *Excitonic transitions and exciton damping processes in*

InGaAs/InP. Journal of Applied Physics, 1986. **59**(6): p. 2196-2204.

110. Bhattacharya, P., *Properties of lattice-matched and strained Indium Gallium Arsenide*. 1993: Inspec/Iee.

111. Pires, M.P., T. Chang, and N. Sauer, *Measurement of Heavy and Light Hole Masses in InGaAs/InAlAs Quantum Wells.* Brazil. J. Phys, 1997. **27**(4): p. 223-226.

112. Ng, J., et al., *Field dependence of impact ionization coefficients in In< sub> 0.53</sub> Ga< sub> 0.47</sub> As.* Electron Devices, IEEE Transactions on, 2003. **50**(4): p. 901-905.

113. Williams, K.J. and D.A. Tulchinsky. *Impact of photodiode nonlinearities on optical to microwave frequency conversion*. in *Holey Fibers and Photonic Crystals/Polarization Mode Dispersion/Photonics Time/Frequency Measurement and Control, 2003 Digest of the LEOS Summer Topical Meetings*. 2003.

114. Lee, C.P., W. Ma, and N.L. Wang, *Averaging and cancellation effect of high-order nonlinearity of a power amplifier.* Circuits and Systems I: Regular Papers, IEEE Transactions on, 2007. **54**(12): p. 2733-2740.

115. McKinney, J., K. Colladay, and K.J. Williams, *Linearization of Phase-Modulated Analog Optical Links Employing Interferometric Demodulation.* J. Lightwave Technol., 2009. **27**(9): p. 1212-1220.

116. Walker, A., M. Steer, and K. Gard, *Simple, Broadband Relative Phase*

Measurement of Intermodulation Products, in *ARFTG Conference, 65th*. 2005: Long Beach, California.

117. Remley, K.A., et al., *Simplifying and interpreting two-tone measurements.* Microwave Theory and Techniques, IEEE Transactions on, 2004. **52**(11): p. 2576-2584.

118. Haifeng, J., et al., *Noise Floor Reduction of an Er:Fiber Laser-Based Photonic Microwave Generator.* Photonics Journal, IEEE, 2011. **3**(6): p. 1004-1012.

119. Ivanov, E.N., S.A. Diddams, and L. Hollberg, *Study of the excess noise associated with demodulation of ultra-short infrared pulses.* Ultrasonics, Ferroelectrics and Frequency Control, IEEE Transactions on, 2005. **52**(7): p. 1068-1074.

120. Kan, W., et al., *Characterization of the Excess Noise Conversion From Optical Relative Intensity Noise in the Photodetection of Mode-Locked Lasers for Microwave Signal Synthesis.* Lightwave Technology, Journal of, 2011. **29**(24): p. 3622-3631.

121. Taylor, J., et al., *Characterization of Power-to-Phase Conversion in High-Speed P-I-N Photodiodes.* Photonics Journal, IEEE, 2011. **3**(1): p. 140-151.

122. Zhang, W., et al., *Amplitude to phase conversion of InGaAs pin photo-diodes for femtosecond lasers microwave signal generation.* Applied

Physics B: Lasers and Optics, 2012. **106**(2): p. 301-308.

123. Joshi, A. and S. Datta, *Dual InGaAs Photodiodes Having High Phase Linearity for Precise Timing Applications.* Photonics Technology Letters, IEEE, 2009. **21**(19): p. 1360-1362.